Band Engineering of Graphene using Metal Mediated Oxidation

A Thesis Submitted to the College of

Graduate Studies and Research

In Partial Fulfillment of the Requirements

For the Degree of Doctor of Philosophy

In Physics and Engineering Physics

University of Saskatchewan

Saskatoon

By

Paul Bazylewski

PERMISSION TO USE

In presenting this thesis in partial fulfilment of the requirements for a Postgraduate degree from the University of Saskatchewan, I agree that the Libraries of this University may make it freely available for inspection. I further agree that permission for copying of this thesis in any manner, in whole or in part, for scholarly purposes may be granted by the professor or professors who supervised my thesis work or, in their absence, by the Head of the Department or the Dean of the College in which my thesis work was done. It is understood that any copying or publication or use of this thesis or parts thereof for financial gain shall not be allowed without my written permission. It is also understood that due recognition shall be given to me and to the University of Saskatchewan in any scholarly use which may be made of any material in my thesis.

Requests for permission to copy or to make other use of material in this thesis in whole or part should be addressed to:

Head of the Department of Physics and Engineering Physics

University of Saskatchewan

Saskatoon, Saskatchewan S7N 5E2

ABSTRACT

In the study of materials for electronic devices, there is a continuous search for new materials with useful properties. In the early 2000's, the 2D semi-metal carbon material graphene was isolated and characterized experimentally, and found to have a variety of desirable electronic properties. Since that time research on graphene and graphene related materials has progressed at an ever growing rate as researchers seek to understand, manipulate, and enhance graphene for use in electronic devices. One arm of this research seeks to manipulate the band structure of graphene such that it behaves like a semiconductor in devices. This thesis reports a study of four graphene systems investigated to attempt to manipulate the electronic structure in graphene; Graphene/Cu, Co/Graphene/Cu, Graphene/Co/SiO_2, Co/Graphene/SiO_2. The properties of these systems were investigated using various X-ray spectroscopy and surface science techniques. The analysis showed that the band structure of Graphene/SiO_2 may be manipulated by depositing cobalt on the graphene surface. At a low concentration, the cobalt is completely oxidized into primarily CoO, and the graphene is not heavily damaged. Oxide groups form on the graphene surface but are found to be proportional to the cobalt thickness below 1 nm. Using X-ray spectroscopy a band gap of up to 0.30 ± 0.10 eV is observed in graphene 2*p* states when a low concentration of cobalt forms islands on the graphene surface. The mechanism of band gap opening was interpreted using electronic structure calculations to have a contribution from both graphene oxide formation as well as the presence of CoO. These results have implications for graphene electronics and spintronics where magnetic metals can be used to induce a band gap in graphene that is stable at room temperature and under atmospheric exposure.

ACKNOWLEDGEMENTS

This thesis was the culmination of a lot of work that is not presented in it. In the interest of presenting something coherent no mention is made of many people who I worked with over the years on various side projects not directly related to my thesis work. In no particular order I wish to acknowledge Robert Bauer, Sarah Purdy, David Muir, John McLeod, Adrian Hunt, Eamon McDermott, Neil Johnson, Jay Forrest, Luan Van Nguyen, Teak Boyko, Tom Regier, Jason Maley, Alex Moewes, Muhammad Husain, Matteo Balestrieri, Brett Leedahl and Robert Green. All of these people at one time or another taught me something important about physics or science or life through personal conversations, and I would not be the same person today without knowing and working with each of these people. In many ways I feel that I have learned more from simple discussions with free flowing ideas than I ever have or ever will from individual study. Research should be a collaboration.

Special acknowledgement is also be given to the researchers that contributed electronic structure calculations and experimental measurements to this study. X-ray photoelectron spectroscopy measurements were contributed by Dr. Andery I. Kukharenko, Dr. Seif O. Cholakh, and Dr. Ernst Z. Kurmaev working at the Ural Federal University, Yekaterinburg, Russia. Multi-ligand Field Theory calculations were performed by Brett Leedahl during his graduate studies at the University of Saskatchewan as part of the Beam Team research group. DFT calculations using WIEN2K were performed by Eamon McDermott and Adrian Hunt during their graduate studies at the University of Saskatchewan, also as part of the Beam Team research group. DFT calculations using SIESTA were contributed by Dr. Danil W. Boukhvalov working at the Korean Institute for Advanced Study (KIAS) in the School of Computational Sciences, Korea. All of these researchers

contributed greatly to this work with their own time, effort, and expertise, and this project would not have been successful without their insightful input.

Last I will give acknowledgement to Gap Soo Chang, my graduate level supervisor. Throughout the years he has always given me measured and reasonable advice in all things ranging from materials science research to having children. In his group there was never any shortage of research opportunities and I was always free to speak my mind and pursue my research as I saw fit without micromanaging. I now believe that one of the most important factors in becoming a successful researcher is time management, so I thank Gap Soo for creating an environment where my success or failure was always in my own hands.

TABLE OF CONTENTS

LIST OF TABLES

LIST OF FIGURES

LIST OF ABBREVIATIONS

Abbreviation	Long Name
VB	Valence band
F_4TCNQ	2,3,5,6-Tetrafluoro-7,7,8,8-tetracyanoquinodimethane
F2-HCNQ	3,6-difluoro-2,5,7,7,8,8-hexacyano-quinodimethane
DMC	dimethyl carbonate
HOPG	highly ordered pyrolytic graphite
GO	Graphene Oxide
GNR	Graphene Nano Ribbon
CNT	Carbon Nano Tube
DOS	Density of States
RKKY	Ruderman-Kittel-Kasuya-Yosida (Exchange Coupling)
STM	Scanning Tunneling Microscopy
EXAFS	Extended X-ray absorption fine structure
CLS	Canadian Light Source
ALS	Advanced Light Source
BL8	Beamline 8.0.1
REIXS	Resonant Elastic-Inelastic X-ray Scattering
XAS	X-ray Absorption
XES	X-ray Emission
TFY	Total Fluorescence Yield
TEY	Total Electron Yield
HXMA	Hard X-ray Microanalysis (beamline)
NEXAFS	Near edge X-ray absorption fine structure
XANES	X-ray absorption near edge structure
XPS	X-ray Photoelectron Spectroscopy
MLFT	Multi-Ligand Field Theory
DFT	Density Functional Theory
AFM	Atomic Force Microscopy
TEM	Transmission Electron Microscopy
HAADF	High-Angle Annular Dark Field (imaging)
SSSC	Saskatchewan Structural Sciences Center
PVD	Physical Vapor Deposition
PID	Proportional-Integral-Derivative (controller)
CVD	Chemical Vapor Deposition
PMMA	Polymethylmethacrylate
CBM	Conduction Band Minimum
VBM	Valence Band Minimum
S-SWNT	Semiconducting Single Walled Nanotubes
HR-TEM	High Resolution Transmission Electron Microscope
RMSR	Root Mean Square Roughness
LDA	Local Density Approximation

LAPW	Linear Augmented Plane Wave (basis set)
APW+lo	Augmented Plane Wave plus local orbital (basis set)
PBE	Perdew–Burke–Ernzerhof (functional)
mBJ	Tran-Blaha modified Becke-Johnson (potential)
XMCD	X-ray Magnetic Circular Dichroism
XMLD	X-ray linear magnetic dichroism
h-BN	Hexagonal boron nitride

CHAPTER 1

INTRODUCTION

In the past decade since its isolation, graphene has become one of the most popular topics in electronic materials and device research. Although not officially isolated until 2004 by Novoselov and Geim [1], the properties of graphitic materials have been analyzed and studied since the early 1900's. In 1962, the name 'graphene' was first coined by H. P. Boehm [2], but the result did not garnish much attention at the time. This was partially due to the experimental difficulties of isolating a pristine sample of graphene. Without such a sample, graphene's properties were not easily quantifiable, and for more than four decades its unique characteristics remained largely unknown. Prior to 2004, several reports can be found detailing the synthesis of graphene-like materials and even monolayer graphene [3,4]. Graphite oxide was independently synthesized in 1959 [5], and monolayer graphene was reported to be found on the surface of silicon carbide after annealing at high temperature in 1975 [6].

However, none of those studies reported discovery of graphene's unique electronic properties until 2004. Since that time, graphene has become heavily studied and attracted the attention of much of the scientific community in fields ranging from materials science to medicine. In the decade it has been under study since its isolation, graphene has found applications in transistors [7,8], photovoltaics cells [9,10], sensors [11], as a corrosion barrier [12], and in spintronics devices [13]. The rate of research and filing of new patents related to graphene has exploded over the past decade, as reported by Thomson Reuters (Figure 1.1), with just 33 inventions in 2004 increasing to 5,000 in 2013 [14]. With many of these patents published by electronics companies, it has been

predicted that graphene will make its way into next generation devices over the next 2 decades [15] (Figure 1.2).

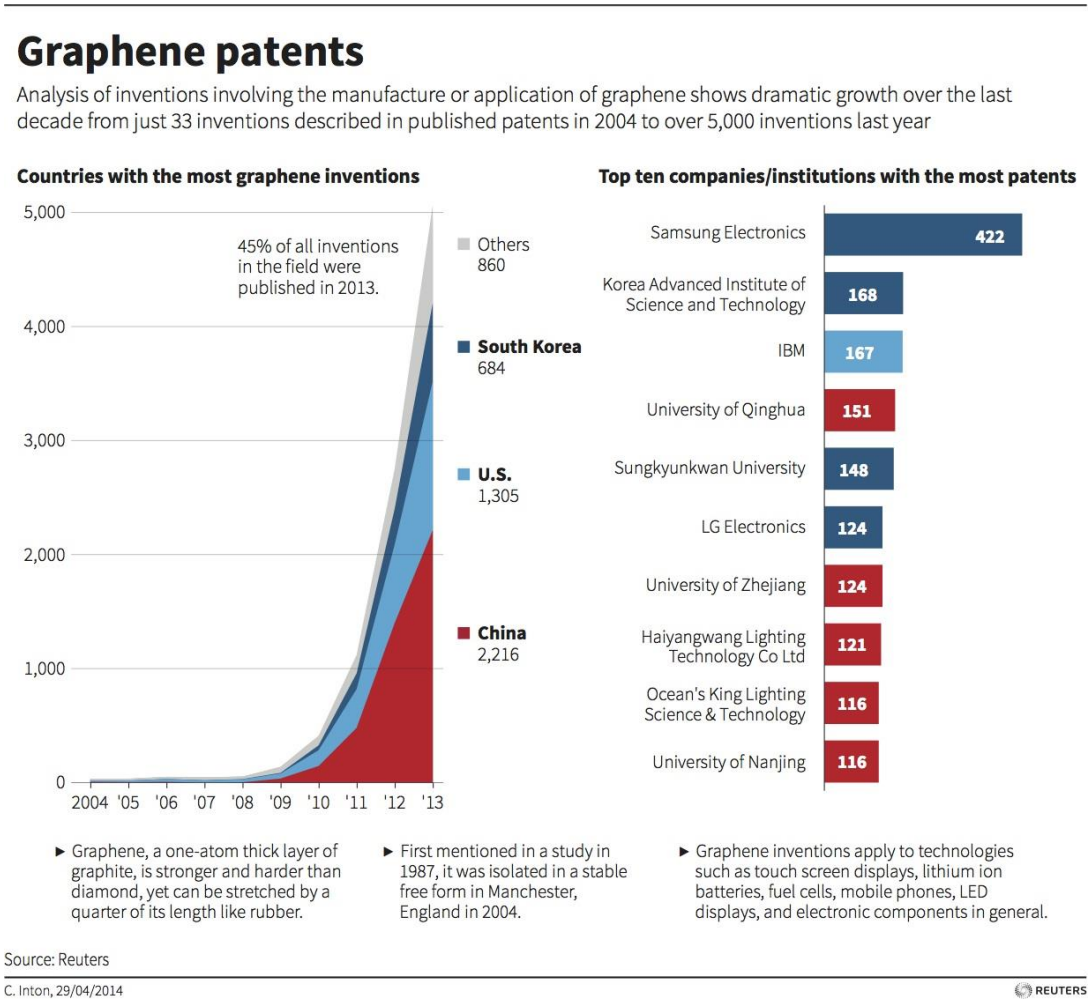

Figure 1.1. Published patents involving the manufacture or application of graphene from 2004-2013.

Fabrication of devices using graphene still poses many difficulties, often resulting in complex and costly fabrication procedures. One consideration is a difficulty in electrically contacting the graphene. The unique structure that gives rise to so many interesting properties is a double-edged sword in that its low kinetic reactivity makes the pristine graphene surface resistant to covalent

bonding. This results in often poor interfaces between graphene and metallic contacts, making it difficult to incorporate without more complex fabrication methods.

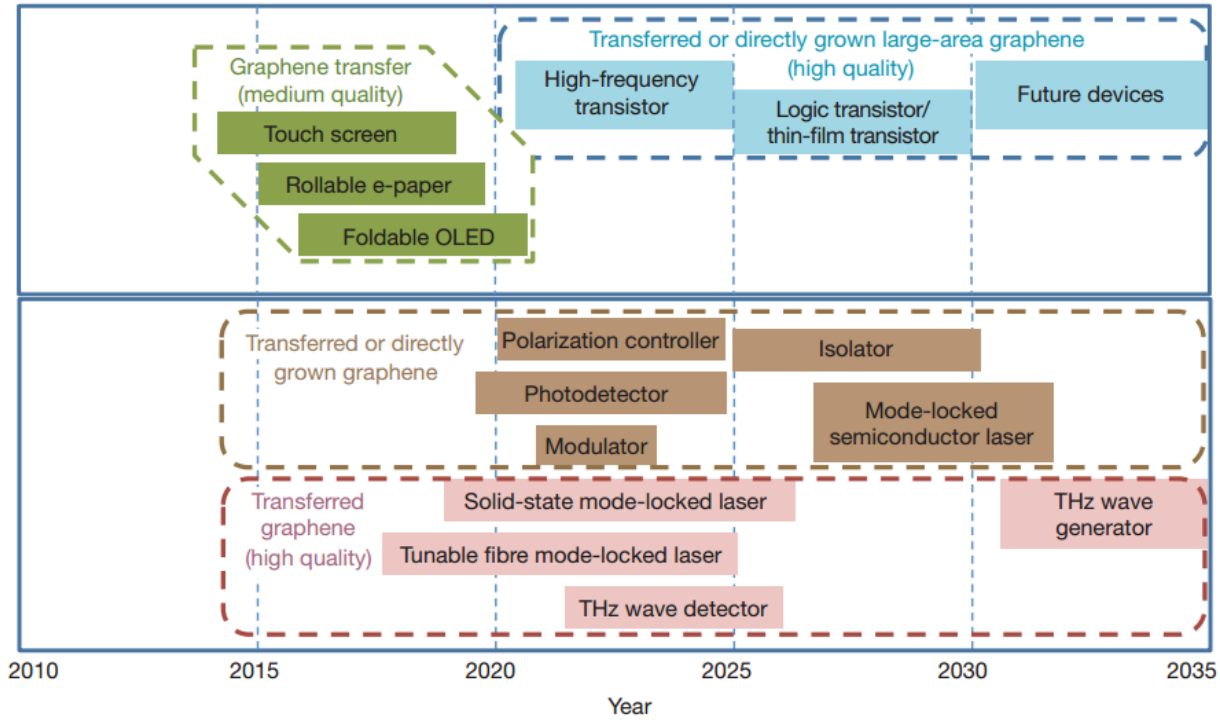

Figure 1.2. Applications of graphene in electronics. Display applications are shown in green; electronic applications are shown in blue. Optical applications are shown in pink; optical interconnect applications are shown in brown. The figure gives an indication of when a functional device prototype could be expected based on device roadmaps and the development schedules of industry leaders. Adapted from Ref. 12.

For some applications, the use of graphene is also limited by a lack of intrinsic band gap. Pristine graphene without defects does not possess an electronic band gap, and introducing one that is tunable and reproducible is difficult to achieve. This thesis presents a study on a method to open an electronic band gap in graphene, termed cobalt-mediated oxidation. This metal-mediated oxidation has both advantages and disadvantages compared to other methods, and may have use

in graphene based devices. The following chapters will cover the details of this study beginning with the basic properties of graphene and its history in electronic devices, followed by literature examples of graphene research for device applications. Next is details of the experimental and theoretical tools used including X-ray spectroscopy, Raman spectroscopy, atomic force microscopy, and density functional theory simulations. The final chapters report the analysis and discussion of the results, including conclusions and ongoing future work.

1.1 Graphene: Physical properties and Band Structure

The name graphene refers a single layer of graphite that has been isolated or grown in isolation. Structurally graphene consists of a hexagonal pattern of sp^2 bonded carbon atoms in a single layer [Figure 1.3(a)]. The atoms are spaced 1.42 Å apart with a bonding angle of 120° to form a honeycomb-like structure consisting of a single layer of atoms. This structural arrangement gives graphene high mechanical strength as well as interesting thermal, optical, and electrical properties. Researchers were quick to quantify the properties of single and multi-layer graphene using modern measurement techniques, revealing excellent thermal conductivity (3000 W/m·K), mechanical stiffness (1060 GPa), optical transparency (>90%), and charge carrier mobility (2000-20,000 cm^2/Vs) [16-20]. These properties make graphene very mechanically robust and desirable for electronic applications requiring transparent or very thin materials. As a short note on naming, multi-layer graphene up to several layers is often referred to generally as "graphene". For the rest of this document, "graphene" refers to only a single layer unless otherwise stated.

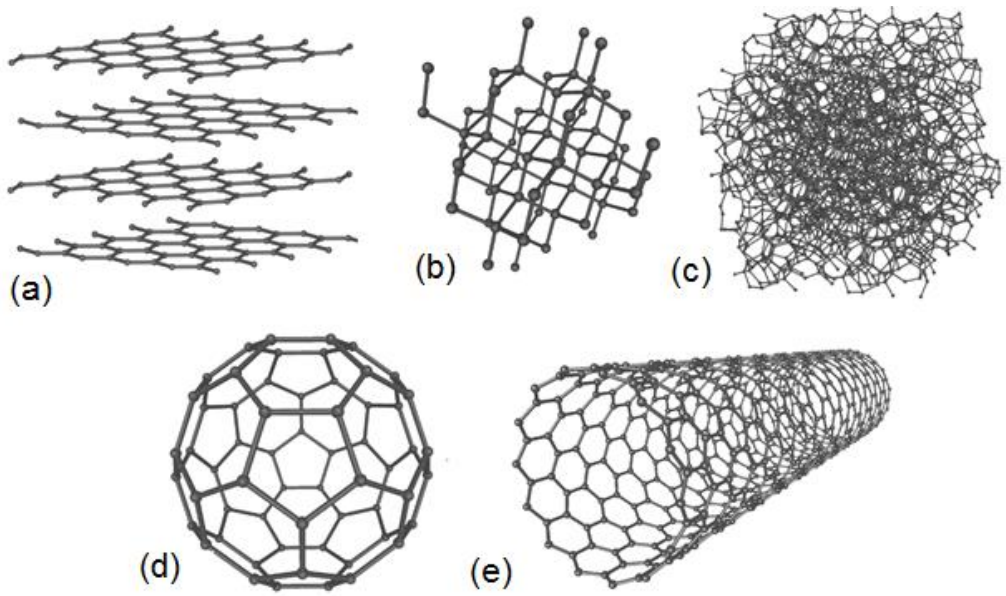

Figure 1.3. Common carbon allotropes used in electronic devices. (a) graphite, (b) diamond, (c) amorphous carbon, (d) C_{60} fullerene, (e) carbon nanotube (single wall).

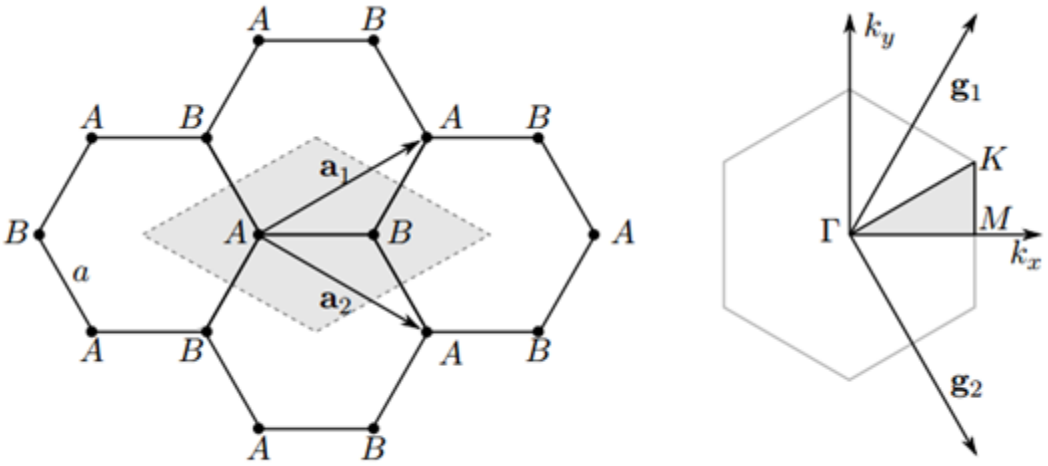

Figure 1.4. Graphene unit cell. On the left is the graphene lattice and unit cell (gray) with *A* and *B* lattices and primitive vectors marked. On the right is the Brillouin Zone with *k*-points, reciprocal lattice vectors, and high symmetry points marked. This figure was adapted from Ref. [21,22].

The 2D structure of graphene gives rise to a unique band structure that can be derived theoretically. To begin with the derivation of the reciprocal lattice, graphene is broken into two sub-lattices *A* and *B* (Figure 1.4). The following derivation has been adapted from references [21] and [22]. The structure has a unit cell containing only 2 atoms, allowing the primitive lattice vectors to be defined as below where $\boldsymbol{a} \approx 1.42$ Å, yielding a graphene lattice constant of $|a_1| = |a_2| = 2.46$ Å.

$$\boldsymbol{a_1} = \frac{a}{2}\left(3, \sqrt{3}\right) \quad , \quad \boldsymbol{a_2} = \frac{a}{2}\left(3, -\sqrt{3}\right) \tag{1}$$

The reciprocal lattice vectors can then be computed as:

$$\boldsymbol{g_1} = \frac{2\pi}{3a_o}\left(1, \sqrt{3}\right) \quad , \quad \boldsymbol{g_2} = \frac{2\pi}{3a_o}\left(1, -\sqrt{3}\right) \tag{2}$$

To calculate the band structure in graphene *p*-states, the tight binding model is typically used where only nearest neighbor contributions are considered. By constructing the Hamiltonian in the tight binding approximation, an energy dispersion relation can be derived, which was first derived by Wallace in 1947 [22].

$$E_D(\boldsymbol{k}) = E_F \pm t\left[1 + 4cos\left(\frac{3k_x a}{2}\right)cos\left(\frac{k_y a}{2}\right) + 4cos^2\left(\frac{k_y a}{2}\right)\right]^{1/2} \tag{3}$$

The value *t* refers to the nearest neighbor hopping energy and is $t \approx 2.8$ eV in graphene, with positive and negative values used to represent the bonding and antibonding π-bands. Equation (3) can be plotted to visually represent the band structure, showing that the π and π* bands touch at the *K* symmetry point (Figure 1.5), and that the band shape appears linear near the *K*-point or Dirac point.

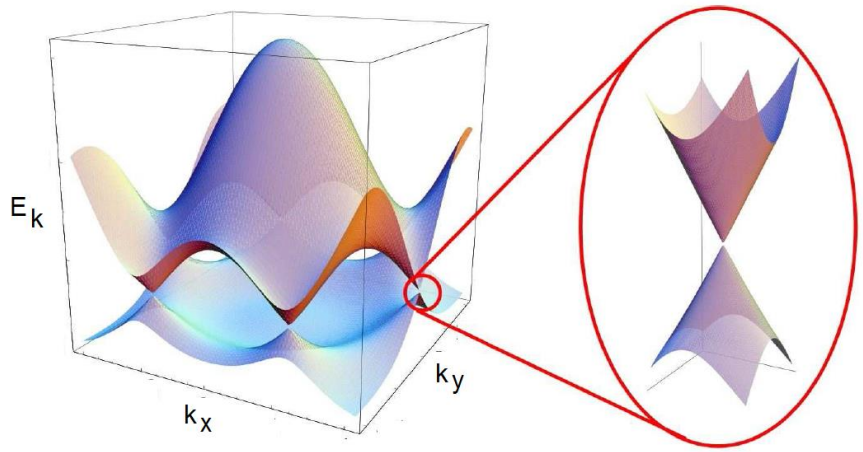

Figure 1.5. Energy spectrum of graphene and around the Dirac point. On the left the energy spectrum of graphene plotted in 2 dimensions. On the right is a close view around a Dirac point showing the conical shape. This figure was adapted from Ref. 21.

This linear shape of the dispersion curve near the Dirac point is fundamentally different than that observed for typical semiconductors with a parabolic band shape, and is the origin of many of the electronic properties of graphene. As shown in Figure 1.6 (left) the dispersion relation for a typical semiconductor is curved near the *K*-point and can be described by the equation for a parabolic band (Equation 4), where m^* is charge carrier effective mass).

$$E = \frac{\hbar^2 k^2}{2m^*} \tag{4}$$

The charge carrier effective mass in this case can be determined by deriving the 2nd derivative with respect to energy to yield an equation for effective mass of (low energy) electrons in semiconductors with a parabolic band (Equation 5).

$$\frac{1}{m^*} = \frac{1}{\hbar^2}\frac{d^2E}{dk^2} \tag{5}$$

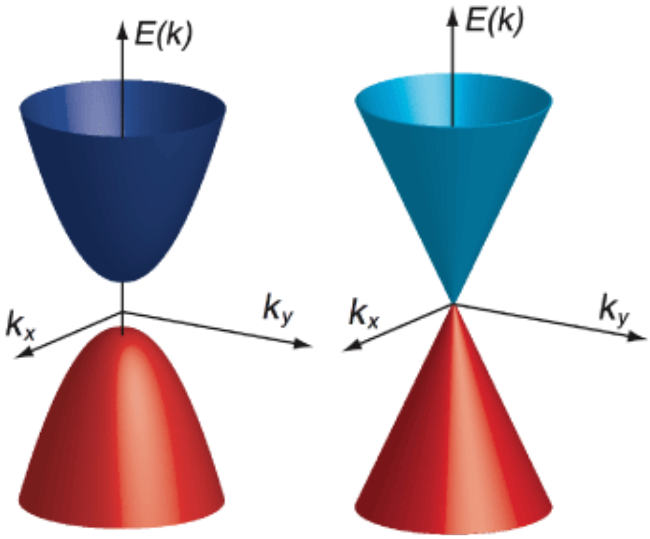

Figure 1.6. Dispersion curves for (left) a typical semiconductor, and (right) in graphene. This figure was adapted from Ref. 21.

By contrast to a typical semiconductor, the band structure in pristine graphene presents a linear dispersion near the Dirac point (Figure 1.6, right). An equation describing the linear shape can be derived by expanding equation (3), and is given by equation (6) where v_F is the Fermi velocity.

$$E = \pm \hbar v_F |k| \tag{6}$$

In the case of a non-parabolic band, the definition of effective mass in equation (5) no longer applies. A more general relationship between total particle energy, *E*, and charge carrier or particle effective mass can be derived by considering wave-particle duality with an associated group ($v_g \simeq \hbar^{-1}(\partial E/\partial k)$) and phase velocity ($v_p \simeq E/\hbar k$) given by equation (7) [23].

$$E \simeq m^* v_g v_p \tag{7}$$

Using the linear dispersion relation in graphene (equation 6) with the definitions of group and phase velocity, it can be shown that $v_g = v_p = v_f$ in graphene [23]. Therefore the effective mass of charge carriers in graphene from equation (7) depends on the momentum ($\hbar k$) of the particle as given by equation (8).

$$m^* \simeq \frac{E}{v_g v_p} \simeq \frac{\hbar k}{v_F} \tag{8}$$

From the linear band dispersion, the Fermi velocity can be computed to be the same order of magnitude as the speed of light in graphene ($v_F \approx 1 \times 10^6$ m/s) [22]. Inserting this value into equation (8) shows that charge carriers in graphene have very low effective mass and behave as nearly massless particles near the Dirac point. This linear band shape near the Dirac point means that when $E_{Fermi} = 0$, the graphene valence band (VB) is exactly filled and the conduction band is empty, with the two bands meeting at the Dirac points. Therefore graphene is termed a semi metal or gapless semiconductor with charge carriers that behave like massless Dirac fermions. For a prefect graphene sheet free from impurities and disorder, the Fermi energy lies at the Dirac point.

The electronic properties of pristine graphene arise from the behavior of charge carriers around the Dirac points, but the subject of this thesis is the modification of the graphene band structure to form a band gap. The goal of this research is to induce a semiconducting band gap in graphene while preserving as much as possible its electrical and mechanical properties. Several methods have been derived to induce a semiconducting gap in graphene, which are discussed in the following sections.

1.2 Engineering a Band Gap in Graphene

The following section outlines some methods that can be found in the literature that have successfully opened a band gap in graphene. Methods not discussed that may of interest to the reader concern band gap opening in multilayer graphene using electric or magnetic fields or asymmetrical layer stacking [24,25]. In this study, it was assumed that the graphene obtained initially is single layer without significant wrinkling or areas of multilayer graphene, and no electric or magnetic fields were applied during measurements. Therefore band gap opening effects in multi-layer graphene due to electrical or magnetic fields are not considered to contribute.

1.2.1 Chemical Functionalization

The most straight forward approach to changing the physical properties of any material is to introduce other materials to produce a new (better) composite material. Many attempts have been made in the literature to functionalize single and multilayer graphene using single atoms or molecules deposited on the surface or by substitution. Using multilayer graphene, the top layer of bi- or tri-layer graphene may be functionalized with organic molecules in order to break the layer symmetry by charge transfer, yielding a typical semiconducting gap of 100-200 meV [26]. A wide variety of band gap energies can be obtained depending on the type of organic molecule adsorbed and its location on the graphene surface (Figure 1.7). Organic materials can become tightly bound to the graphene surface through π-π interaction, in some cases making the band gap permanent and insensitive to temperature or charge carrier concentration. Bilayer graphene modified with organic 2,3,5,6-Tetrafluoro-7,7,8,8-tetracyanoquinodimethane (F_4TCNQ) molecules has been used in field effect transistors to achieve a mobility up to 1600 cm^2/Vs and a tunable band gap from 0 – 300

meV [27]. Using organic materials to modify graphene is advantageous in that it is scalable to large quantities with a tunable band gap provided a homogenous distribution of molecules can be obtained. The main disadvantages with this method are the small range of accessible band gap energies, control of the carrier type, and the requirement for a variety of different molecules needed to tune the band gap to a desired energy [26].

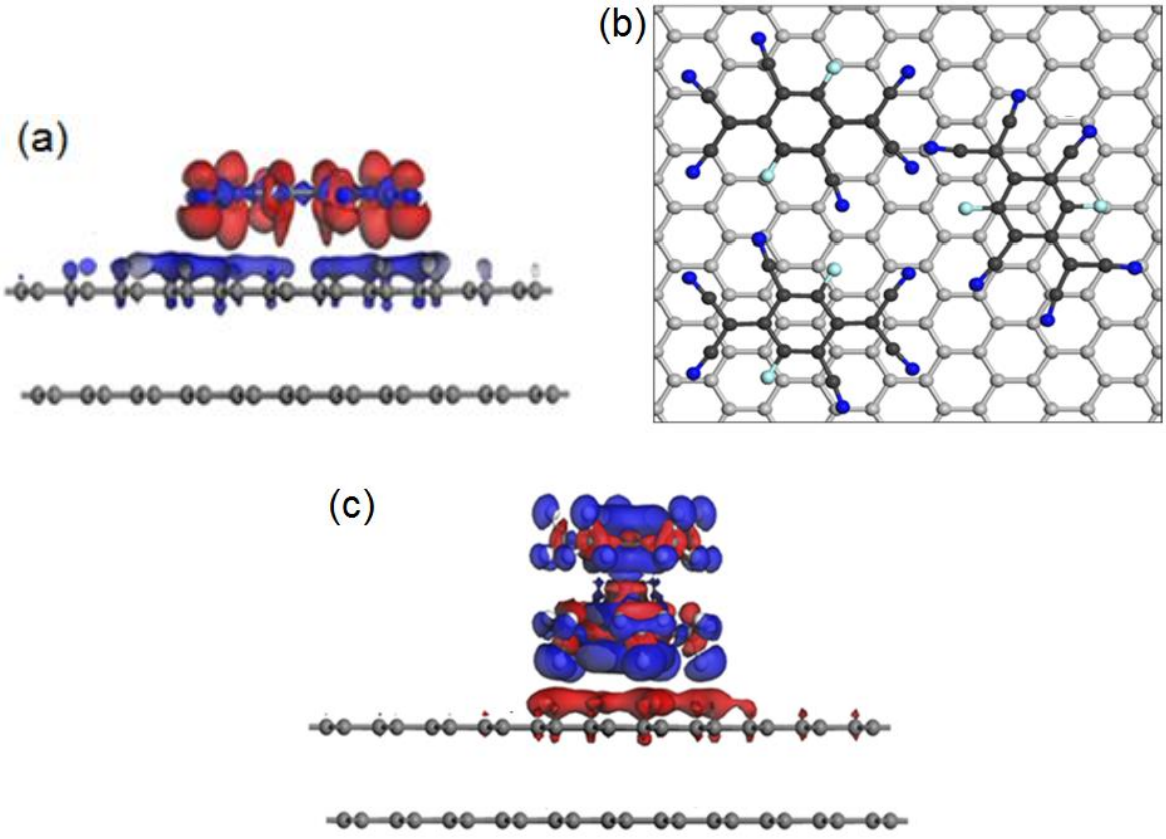

Figure 1.7. Examples of molecular functionalization. (a) Bilayer graphene modified with adsorbed 3,6-difluoro-2,5,7,7,8,8-hexacyano-quinodimethane (F2-HCNQ) molecule. Red and blue regions show areas of increasing and decreasing electron density, respectively. (b) High symmetry adsorption geometries for the F2-HCNQ molecule yielding a band gap. (c) Bilayer graphene modified with adsorbed dimethyl carbonate (DMC) molecule. This figure was adapted from images in Ref [25].

One of the more successful examples using single layer graphene is fluorinated graphene or fluoro-graphene [28,29]. This is achieved by the addition of fluorine atoms across the carbon-carbon double bond, typically starting with highly ordered pyrolytic graphite (HOPG) and reacting it with fluorine gas at high temperature, followed by isolation using exfoliation. Fluoro-graphene is mechanically stable with a band gap up to 3 eV depending on the degree of fluorination, and can be a high quality insulator with resistivity in excess of 10 GΩ at room temperature. Fluoro-graphene has been used in devices as an interface modification layer, an insulator, as well as a semiconductor in transistor devices [29,30]. Through the clever use of buffer layers, a single sheet of graphene can become a transistor through selective fluorination to produce adjacent insulating and semiconducting areas.

The most prolific example of the chemical functionalization approach is graphene oxide (GO). GO can be fabricated by exfoliation of graphite in oxidizing solvents, where covalent bonding with oxygen forms sp^3 and sp^2 hybridizations that can open a band gap of 0.02 to 3.5 eV, depending on the reduction level and number of graphene layers (Figure 1.8) [32]. GO has been implemented successfully in sensors [11,33], transistors [7], and solar cells [9,10]. Typically GO is used as a single layer in devices, but there are monolithic examples of all graphene/graphene oxide devices [8].

With implementation of GO (and other graphene derivatives) into devices, the concerns become reliable fabrication with reproducible properties in a scalable manner. The use of GO is advantageous because it is scalable to large quantities and the band gap is tunable over a wide range. The fabrication procedure also can be done without significant high vacuum systems or otherwise complicated equipment. However, there are disadvantages concerning the reproducibility and yield of GO with the desired properties from a given fabrication run. Impurity

sites and defects in the precursor graphite can contribute to non-homogeneous distribution of oxygen functional groups, making it more difficult to produce large quantities of GO with consistent, reproducible properties. Additionally, to tune the band gap energy thermal annealing is required, which can introduce defects and fragment the GO. But in spite of these difficulties, GO production has become scalable to large quantities with many high quality products available commercially and used regularly in research. Similar issues are present such as difficulties of homogeneous distribution of additive materials for other functionalized forms of graphene.

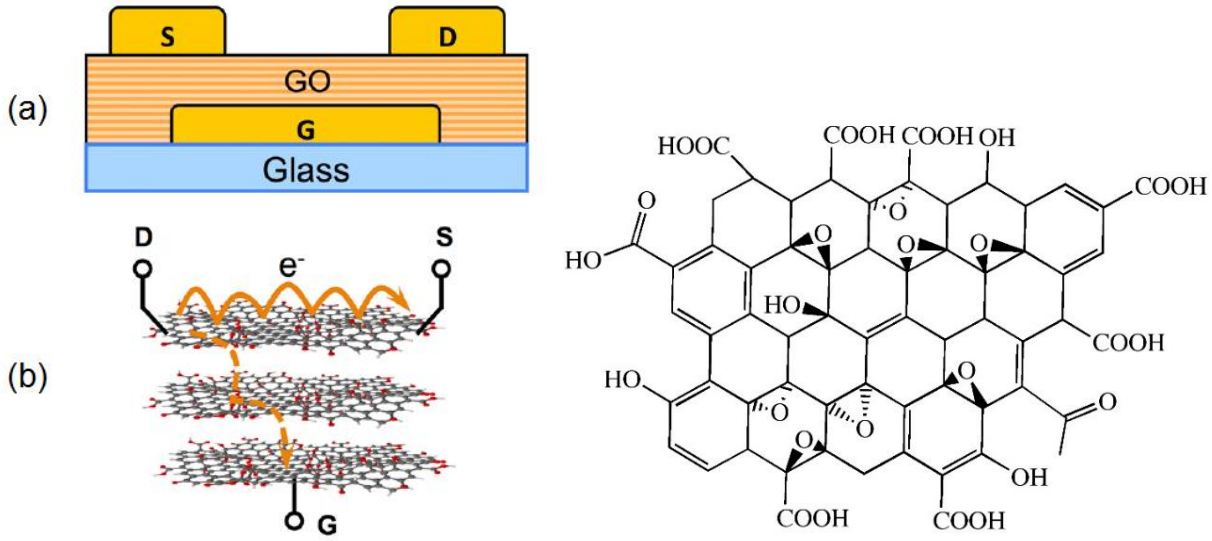

Figure 1.8. GO transistor and schematic. (a) An example of a GO transistor employing an insulating/semiconducting heterostructure. (b) Conduction pathways through the GO layers in this device. On the right the GO structure resulting from exfoliation. sp^3 and sp^2 functional groups including carboxyl (COOH), hydroxyl (C-OH), carbonyl (C=O), and epoxide (C-O-C) form non-homogeneously. This figure adapted from Ref. [8].

1.2.2 Quantum Confinement and Edge Effects

Another method to modify the band gap energy of graphene is to limit the size of a bulk sample to a graphene nanoribbon (GNR) or nanofragment. Ribbons or fragments possessing a width of ~10 nm can exhibit quantum confinement and edge effects, resulting in band structure that is very different from bulk graphene. Quantum confinement begins to take effect when the size of the nanoparticles approaches the exciton Bohr radius of the material. Therefore the onset of confinement depends on properties of the specific material including dielectric constant and charge carrier effective masses, which in turn determine the Bohr radius. Below this size threshold, charge carriers no longer exist in an effectively infinite lattice, but are confined in a potential well where the boundaries are simply the edge of the nanoparticle. The properties of a potential well are known and can be solved using the Schrodinger Equation to show that discrete energy levels exist with a discrete energy splitting depending on the size of the well (and charge carrier effective mass, m^*), given by equation (9). The energy splitting is seen to increase with decreasing size L, and therefore the band gap in nanomaterials can be dependent on their physical size.

$$E_n = \frac{n^2 h^2 \pi^2}{2m^* L^2} \tag{9}$$

This concept has been utilized to great effect through the development of semiconductor quantum dots for numerous applications including commercial applications such as solar cells and medical imaging. The quantum confinement effect can be observed in graphene when GNRs or fragments are used, which can be fabricated from graphite, carbon nanotubes (CNTs), or organic molecule precursors using chemical or lithography techniques. Studies using molecular precursors

have shown GNRs fabricated with a reproducible, controllable band gap of 1.4 or 2.5 eV [34]. However the usable yield from this procedure is low because the GNRs grow chaotically, and pristine samples must be located, isolated, and measured *in situ*. Exfoliation of graphite using etching solvents is a less complex method, but at a similar cost in low yields and poor reproducibility [35]. For device applications, GNRs have been integrated into devices using metal-nanowire-etching to fabricate a ribbon-based device *in situ*, with very good performance of the resulting device [36].

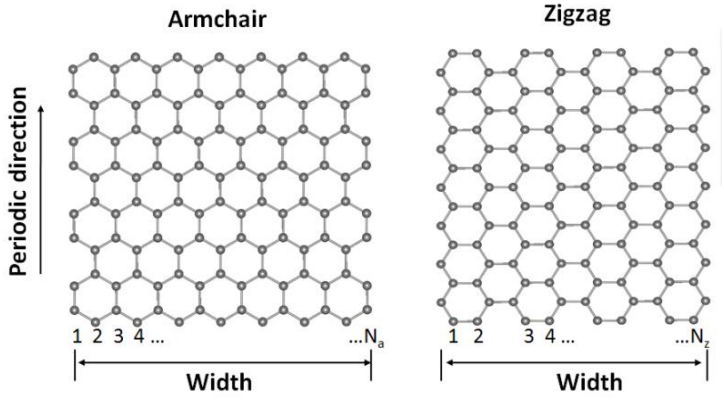

Figure 1.9. Example of armchair and zigzag graphene nanoribbons. Adapted from ref [37].

Aside from quantum confinement in graphene nanostructures, edge effects also play a role in modifying the graphene band structure. Due to the hexagonal pattern of graphene, two edge types are possible: armchair or zigzag (Figure 1.9). Both types of nanoribbon edges are subject to reactivity with other species such as hydrogen, where the zigzag edge possesses slightly higher reactivity due to an unpaired electron. [38]. The zigzag edge also therefore possesses localized edge states that contribute to the density of states (DOS) near the Fermi level. These localized

states can become spin polarized, leading to a magnetic moment in GNRs and other graphene based nanostructures. For the purposes of band gap engineering, the type of edge and the concentration of defects on the edge, as well as the overall size of GNRs, both play a large role in determining the band gap energy.

Using GNRs is advantageous for semiconducting applications because they can be fabricated very reproducibly with consistent characteristics. To obtain a desired band gap, one need only produce a GNR of the desired width. GNRs are also by definition on the nanoscale, making them ideal for thin, nanoscale devices. The disadvantages mainly stem from difficulties in scalability of the fabrication methods. Growth using molecular precursors generally does not produce a high yield of identical GNRs, but rather a range of sizes from a few units wide to larger sheets that do not exhibit quantum confinement. Fabrication by unzipping CNTs is by contrast very reproducible where the width of the GNR depends only on the diameter of the CNT precursor. The main limitation here is the requirement for well-defined CNTs as the starting material. Similar to the case of GO, any non-uniformity or defects in the precursor CNTs can result in GNRs with a range of sizes and electronic properties.

1.2.3 RKKY Magnetic Exchange Coupling

In addition to quantum confinement, magnetic exchange coupling has been identified as a method to open a band gap in graphene. Specifically, Ruderman-Kittel-Kasuya-Yosida (RKKY) exchange coupling; pure superexchange and double exchange are not considered in the graphene architecture under study here. RKKY exchange is fundamentally different from super and double exchange in that it does not involve actual transfer of electrons across an intermediary atom. Here

the exchange can be visualized by taking an isolated magnetic moment in a sea of conduction electrons such as in a metal. The electrons acquire a spin polarization due to a magnetic moment that oscillates in direction with distance from the origin (a magnetic impurity atom or cluster), and persists over relatively large distances (3-4 nm). Effectively the electrons are scattered by the impurity and such an oscillatory spin rearrangement is more energetically favorable. Two isolated magnetic impurities may be coupled through this electron oscillation, with a strength defined by a distance dependent exchange coupling constant *J(R)* where *R* is the distance between moments. In the Heisenberg form the RKKY exchange Hamiltonian between two spins $\boldsymbol{S}_i$ and $\boldsymbol{S}_j$ is written as shown in Ref. 39:

$$\mathcal{H} = -2\sum_{i<j}^{N} J(R)\boldsymbol{S}_i \cdot \boldsymbol{S}_j \tag{10}$$

Next consider the interaction of the spins $\boldsymbol{S}_{ij}$ with the spins $\boldsymbol{s}$ of the surrounding conduction electrons to be delta function limited and of the form:

$$\mathcal{H} = -2A\delta(\boldsymbol{r} - \boldsymbol{R})\boldsymbol{S}_{ij} \cdot \boldsymbol{s} \tag{11}$$

It can be shown using equations (10) and (11) (derivation from Ref. 39) that the exchange coupling constant takes a form that is oscillatory in *R* and for the limit of large *R* is given by (where k_F is the Fermi wave vector):

$$J(R) = \frac{2A^2 m_e k_F}{(2\pi)^3 \hbar^2}\left(\frac{\cos(2k_F R)}{R^3}\right) \tag{12}$$

In the case of metallic multi-layer stacks [example, Co/Cu (1-5 nm)/Co], the oscillations are found to permeate the non-magnetic interlayer with a $1/z^2$ dependence where z is the distance from the magnetic/nonmagnetic interface. RKKY exchange is therefore unique in that it is the only type of exchange coupling that magnetizes the non-magnetic interlayer (intermediary). The exchange coupling strength is defined per unit interface area and takes a form dependent on the spacer layer thickness d given by:

$$J_{12}(z) = J_o \frac{d^2}{z^2} \sin(2k_F z) \tag{13}$$

In the research undertaken here, graphene provides the sea of conduction electrons to be polarized by either magnetic impurities or layers according to the RKKY exchange models outlined above. It has been predicted using theoretical simulations that randomly distributed magnetic impurities on a graphene surface can undergo RKKY coupling [39-41]. In some cases antiferromagnetic coupling between impurities on opposite graphene sublattices can result in band gap opening. Hopping from one sublattice to another normally does not flip the electron spin, but since neighboring impurities are antiferromagnetically coupled, it costs energy for an electron to move between sublattices. This leads to localization of spin polarized charges on the graphene sublattices, and a band gap opening in the area of magnetic impurities [42]. The gap size is predicted to be on the order of 0.1 eV depending on the exchange coupling strength, and is therefore tunable with temperature and external magnetic field.

Exchange coupling can however be difficult to measure experimentally, and it was not achieved in this study. Rather, this mechanism of gap opening is discussed because it was the main motivation for the study of metal/graphene systems. This is discussed further in Chapter 3 where

several sample architectures were developed to attempt to produce RKKY coupling and potentially open a band gap in graphene by this method.

1.2.4 Cobalt Mediated Oxidation of Graphene

The method developed and studied in this thesis is an alternative to chemical or exfoliation techniques that uses metal deposition to modify the band gap of graphene. Many related studies appear in the literature concerning work function doping of graphene for device applications, but a band gap was not revealed in these metal/graphene systems [43,44]. Indeed, work function engineering graphene is well known and has been used successfully to produce graphene contacts with a tunable work function, but again a band gap opening is not observed in these cases [45,46]. Studies involving transition metal clusters deposited on graphene have also not revealed a band gap opening using various techniques including scanning tunneling microscopy (STM) and X-ray spectroscopy methods [47-49]. Typically these studies are pursued to control magnetic characteristics of graphene or induce spin polarization, and are largely performed *in situ* to prevent perturbations such as oxidation.

Using graphene on SiO_2 substrates, it is possible to induce a controllable band gap using cobalt deposited on the surface. When a sub-monolayer of cobalt is deposited on the graphene, it does not etch or otherwise heavily damage the graphene. Exposing such a system to oxygen subsequently causes oxygen functional groups to form where cobalt has been deposited in a concentration proportional to the cobalt thickness, and also converts all Co to cobalt oxides. Through a mechanism similar to production of graphene oxide, the functional groups cause new sp^3 and sp^2 hybridizations, which can induce an opening of a band gap (Figure 1.10). Additionally,

electronic structure calculations of cobalt-graphene systems reveal a contribution from CoO alone that may also contribute to the band gap opening by localizing electronic charge near the Co clusters. The development and study of cobalt-graphene systems for band gap opening is the main subject of this thesis, with full analysis details reported in Chapter 3.

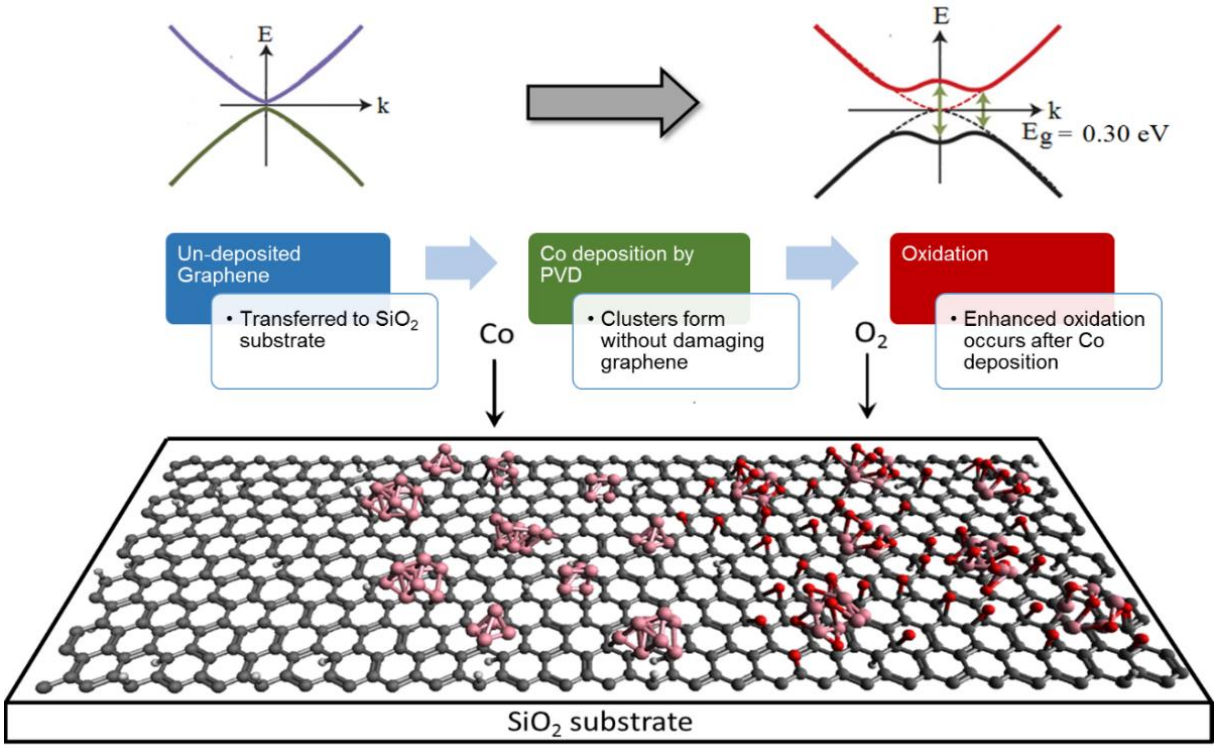

Figure 1.10. Schematic of band gap opening using cobalt-mediated oxidation.

CHAPTER 2

EXPERIMENTAL METHODS

2.1 A Brief History of X-ray Spectroscopy

Historically X-rays and X-ray spectroscopy have been studied since the evening of November 8th, 1895 when X-rays were first discovered and named by Röntgen [50]. Study on the interaction between X-rays and matter began nearly immediately, with over 1000 papers published on the subject in the first year [51]. Studies continued to progress at this rate, and in 1913 a technique to measure X-ray absorption was developed, followed by the first published X-ray absorption spectrum by Wagner in 1915 of a silver bromide emulsion. Up until this point, only the bright "white line" absorption features had been observed due to the measurement technique in use at the time; the transmission of X-rays through a sample was measured using photographic film. A systematic study of the various absorption and emission lines was undertaken in England, mainly by researcher Charles Glover Barkla over a period of many years, and ultimately published in 1918. The naming convention that is now commonly used for X-ray spectra defines the different electronic shells (typically in atomic notation) with new letters *K*, *L*, *M* etc. as shown in Figure 2.1, and was originally created by Charles Barkla during his studies [51]. Initially Barkla uncovered that the X-rays he could produce seemed to be of two types - one type was able to penetrate sheets of metal of a certain thickness, while the other was not and seemed to be blocked. Barkla initially named the more penetrating one type *A* and the less penetrating type *B*, but he then became concerned that even more penetrating types of X-ray radiation could be discovered. To avoid a potential naming problem, he renamed *A* and *B* to *K* and *L*, thus leaving room at the start of the

alphabet for more penetrating X-rays to be named *A* through *J*. As it turns out, no class of more penetrating rays was ever discovered, and the naming convention remains today. The conventional *K*, *L*, *M* lettering is used for X-ray spectroscopy measurements in this thesis as opposed to atomic notation.

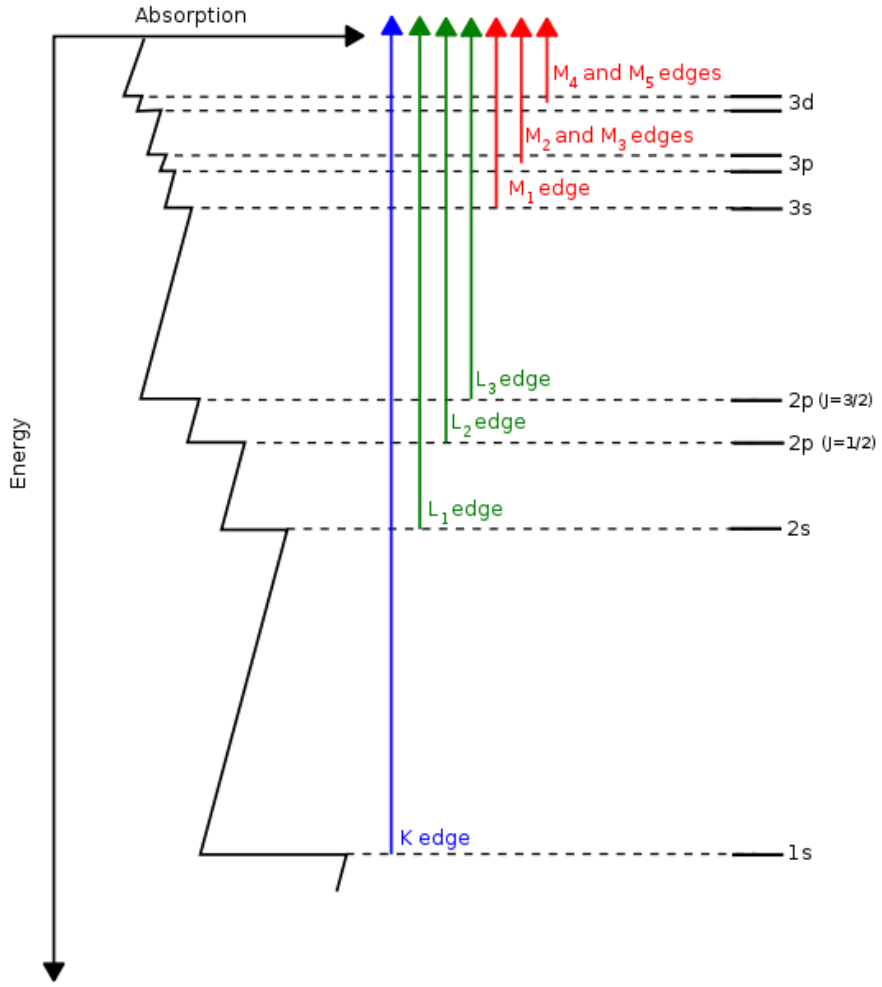

Figure 2.1. X-ray Absorption transition edges and their naming showing *K*, *L*, and *M* edges [52].

The first extended X-ray absorption fine structure (EXAFS) was observed by Wilhelm Stenström in Sweden, who published his results in his thesis studying the *M*-edges of rare-earth

metals in 1919. This was closely followed in 1920 by the observation that energy of a given absorption line may shift depending on the chemical environment and valence of the element. This made it necessary for further study to establish beyond any doubt the correct energy locations for various absorption edges according to the valence. This work was contributed by many researchers, largely by the work of Linus Pauling on ionic materials, published in 1929.

Most studies on X-ray absorption had been mainly experimental until 1920 when Walther Kossel offered an interpretation of X-ray absorption and fine structure from theory. He postulated correctly that absorption lines arise from electron excitations from inner shell orbitals to unoccupied outer shell orbitals due absorption of X-rays. Kossel's theory persisted until 1931 when a modification of the theory was introduced by Kronig to explain details of EXAFS oscillations by considering them as alternating forbidden and allowed bands in the DOS. Over the next several years Kronig went on to develop the theory of X-ray absorption in crystals and molecules, with contributions from many other physicists [51]. Kronig's theory was advanced experimentally over the next 5 years by several physicists including Dirk Coster, Douglas Hartree, and Kronig's PhD student, Hendrick Petersen. This work was also largely contributed to by experimental advances in detectors and monochromator crystals that allowed for much higher measurement resolution. Several other breakthroughs are noted in the next two decades up to the 1950's including ionization chambers becoming standard equipment for transmission X-ray absorption. This resulted in measured spectra taking the form seen today by plotting absorption cross-section ($\mu(E)$) vs. incident photon energy. With numerous contributions and changes made by other scientists, Kronig's theory was developed into the theoretical framework used today to understand the interaction of X-rays with matter. For a full account of the history of X-ray spectroscopy and X-ray absorption, refer to Ref. 51.

2.1.1 Synchrotron Facilities and Beamlines

To perform X-ray spectroscopy efficiently, a bright, monochromatic source of X-rays is desirable. Some experiments can be successful using a laboratory source, but most modern measurements are accomplished at a synchrotron facility. Without going into great detail, a synchrotron produces X-rays by accelerating bunches of electrons to near relativistic speeds around a nearly circular path under high vacuum. When the bunches meet a corner in the nearly circular path, their trajectory is changed using magnetic fields, causing the emission of intense electromagnetic radiation in a broad energy range. This is then the basis of X-ray production using a synchrotron facility. In addition to magnets at the bends in the path, special equipment may be used along the straight sections to also produce radiation, called insertion devices. An insertion device typically contains an array of magnets with alternating magnetic field direction, with the two types used called undulators and wigglers. The specific details of different synchrotron facilities may vary in terms of what experiments can be performed, but the basic functionality and insertion devices are the same. Near or attached to each insertion device may be one or more experimental stations that make use of the X-ray light for experiments, called beamlines.

X-ray radiation provided by most modern 3rd generation synchrotron facilities may range from 10 eV – 50 keV depending on the construction of the facility. The energy range of X-rays chosen depends on the specific element(s) one wishes to probe. Examination of elements in this study required only soft X-rays which typically range from about 100 eV – 5 keV. X-rays provided by a synchrotron facility can also be tuned (very accurately) in energy using mirrors and other optics present as part of each beamline. Due to the lower energy and longer wavelength of soft X-rays,

they do not penetrate deeply into matter, and in fact are heavily absorbed by most materials including air at atmospheric pressure. For this reason soft X-ray beamlines at synchrotrons employ high vacuum chambers to perform spectroscopy measurements and avoid significant X-ray attenuation that may occur. Samples to be measured are transferred into the high vacuum chambers and mounted on a *xyz* stage that can be freely moved or rotated in or out of the X-ray beam.

Measurements reported in this thesis were performed at two facilities: the Canadian Light Source (CLS) at the University of Saskatchewan, SK, Canada, and the Advanced Light Source (ALS) in Berkeley, CA, USA. At these facilities many beamlines are available, and for this thesis measurements were performed at either Beamline 8.0.1 (BL8) at the ALS, or the Resonant Elastic-Inelastic X-ray Scattering (REIXS) beamline at the CLS. BL8 is a soft X-ray beamline known for efficiency and reliability, with an X-ray fluorescence endstation that can perform both X-ray absorption (XAS) and X-ray emission (XES). X-rays are generated at this beamline using an undulator to achieve an energy range of 100-1200 eV, further tunable using a spherical grating monochromator, and arriving at the sample with a spot size of 100 x 1000 μm [53]. The BL8 endstation is equipped with both a channeltron fluorescence detector and a picoammeter to measure bulk sensitive total fluorescence yield (TFY) and surface sensitive total electron yield (TEY). BL8 also employs a spherical grating spectrometer in Rowland circle geometry to obtain XES measurements. Photons emitted from the sample are collected in the spectrometer using an area-sensitive detector to detect energy and intensity. The resolving power of the spectrometer depends on the energy range of X-rays used, and for this study it ranged from 500-1000.

The REIXS beam line at the CLS is similar to BL8 in that it can perform both XAS and XES measurements. It uses an elliptically polarized undulator as the insertion device with an energy range of 80 – 2000 eV, and a spot size of 60 x 10 μm at the sample. REIXS also employs a grating

spectrometer for XES measurements similar in operation to BL8, but with significantly higher operational energy resolution. In the energy range for this study, the resolving power was 2000-2500 [54]. During this thesis research, this beamline was undergoing commissioning, but was fully functional. Unless stated otherwise, X-ray spectroscopy measurements reported here were completed at room temperature at 10^{-7} torr or better (10^{-8} for XES) with linearly polarized X-rays. Samples were affixed to the sample plate using double sided carbon tape, and in some cases extra tape was used around the top surface edges to ensure good conduction between the samples surface and the plate.

2.1.2 X-ray Absorption Spectroscopy (XAS)

X-ray absorption spectroscopy was the first technique to be developed to study the interaction of X-rays and matter. XAS provides a measure of the partial density of unoccupied electronic states relative to incident X-ray energy. The unoccupied states are probed by first exciting a core-level electron into previously empty orbitals through absorption of X-ray, leaving a positively charged hole in core states. It is important to note that Fermi's Golden Rule applies, and the density of states determined from an XAS experiment is strongly influenced by the presence of the core hole, and therefore does not strictly represent the ground state DOS. There are three common experimental arrangements used to measure XAS (the number of core holes created): transmission, TEY, and TFY (Figure 2.2). Transmission directly measures absorption by simply detecting the X-ray attenuation caused by a sample placed in the beam path. Detectors commonly in the form of ion chambers are placed before and after the sample to directly measure the absorption. This arrangement is used often with hard X-rays that easily penetrate through thin samples, but the

requirement of full penetration can create a disadvantage in that samples that are too thick cannot be measured. Furthermore, an additional insidious complication occurs for sample thickness near the threshold of measurement (typically 100 nm) for complete attenuation. Such a sample may not stop all X-rays at all energies in the spectrum, leading to suppression of some absorption peaks or otherwise unphysical intensity related artifacts.

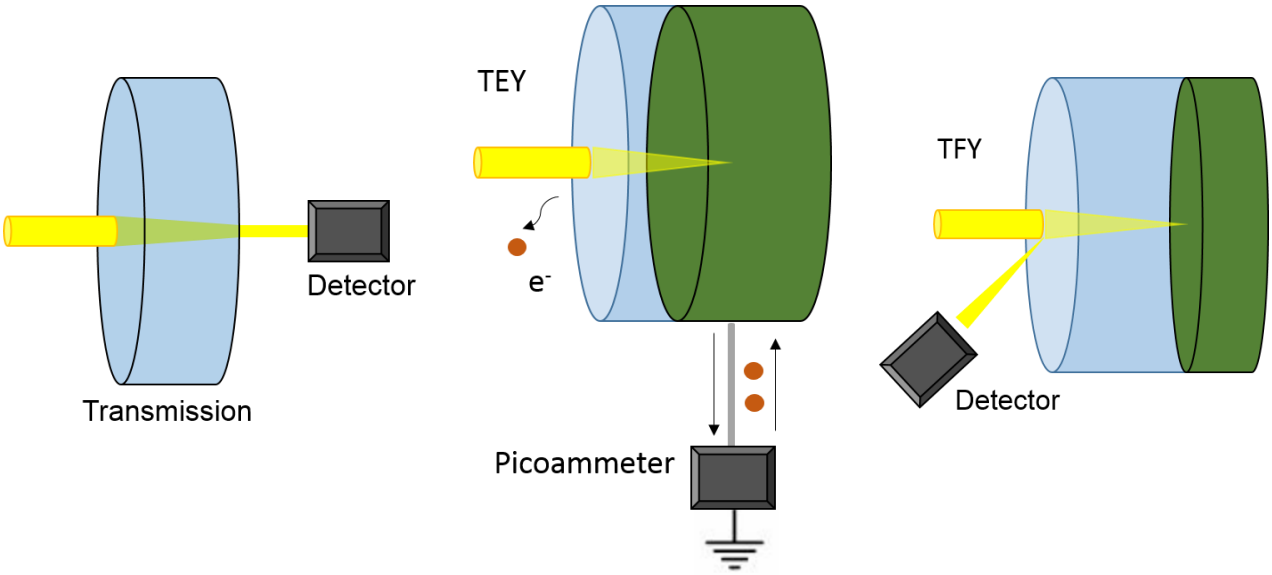

Figure 2.2. Schematic representations of common XAS detection techniques where the blue region represents the approximate probing depth of each technique. Transmission (left) measures absorption by detecting the fraction of photons absorbed by a thin sample. Electron yield (middle) probes the sample surface by detecting electrons ejected from the sample surface, or by measuring a current that replenishes the charge on the sample. Total fluorescence yield (right) detects fluorescence photons that result from relaxation after an absorption event.

A typical transmission measurement is shown in Figure 2.3 of cobalt nanoclusters on graphene measured at the Hard X-ray Microanalysis (HXMA) beamline at the CLS. In general XAS spectra have three areas defined in the figure. The near edge region is often referred to as near edge X-

ray absorption fine structure (NEXAFS) or X-ray absorption near edge structure (XANES). After the near edge, the spectrum may be extended to collect further data at higher energies, often called the Extended X-ray absorption fine structure (EXAFS). Much useful information can be derived from the EXAFS region with careful analysis, including the number of nearest neighbor atoms and the bond lengths to those atoms. However, analysis of the EXAFS oscillations is not trivial and was not used as part of this study. Measurements discussed in this study focus on the NEXAFS region of absorption measurements which contains other useful information about the bonding environment of the element being probed.

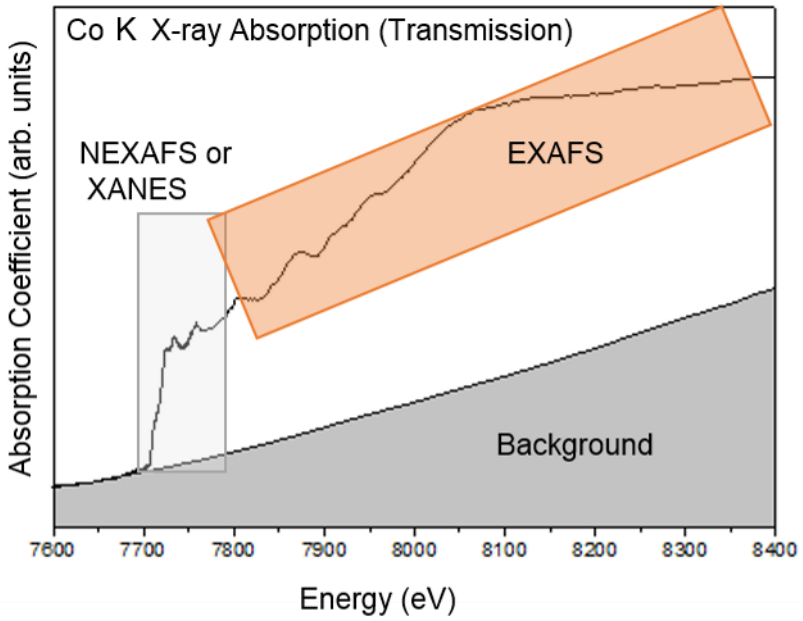

Figure 2.3. A representative X-ray absorption measurement of Cobalt clusters with the three main regions labeled.

TEY measurements are similar to transmission in that a measure of the absorption cross section is obtained, but by an indirect method. After an X-ray absorption event, the system is in a highly excited state that will decay over a short time scale to its ground state by releasing energy. First a

core electron is excited to unoccupied states by absorption of an X-ray, leaving a positively charged hole. This hole will be filled by an electron from the occupied states, releasing energy as a photon or transferring it to another electron. The receiving electron or the photon may escape the sample surface. In practice it is found that the number of electrons or photons produced is proportional to the total number of core holes created. In the case of TEY the number of electrons ejected is indirectly measured by detecting a positive current flowing from the sample to an electrical ground to return the sample charge to neutral (typically done with a picoammeter due to the small current values). This technique is effective when the sample and sample plate are electrically isolated, typically in a vacuum chamber. A disadvantage here is that TEY is a total yield technique, meaning it detects all electrons ejected from the sample, regardless of their origin. This may be a significant consideration when considering the probability of various absorption and relaxation events in the sample under study. Not all electrons ejected from the surface may arise from core levels of the element that one intended to excite. Electrons can also be excited from lower energy orbitals of any element in the sample – this is the origin of the background signal observed in Figure 2.3. Due to this, in practice TEY absorption spectra may contain artifacts or a strongly varying background that is dependent on the specific materials in the sample or its electrical properties. Furthermore since the TEY signal depends on current flow, if the sample or its substrate are strongly insulating, a net positive charge can be developed on the sample. This can cause subtle artifacts in the spectra such as a slowly varying non-linear background. Lastly, for electron yield techniques, the probing depth is only a few nanometers due the short mean free path of Auger electrons that must escape the sample surface to be detected (~2-20 nm of the sample surface) [55]. A relevant example of artifacts in TEY spectra can appear because of a method commonly used to normalize measured absorption to remove fluctuations in the incident beam. Across the energy

range of a measurement, the incoming flux may vary for many reasons dependent on the function of the synchrotron facility, which is accounted for by measuring the flux with a gold mesh upstream of the sample chamber. Now consider that although soft X-ray beamlines are kept in high vacuum (10^{-8} - 10^{-9} torr), contamination with common elements is unavoidable. Carbon in particular is ubiquitous and may arrive through the sample garage from the hands of experimenters or through outgassing from the samples themselves while they are measured. Carbon materials in the beamline vacuum chambers can be adsorbed onto the mesh, and inadvertently absorb X-rays meant for the mesh, causing fluctuations in the flux recorded by the mesh around the absorption edge of the contaminant. Figure 2.4 shows an example of the mesh current at the carbon and oxygen K absorption edges. A nonlinear variation in the flux recorded by the Au mesh is clearly evident at near the C *K*-edge, which is even more severe at the O *K*-edge. Under ideal conditions, these fluctuations are much smaller than the recorded absorption from the sample, but this background can be an issue for poorly conducting or very dilute samples.

To avoid the issues of total yield, partial yield techniques have been developed that employ an energy selective detector to cut off all detection events that do not arise from the desired core level excitation. Partial yield techniques were not used in this study to collect absorption spectra, due to availability and experimental considerations, so they will not be further discussed here.

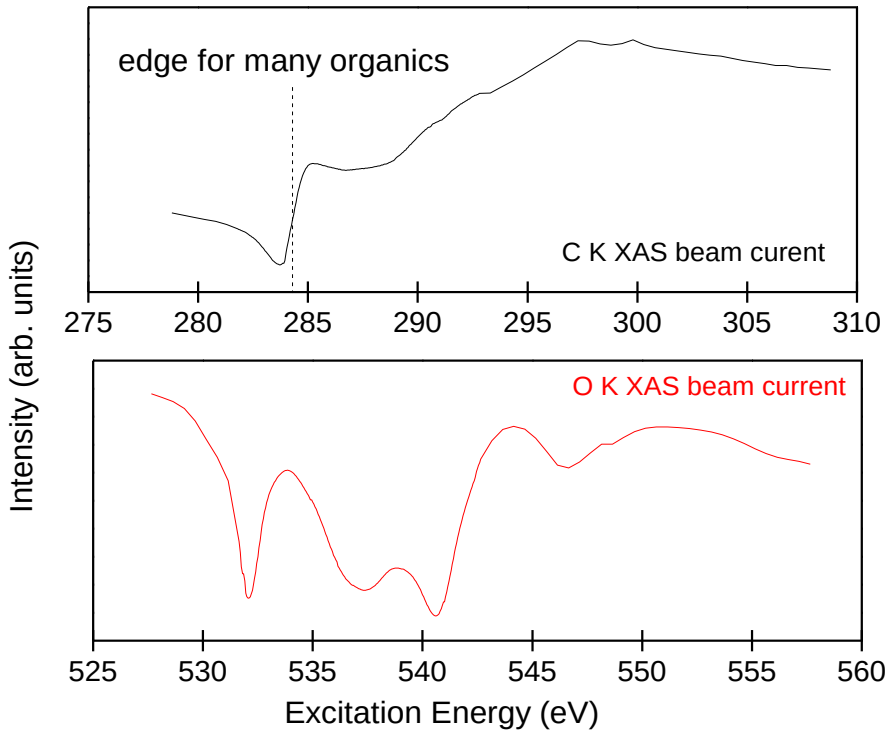

Figure 2.4. Beam current measurements at the carbon and oxygen *K*-edges. Similar to TEY, photons resulting from relaxation events can also be detected.

Collecting all emitted photons and integrating them with respect to incoming X-ray energy is termed total fluorescence yield (Figure 2.2). Practically photons have a much longer mean free path (~100 nm in the soft X-ray regime) and are emitted isotropically from the sample. Therefore only a fraction of the emitted fluorescence is captured by the detector, but the fraction of detected photons is still proportional to the number of core holes created. TFY however is not without other practical considerations – this technique can suffer from self-absorption effects in high concentration samples when using soft X-rays [55]. Self-absorption effects occur when the penetration depth of X-rays varies strongly near an absorption edge. This can cause artificial suppression of absorption peaks and a strongly varying background signal. In TEY, a similar

saturation effect can occur when the ratio of absorbed X-rays to ejected electrons approaches unity, causing the absorption cross section to be independent of energy. Effectively, the measured spectrum plateaus to a straight line as the detector is saturated with counts. This problem can be avoided by careful sample preparation and appropriate experimental setup, and techniques also exist to correct TFY data affected by self-absorption after completion of measurements [55].

When deciding which technique is more appropriate, one must consider the samples under study and the element edges that are to be probed. Figure 2.5 displays the theoretical fluorescence yield plotted vs. atomic number. From the plot, it is clear that the yield from *K*-shell excitations elements with atomic number below about 20 is very low, making TFY measurements of these elements potentially more difficult for dilute samples.

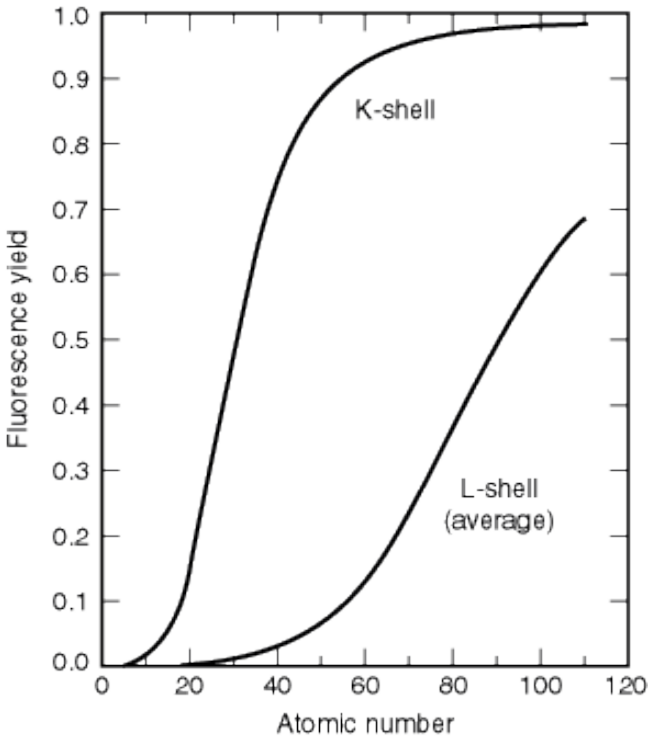

Figure 2.5. Fluorescence yields for K and L shells for $5 \leq Z \leq 110$. The L-shell curve the average of effective yields from L_1, L_2 and L_3. This data adapted from Ref. 56 and appears in the X-ray data Booklet [57].

Aside from the yield, one must consider the density of states that is actually recorded from a single measurement. A given XAS measurement will provide a picture of the partial density of states favoring the orbital transition with the highest probability. A set of general rules can be derived that govern which transitions are more probable, or deemed "allowed" or "forbidden", based on a theoretical case. Called "transition selection rules", these rules can be used to describe electronic transitions such as those in X-ray spectroscopy, and specify the possible transitions among quantum levels due to absorption or emission of electromagnetic radiation. To derive a set of selection rules, first consider that incident electromagnetic radiation presents an oscillating electric field that can interact with an electron. For X-rays the simplification of considering only a dipole allowed transition can be made because soft X-rays have relatively long wavelengths compared to orbital radii under study. Electric quadrupole-allowed, or magnetic dipole-allowed transitions can also occur, but the transition probability in these cases is much smaller than the electric dipole. A transition dipole can be defined to model this transition with the dipole operator given by $\mu = \hat{\varepsilon} \cdot r$. This simplification is known as the electric dipole approximation because it simplifies that operator by removing the exponential dependence. The transition probability before approximation is given by [58]:

$$T_{i\to n} = \frac{2\pi e}{\hbar m^2 c^2} |A|^2 \left| \langle \phi_f \left| e^{i(\omega/c)(\hat{\mathbf{n}}\cdot\vec{\mathbf{r}})} \hat{\varepsilon} \cdot \vec{p} \right| \phi_i \rangle \right|^2 \delta(E_n - E_i - h\omega) \qquad (12)$$

Where $\hat{\varepsilon}$ and $\vec{\boldsymbol{r}}$ are the polarization and propagation directions and $\vec{A}$ is the vector potential of the radiation field. If we consider that experiments will be performed with soft X-rays and on

elements with small atom sizes (on the order of 0.5 -1 Å), then the exponential term can be approximated by the first term of its expanded series.

$$e^{i(\omega/c)(\hat{\boldsymbol{n}}\cdot\vec{\boldsymbol{r}})} = 1 + i\left(\frac{\omega}{c}\right)(\hat{\boldsymbol{n}}\cdot\vec{\boldsymbol{r}}) + \cdots \tag{15}$$

$$T_{i\to n} = \frac{2\pi e}{\hbar m^2 c^2}|A|^2\left|\langle\phi_f|\hat{\varepsilon}\cdot\vec{p}|\phi_i\rangle\right|^2\delta(E_n - E_i - h\omega) \tag{16}$$

Taking $\hat{\varepsilon}$ for example along the x-axis, $\langle n|p_x|i\rangle$ can be calculated using the commutation relation:

$$[x, H_O] = \frac{i\hbar p_x}{m} \tag{17}$$

$$\langle\phi_f|p_x|\phi_i\rangle = \frac{m}{i\hbar}\langle\phi_f|[x, H_O]|\phi_i\rangle \tag{18}$$

$$\langle\phi_f|p_x|\phi_i\rangle = imw_{ni}\langle\phi_f|x|\phi_i\rangle \tag{19}$$

With the dipole approximation, we can now write the expression for a single electron transition with initial (ϕ_i) and final state (ϕ_f) wavefunctions as in equation (20).

$$T_{i\to n} \propto \left|\langle\phi_f|\hat{\varepsilon}\cdot r|\phi_i\rangle\right|^2\delta(E_n - E_i - h\omega) \tag{20}$$

Using the single electron excitation approximation makes it possible to rewrite the initial state wavefunction as a core wave function, and the final state wave function as a free electron wave function. That is, with these wavefunctions constructed, allowed transitions occur according to whether or not the matrix elements of the dipole moment operator (along the direction $\hat{\varepsilon}$) are non-vanishing. When the transition operator vanishes, the transition is deemed forbidden. However,

this is not to say that it cannot occur, but rather will only occur at a much lower probability compared to an allowed transition.

To determine the conditions for allowed or forbidden transitions, the initial and final state wavefunctions must be constructed. These wavefunctions will contain both a spherical and radial components and depend on quantum numbers for angular momentum (ℓ), magnetism (m), spin (s). A full detail of the derivation will not be given here, but can be found in many quantum mechanics texts including Ref. 58. Total angular momentum ($J=L+S$) should also be considered when there is significant spin-orbit interaction (L-S or Russell-Saunders coupling) affecting the transition, rather than just L and S. An additional restriction is also when J or L is zero, ΔJ or ΔL, respectively, cannot be zero. The parity of two states is another important factor in determining whether or not a transition between them is allowed by emitting or absorbing a photon. Rigorously, for a dipole transition the parity must change (odd or even), as given by $(-1)^{\ell}$. So ℓ determines odd or even states, and hence dipole transitions are allowed for $s \leftrightarrow p$ or $p \leftrightarrow d$, but not allowed for $s \leftrightarrow s$ or $s \leftrightarrow d$ by parity. These conditions lead to a set of selection rules for allowed electric dipole transitions, shown in Table 2.1**.**

Electric Dipole Selection Rules	
ΔJ	0, ±1
ΔM_J	0, ±1
ΔL	0, ±1
ΔS	0
$\Delta \ell$	±1
parity	$(-1)^{\ell}$

Table 2.1. Electric dipole selection rules where uppercase letters refer to quantum numbers for multiple electrons.

The selection rules defined above with *J*, *L*, and *S* quantum numbers are appropriate for lighter elements where the interactions between the orbital angular momenta of individual electrons is stronger than the spin-orbit coupling between the spin and orbital angular momenta. However, in heavier elements (such as rare earth metals) with larger nuclear charge, spin and orbital angular momenta of individual electrons may couple to form individual electron angular moment. In this regime, the *L*-*S* coupling described above is no longer sufficient to describe the system. The new coupling between electrons is referred to as *j*-*j* coupling where $j_i = L_i + S_i$ for each electron, with an overall angular momentum defined as the sum of individual total angular momenta $J = \sum_i j_i$. This gives rise modifications to the above selection rules that should be considered when heavier elements are under study.

In the dipole approximation, the absorption spectrum should be the partial density of unoccupied states projected onto the absorbing site. Some broadening of the spectra will occur from three sources: the lifetime of the core hole, the lifetime of the excited state, and instrumental broadening. Lifetime broadening effects occur due to the finite life-time of an excited state which leads to an uncertainty in its energy. The amount of lifetime broadening therefore also depends on the element and edge.

This study reports three different element edges, C *K*, Co $L_{2,3}$, and Cu $L_{2,3}$. For X-ray measurements we can determine beforehand from selection rules what projection of the density of states is represented. For carbon, the 1*s* core level is not affected by spin-orbit coupling, so the transition is governed by $\Delta\ell = \pm 1$, $1s \rightarrow 2p$. Therefore C *K* XAS spectra represent unoccupied 2*p* states without significant perturbation from spin-orbit interaction. Effectively, the presence of the core-hole in the final state does not significantly perturb the shape and energy location of *K*-edge spectra compared to *L*-edge.

Co XAS strictly represent 3*d*4*s* unoccupied states according to selection rules, but in practice it has been found that $2p \rightarrow 3d$ transitions dominate the spectrum [59]. Cu $L_{2,3}$ XAS also represents 3*d*4*s* unoccupied states, but due the valence electron configuration of Cu with a filled *d*-shell ($[Ar]3d^{10}4s^1$) these spectra are dominated by $2p \rightarrow 4s$ transitions. Notably for these metal edges, there is an energy splitting between the L_3 ($2p_{3/2}$) and L_2 ($2p_{1/2}$) edges. This splitting is caused by the 2*p* spin-orbit interaction, *(J = L+S, L*=1, *S*=±*1/2, J= 3/2, 1/2*) and it increases with atomic number in the transition metal series because it is directly proportional to nuclear charge and inversely to the orbital radii, ranging from 5 eV for Sc to 20 eV for Cu [59]. The spectral shape of *L*-edge spectra is also largely determined by the crystal field produced by nearest-neighbor atoms to the one being probed, which is further discussed in Chapter 2.2.1 in the context of electronic structure simulations**.**

The polarization of X-rays used also has an effect on the shape of the spectra obtained, particularly in the case of graphene. All measurements in this study excluding those discussed in Chapter 5 used linearly polarized X-rays. The angle of incidence in this case has an effect on the relative intensities of the π* and σ* resonance features for structures that are nearly planar. Consider Figure 2.6 showing a benzene ring. The π* and σ* states are localized perpendicular to and along the plane of the ring respectively. The angle of incidence of incoming X-rays (0^o for normal to the substrate surface) determines the coupling of the linear polarization vector of the X-ray with the orbital cross section. When a structure such as graphene is resonantly excited by X-rays, the observed absorption cross section is dependent on the projection of the X-ray polarization vector onto the final state orbitals involved in the transition [60]. Practically this means π* intensity will be maximized at 90^o (grazing incidence) while σ* is minimized. Using this effect, one can preferentially probe π* or σ* states using linear polarized X-rays and varying the angle of

incidence. To effectively view all peaks in planar materials such as graphene, an angle of incidence of 35-55^{o} is reasonable.

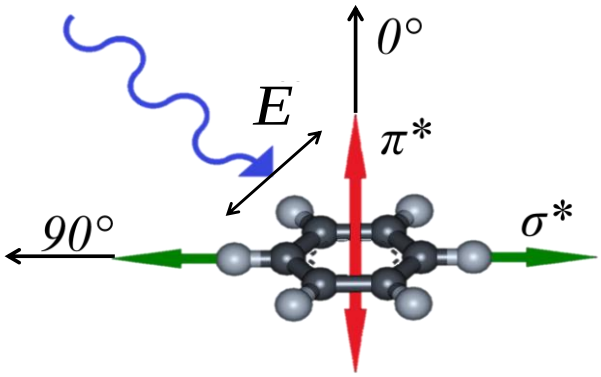

Figure 2.6. Schematic representation of π* and σ* orbital locations. Linearly polarized X-rays can preferentially excite into π* or σ* states by changing the angle of incidence.

2.1.3 X-ray Emission Spectroscopy (XES)

In addition to probing the unoccupied states, XES can be used as a complementary technique to probe the partial density of occupied states. The simplest form of this measurement involves non-resonant excitation where core level electrons are ejected from the system entirely as photoelectrons. As mentioned above for XAS, core holes created by an absorption event can be filled by valence electrons in occupied states, releasing energy that may take the form of X-ray photons. In contrast to the case of TFY, these photons may be collected in an energy dispersive detector to measure the fluorescence intensity as a function of emitted energy. In non-resonant XES, the incoming X-ray energy is fixed at a value well above the absorption edge of the element in question (for example at 320 eV for a carbon measurement) to promote core level electrons beyond bound unoccupied states as photoelectrons. If the core hole is filled by a weakly bound valence electron, the spectrum will represent the occupied density of states. XES is therefore

complimentary to XAS, and the two measurements can be used in conjunction to provide a full picture of the partial density of occupied and unoccupied states for a given transition. XES is also bulk sensitive similar to TFY because it detects emitted photons, and due to the lower energy of emitted photons (below the absorption edge), self-absorption is not as much of a concern as for TFY. XES spectra can also be acquired using a resonant transition to unoccupied bound states. This type of measurement can provide additional information about specific occupied states in a material, but has not been used in this study.

Unfortunately XES measurement capabilities are not as easy to access as XAS due to realistic equipment cost and size considerations. XES requires high resolution spectrometers that expensive to implement and as well as physically large. Fortunately both BL8 and REIXS have high resolution XES spectrometers available, which were used for measurements in this thesis.

A final note on X-ray absorption and X-ray emission measurements concerns the energy calibration of the measurements. Although the monochromator can have a very high energy resolution (0.01 eV), the absolute energy of the incident beam varies over time from 1 to up to 100 eV depending on the energy range. Therefore, as part of standard practice very well-known materials with well-defined spectral peaks are used a calibration samples to correct for the absolute energy shift. However, even these materials have spectral features that subject to broadening, usually with a width of 0.1 – 0.5 eV at soft X-ray energies. This calibration procedure is then the main source of uncertainty in the energy location of spectral peaks and edges – the finite width of the peaks creates an uncertainty in the calibration itself of 0.05-0.1 eV.

2.1.4 X-ray Photoelectron Spectroscopy (XPS)

The third and final X-ray spectroscopy technique discussed in this thesis is photoelectron spectroscopy. XPS is related to TEY in that it measures electrons ejected from the sample surface due to the photoelectric effect or Auger electrons. But rather than measure their charge indirectly, XPS measures their kinetic energy directly with an energy dispersive detector. This is advantageous over XES in that energy dispersive detectors for electrons are much more compact than X-ray spectrometers. In XPS, X-rays at a fixed energy ($h\upsilon$) excite electrons that are then ejected from the surface at a kinetic energy E_{Kin}. XPS probes the occupied states by counting the number of electrons at an electron binding energy E_B, which is determined by the energy conservation equation (21) (where φ corrects for the work function of detector and sample) [61].

$$E_B = E_{Kin} - h\upsilon + \phi \tag{21}$$

XPS measurement equipment can be much more compact than XES in that not only is the detector typically much smaller, but a high brightness synchrotron X-ray source is not strictly required. In fact the measurements reported in this thesis were completed with a laboratory setup using an Al X-ray source emitting photons from the $K\alpha$ excitation (1486.6 eV). The spectrometer used was a PHI XPS Versaprobe 5000 spectrometer (ULVAC-Physical Electronics, USA) with an energy resolution of $\Delta E \leq 0.5$ eV and 100 x 100 μm spot size. The measurements are of two types; survey spectra primarily used to determine the elements present and probe their edges, and valence band spectra that probe only the low energy valence orbitals in terms of electron binding energy. By virtue of the fact that XPS detects electrons that must escape the sample, it is a very surface

sensitive technique, probing a similar 2-20 nm depth as with TEY. Therefore, most bulk samples must be cleaved carefully to ensure a clean surface prior to measurement. Luckily graphene is a 2D material, so the probing depth is not a concern for most of the measurements in this study. XPS transitions often use a three letter notation where the first letter indicates the state with core hole, the second the state is the origin of the electron that fills the core hole, and the third is the origin state of the emitted Auger electron. For example, *LMM* notation indicates the Auger transition where the core hole is in *L*-states, and both the relaxing and emitted electron originate from *M*-states.

In this study the XPS data was measured at the Ural Federal University, Yekaterinburg, Russia and contributed by Dr. Andery I. Kukharenko, Dr. Seif O. Cholakh, and Dr. Ernst Z. Kurmaev.

2.2 Theoretical Simulations of Experimental Measurements

2.2.1 Multi-Ligand Field Theory (MLFT)

As discussed above, the single electron picture is used to derive selection rules for X-ray transitions, and can in some cases be a good approximation such as a *K*-edge excitation where the electrons are highly localized and multiplet effects are minimized. It has been found experimentally however that the single electron picture does not well represent many other spectra, namely the $L_{2,3}$ edge of transition metals [62]. The reason such simulations deviate from experiment is because they fail to account for the overlap of the core wave function with the valence wave functions (That is, the 2*p* and 3*d* wavefunctions for $L_{2,3}$ spectra). Of course this occurs even in the ground state, but it is minimized because all states are filled with electrons and so can be approximated by the electron charge. In the case of XAS the final state contains a

partially filled core hole that can significantly perturb the density of states such that the spectrum cannot be reliably simulated in the single electron picture without including atomic multiplet effects. Spin-orbit coupling in 3*d* states of transition metals is also a consideration that causes splitting of the 3*d* envelope into closely degenerate states. One must also consider the effect of ligands that are bonded to the transition metal under study. This is accomplished using the crystal field model where the transition metal is modeled as an isolated atom surrounded by a distribution of charges that mimic the system around it [63]. The crystal or ligand field created by neighboring ligands interacts with the metal *d*-orbitals, causing them to shift in energy and lose degeneracy. The symmetry and strength of the local ligand field therefore has a strong effect on the final energy locations of the split *d*-states. A calculation code that takes into account all of these effects has been used in the form of multi-ligand field theory (MLFT) calculations to simulate Co $L_{2,3}$ XAS spectra. MLFT simulations use a single impurity Anderson model, including multiplet effects, crystal field splittings, and hybridization with ligands. The simulations employ a model Hamiltonian approach where adjustable parameters are fit to the experiment. These parameters include crystal field splitting parameters (10Dq, Dσ, Dτ), symmetry-dependent hopping integrals (V_e, V_{t2}), charge transfer energy (Δ), the difference between the onsite Coulomb repulsion and the core hole potential ($U-Q$), and the ligand bandwidth (W) and shape [63-65]. As a final note, the MLFT simulations in this study were contributed by Brett Leedahl using a code developed by the Beam Team research group at the University of Saskatchewan.

2.2.2 Density Functional Theory using WIEN2K and SIESTA

In addition to MLFT calculations, the graphene band structure was simulated using the density functional theory (DFT) code WIEN2K. DFT is a theoretical approach that uses approximate solutions to the many-body Hamiltonian. WIEN2K is such a DFT code that is also full potential and all electron in that it uses the true potential of atomic nuclei and calculates explicitly the behavior all electrons in the system. WIEN2K is a powerful tool that can determine many material properties including but not limited to relative stability, chemical bonding, relaxation of atoms, phase transitions, electrical, mechanical, optical and magnetic behavior. Without going into detail, the DFT method focuses on computing a ground state density for the entire system that contains information about all ground state properties of the system. DFT was developed by Hohenberg, Kohn and Sham in the mid-sixties and is a popular theoretical approach used by many computation codes [66,67]. The main parameters one considers are the identity and location (in 3D space) of the atoms in the structure to be calculated, the basis sets, and the exchange correlation functional. The exchange-correlation functional is a mathematical approximation that accounts for the exchange and correlation interactions between electrons. These functionals are independent of the particular material studied, so any that is deemed suitable may be chosen. The orbitals of the atom are represented in the basis sets, which are effectively a linear combination of functions. Many different basis sets are available of varying complexity depending on the system and application under study.

DFT calculations in this study were used to compute the band structure of graphene when Co has been deposited on its surface. However, the calculation results are supplementary to the experimental results, and as such a full treatment of the DFT method will not be discussed here.

Several texts are available that provide full details of the DFT procedure [68,69], as well as about WIEN2K specifically [70]. As with the MLFT simulations, WIEN2K calculations were contributed by Adrian Hunt and Eamon McDermott who were part of the Beam Team research group at the University of Saskatchewan.

In addition to WIEN2K, DFT calculations were performed to investigate the electronic structure of graphene on copper using the pseudo-potential code SIESTA. Some DFT codes utilize a pseudo-potential to represent the Coulomb potential of the atomic nuclei including the contribution from core states. Well-constructed pseudopotentials can describe ground state properties with similar accuracy to a full potential approach such as WIEN2K, but with potentially shorter calculation time. SIESTA was used to model several graphene-copper systems for comparison to XAS measurements. Specific details of the methods used to calculate graphene systems can be found in refs. [71] and [72]. SIESTA calculations were contributed by Dr. Danil W. Boukhvalov as part of a study investigating the use of graphene as an oxidation barrier on copper.

2.3 Raman Spectroscopy

For surface characterizations of many samples, Raman spectroscopy is an ideal choice with many high quality commercial laboratory based Raman spectrometers available. Since the collection of the first Raman spectrum of graphene in 2006, Raman spectroscopy has become one of the most popular techniques for the characterization of graphene and many other types of materials including fullerenes, nanotubes and polyconjugated molecules [73]. The resonance peaks observed in Raman spectra result from low energy excitations to vibrational states, which are typically excited using photon scattering with light from a low power laser with a typical spot size

of 10 - 50 μm. As indicated by Figure 2.7, several interactions are possible; elastic Rayleigh scattering of photons is the most probable, with a remaining small photon fraction causing excitations of electrons at or near the ground vibrational state to higher states. When this electron relaxes to the ground state, the outgoing photon may scatter off of phonons (emitted from holes and electrons in the sample), and be shifted in energy (frequency), with a positive or a negative shift referred to as Anti-Stokes or Stokes scattering, respectively. A spectrometer observing the scattered light may then measure the frequency shift of scattered photons relative to the initial beam. The number of scattered photons at a measured frequency shift is then proportional to the number of vibrational states associated with a given phonon dispersion mode.

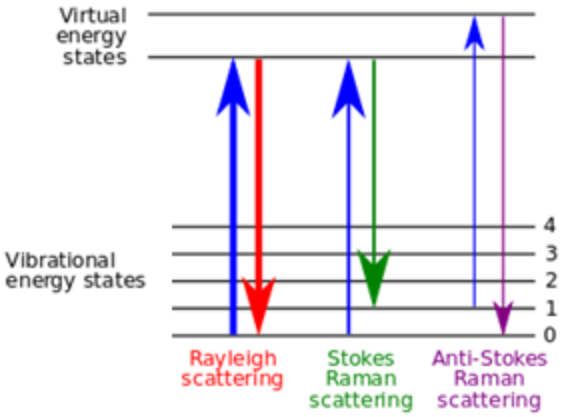

Figure 2.7. Schematic of the different Raman scattering pathways. Adapted from Ref. [74].

To fully interpret the Raman spectrum of graphene, one must consider which modes are Raman-active according the phonon dispersion in graphene. Not all phonon modes can couple to incoming photons and induce Raman Scattering. For a given mode or vibration to be Raman active, it must have anisotropic polarizability. When an electromagnetic wave (light) is incident on the material, a dipole moment may be induced by interaction with the electric field of the wave. This induced

dipole may emit or scatter light at the optical frequency of the incident light. In the case of isotropic polarizability, the phonon mode oscillates at the frequency of the incident electromagnetic radiation and only Rayleigh scattering results. In order to observe a Raman shift, the polarizability must change due to a vibration, causing inelastic scattering of the incident light, and a frequency shift that may be measured. The spectral peaks in a Raman spectrum then represent only those vibrational modes that experience a change in polarizability, and can therefore inelastically scatter light. Recall that the unit cell of graphene contains two atoms (Figure 1.4), resulting in six phonon dispersion bands, in which three are acoustic branches (A), and the other three are optic (O) phonon branches They are classified by the direction of their vibration as out-of-plane (o) or in-plane (i) to the graphene sheet, and longitudinal (L) or transverse (T) according to vibrations parallel with or perpendicular to the *A*–*B* carbon–carbon bond direction [75]. The six phonon dispersion curves in graphene are therefore assigned the labels LO, iTO, oTO, LA, iTA, and oTA. Of the six modes, only the LO and iTO modes are degenerate and Raman active, and through first and second order processes they produce the peaks seen in Raman spectra of graphene. The in-plane iTO and LO optic modes correspond to the vibrations of the sublattice *A* against the sublattice *B* and are associated with the *G*-band. The *G*-band may broaden due to defects, which is shown by comparison to C_{60} powder in Figure 2.8. This sample of C_{60} shows large broad peaks that signify amorphous carbon byproducts that are produced by breakdown of the C_{60} under the laser light. For some materials that are highly absorbing, even low power lasers (0.1 – 0.5 mW) can be damaging; fortunately this is not the case for graphene which has high thermal conductivity and is also nearly transparent to the 514 nm light used in this study. The *G*'(*2D*) and *D*-bands originate from second-order processes, requiring two iTO phonons to produce the *G*'-band and one iTO phonon plus a defect for the *D*-band. As pointed out by Mallard *et al*. the *G*'-band is often referred to as the *2D*

band because its frequency location is approximately double that of the *D*-band [75]. In this study the *G*' notation will be used because the *2D* label may suggest the band is in some way associated with defects. The *G*'-band has been found to be very sensitive to the number graphene layers, showing significant broadening for bi- and tri-layer graphene. The *D*-band is due to the breathing modes of six-atom rings which require a defect to appear, and has been shown to arise from graphene edges and sub-domain boundaries [73,76]. The *D*-band intensity and FWHM are therefore a qualitative measure of the number of defects present per area of the laser spot size. The *D*'-band may also appear as the result of defects, but at a lower intensity than the *D*-band. The *G**(*D*+ *D*'')-band arises from the same double-phonon resonance process as the *G*' peak, so it may appear without sp^3 defects or edges in the graphene.

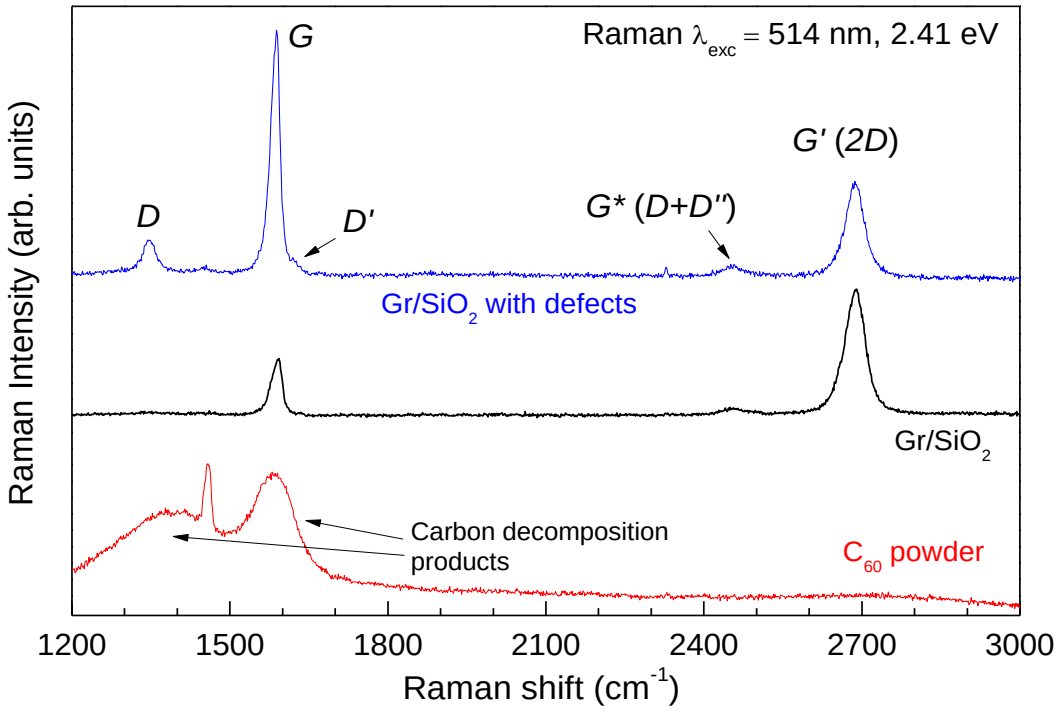

Figure 2.8. Raman Spectrum of Graphene/SiO_2 with defects and without, compared to C_{60} powder with positions of some relevant bands marked. Defects were introduced by deposition of Co of 1 nm thickness on the surface.

Practically, the quality of a graphene sample in terms of number of defects can be quantified by calculating intensity or integrated area ratios of Raman peaks. Ratios are preferred because the absolute intensity of Raman peaks may depend on varying experimental factors such as equipment alignment or spectrometer efficiency. Studies have shown that the peak intensities $I(D)$, $I(D')$ and $I(G')$, depend on the frequency of the exciting laser sources, whereas the integrated peak areas do not [73].

For this reason intensity ratios calculated from experimental measurements in this study were done using integrated peak areas, denoted $A(D)$, $A(G)$ and $A(G')$. The ratios $A(D)/A(G)$ and $A(D)/A(G')$ is a general measure of the defect concentration, typically ranging from 0.1 for very few defects to 4 for highly fragmented or damaged graphene [75]. $A(G')/A(G)$ is used as a general measure of graphene quality as for pristine graphene the G'-band intensity should be at least double the G-band, giving the ratio a value of 3 or higher for nearly defect free graphene [76]. From Figure 2.8, graphene with defects shows this with $I(G')/I(G) \approx 0.5$. In this study Raman spectroscopy was used to characterize the condition of graphene after fabrication steps such as transfer to different substrates or metal deposition.

2.4 Atomic Force Microscopy (AFM)

Another popular technique for the characterization of surfaces is atomic force microscopy. Along with other imaging techniques such STM, transmission electron microscopy (TEM), and scanning TEM using a high-angle annular dark field imaging (HAADF) detector, atomic force microscopy (AFM) is commonly used to examine the surfaces of many materials. Shown schematically in Figure 2.9, AFM functions by sensing the motion of a cantilever attached to a tip

of small diameter (5-20 nm) moving over the surface. In its simplest implementation, the tip is dragged over the sample surface and is deflected by interactions with the sample surface. Depending the particular tip used (insulting, conducting, magnetic) the deflections can measure a number of properties including mechanical contact force, van der Waals forces, capillary forces, chemical bonding, electrostatic forces, or magnetic forces. Other measurement techniques have also been developed involving tapping of the tip as it is moved, accomplished with an embedded piezoelectric element. In tapping mode, the forces on the tip are measured as a change in the oscillation amplitude. This mode is preferred for sensitive samples to reduce damage and can image very thin films or even single molecules. Non-contact mode may also be used where the tip hovers far above the surface to avoid contact in order to measure longer range forces.

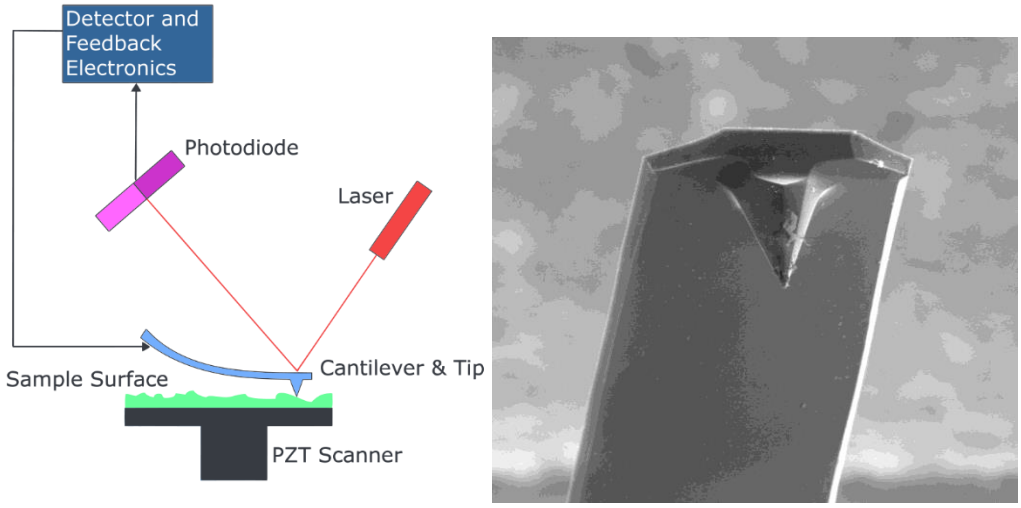

Figure 2.9. Basic AFM operation schematic. The tip is deflection can be measured by piezoelectric elements in the cantilever, or more accurately using laser light reflected off of the polished cantilever surface (Left). A TEM image of a cantilever (width 100 μm) and tip (right). Adapted from Ref. 77.

The tip oscillations in tapping mode may be measured by two methods or a combination. The tip is connected to a cantilever that is highly reflective and attached to a piezoelectric crystal that may act as a strain gauge. This can be used to coarsely measure tip deflections, but is better used in combination with reflected laser light from the cantilever surface. Practically a small diode laser is reflected off of the cantilever surface to land on a photodiode array. This allows for accurate measurement of very small cantilever deflections through the change in reflected laser light. Maps of a sample surface may be produced as changes in the amplitude during tapping mode or simply a surface topography map measuring changes in height. All measurements reported in this study are such surface topography maps.

AFM images in this study were performed in air using a medium range PicoAFM scanner (Molecular Imaging). The images were taken using Si tips available from AppNano with aluminum coated cantilevers and an average tip diameter of < 20 nm. Measurements in this study were done using tapping mode in a frequency range of 90-130 kHz (tip dependent). This equipment was available for use by trained users at the Saskatchewan Structural Sciences Center (SSSC) at the University of Saskatchewan.

2.5 Sample Preparation

2.5.1 Physical Vapor Deposition (PVD)

The method used to deposit cobalt on the graphene surface was physical vapor deposition using a thermal vaporization source in a vacuum environment. PVD is a family of deposition techniques including electron beam evaporation, molecular beam epitaxy, and pulsed laser deposition. In these cases the material reaches the substrate along a line of sight with little or no collision with gas

molecules in the space between the source and substrate. The vacuum environment exists not only to prevent these collisions, but also to limit contamination of the deposited film from gaseous molecules that may be present. Vacuum PVD is typically performed under pressures between 10^{-5} and 10^{-9} torr with deposition rates of 1-100 Å/s. Films formed by this method will have a growth pattern depending on several factors such as substrate surface condition and system geometry, deposition parameters including deposition rate and operating pressure, and post-processing procedures such as annealing.

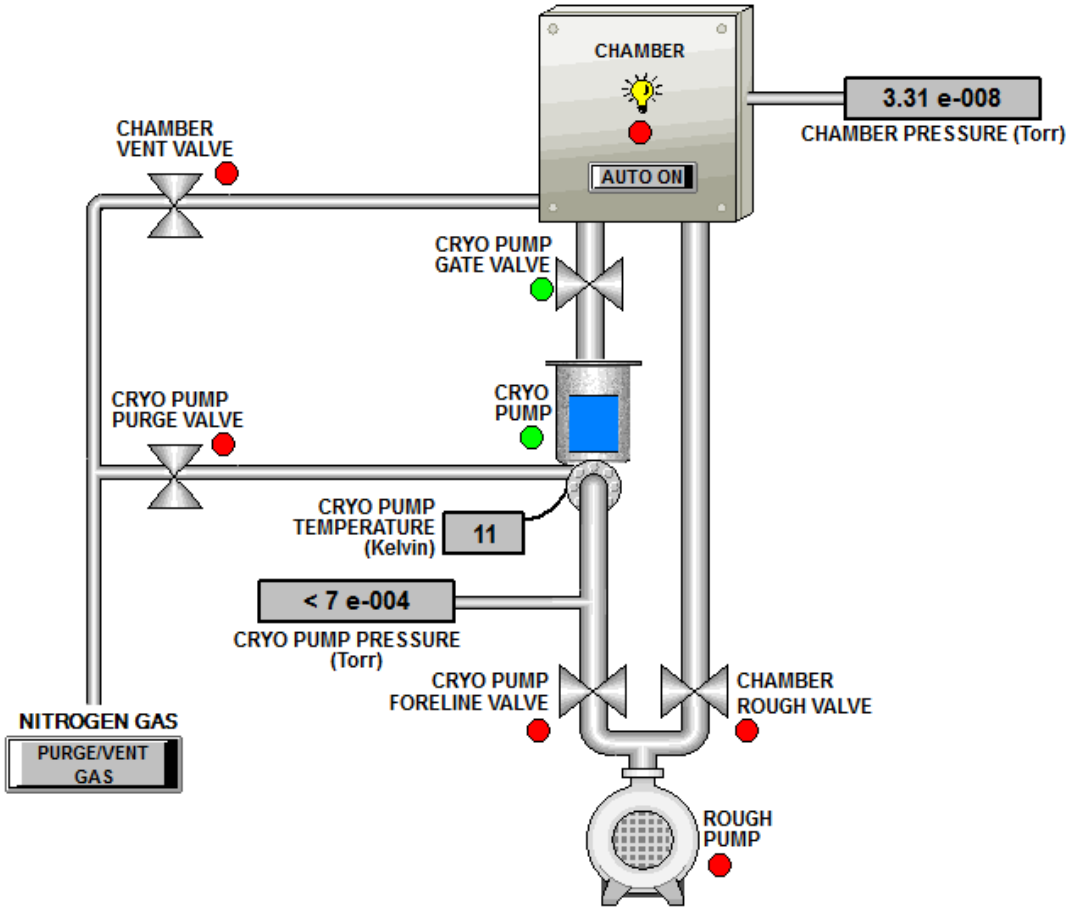

Figure 2.10. Schematic of the Åmod PVD components.

In this study the deposition was performed using an Åmod Physical vapor deposition system available from Angstrom Engineering, with the components shown schematically in Figure 2.10. This system uses two stage pumping system with a backing rough pump and a liquid helium cooled cryopump normally maintained at 10-20 K to obtain high vacuum pressures in the deposition chamber over short time scales of 15-20 minutes when pumping from light vacuum. To vent the chamber under vacuum, inert research grade nitrogen gas is used to raise the pressure such that contamination of the vacuum chamber is limited. This system in particular is very user friendly as all pump down, vent, and other maintenance cycles are pre-programmed and proceed automatically without any required user intervention such as switching pumps on and off.

This system employs 5 different furnace sources: three Radak I tungsten wire furnaces (1 cc), one Radak II (10 cc), and one resistive heater [Figure 2.11(a)]. The Radak furnaces use a coil of tungsten wire to heat a crucible, which is usually made from an insulting ceramic such as alumina (Al_2O_3). Crucibles constructed from this material are structurally stable up to a temperature of 1800 ^oC and are reusable. The resistive heater may be fitted with boats of a variety of shapes and sizes, made of tungsten (W), molybdenum (Mo), or tantalum (Ta). Notably no temperature feedback is available for the resistive heater (embedded sensors are present for the Radak furnaces) so deposition is controlled only by a power percentage applied to the boat. A successful deposition depends strongly on user recipes designed to achieve a given film thickness and deposition rate. The thickness of evaporated material is monitored continuously using quartz crystal thickness monitors, labeled as sensors 1-3. Quartz crystal monitors are commonly used to measure thickness by measuring the change in vibrational frequency of the crystal as material is deposited on its surface. This is possible because quartz exhibits the piezoelectric effect which allows oscillations

to be excited and measured in the crystal electrically. Thus, the deposited film thickness and rate of deposition can be very accurately monitored, down to a resolution of 0.01 Å.

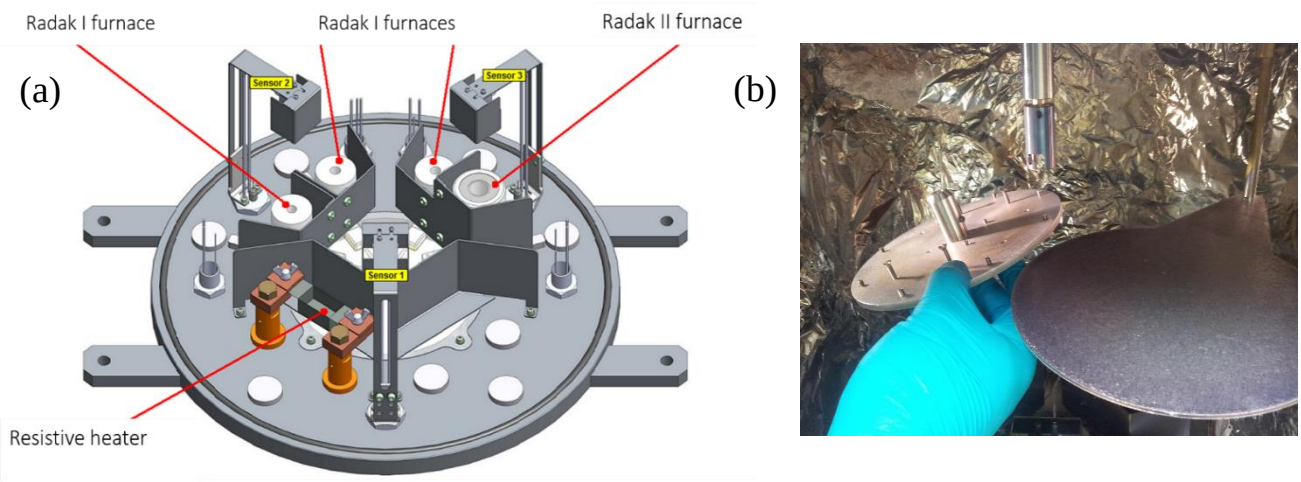

Figure 2.11. PVD furnace schematic and sample plate. (a) Schematic of furnace sources available for PVD. The sensors towers are labeled with sensors 2 and 3 shared between two furnaces. (b) Removing the sample plate from chamber.

A software interface allows for creation of deposition recipes with many variable parameters including material type, film thickness, deposition rate, and ramp/soak times and powers. Depositions are monitored by control software that employs a proportional-integral-derivative (PID) controller to maintain a fixed deposition rate. The procedure begins by preparing a ramp power and soak time where a furnace is ramped to a given power, and maintained at the power for a variable soak time. During the soak time the furnace is under manual (user) control and a shutter between the substrate and furnaces remains closed while the furnace heats. When the furnace heats sufficiently and the desired deposition parameters are reached, the shutter is opened and control of the deposition is turned over to the PID controller which will attempt to maintain a

chosen deposition rate, and will automatically close the shutter when the final desired thickness is reached. In this study PVD was used to deposit cobalt as either a substrate or decorating layer on graphene.

2.5.2 Fabrication of Graphene

Graphene used in this study was fabricated using chemical vapor deposition (CVD) at Sungkyunkwan University, Korea, at the Center for Integrated Nanostructure Physics. CVD is named as such because it uses a mixture of two or more materials at the surface of a substrate to form a new material. This process is usually categorized by the specific parameters used such as the pressure it is performed at, namely atmospheric, low pressure, or in high vacuum. CVD may be aerosol assisted where the precursors are transported to the substrate using a liquid/gas aerosol, or may utilize a plasma to enhance chemical reaction rates of the precursors or deposit at a lower temperature. Many different variations exist for specific applications, but an important detail is that for CVD the films or layers are grown from precursor materials on the substrate surface. Therefore the choice and condition of the substrate as well as the precursor materials is very important for successful deposition. In this study graphene was grown on copper foil of 70 μm thickness. The Cu was first annealed in the CVD chamber for 1 hr at a temperature of 950 °C in an H_2 atmosphere. The graphene single layer was synthesized at 950 °C by using a gas flow of H_2/CH_4, 80/250 sccm, for 20 min, followed by cooling of the chamber down to room temperature in the same atmosphere. Full fabrication details are available in Ref. [78]. The CVD graphene used in this study was fabricated as single layer, and verified using Raman spectroscopy *in situ*.

Graphene/Cu is therefore assumed to by single layer without significant wrinkling or areas of multiple layers when it was prepared.

2.5.3 Preparation of Co/Graphene/SiO_2 samples

As discussed above, preparation of the samples in this study began with graphene grown on copper substrates using CVD. Some graphene was transferred to other substrates such as SiO_2 to decouple it from the copper that it was grown on. This was accomplished using a known solution process, shown schematically in Figure 2.12. First, a polymethylmethacrylate (PMMA):chlorobenzene (Microchem, 95,000 MW) solution was deposited by spin coating on top of as-prepared graphene/Cu samples. The PMMA was dripped onto the sample to cover the entire graphene surface at rest, and spun at a slow acceleration such that 500 rpm was reached over 30 s, and then increased to 1000 rpm for a further 60 s. The PMMA was allowed to dry for several minutes before proceeding. Next the Cu substrate was removed using a ferric chloride copper etchant bath. The PMMA/Graphene/Cu was cleaved with a razor blade to divide the graphene sheet into appropriately sized pieces, then placed in the etchant bath (no heating or stirring was applied). After 45 mins the etchant was visually removed the PMMA/Graphene. The samples were then transferred to a water bath to wash residual etchant away. Transfer to cleaned SiO_2 substrates was accomplished by floating the individual PMMA/graphene pieces onto the SiO_2 surface from the water bath. After transfer, the resulting PMMA/Gr/SiO_2 samples were dried at 80 ^oC on a hot plate for 20 mins to evaporate any water that may be present. Last, the PMMA layer was removed by immersion in an acetone bath for 5 mins. The final resulting graphene/SiO_2 samples were further dried in atmosphere at 80 ^oC for another 20 mins to remove residual solvent.

After the solution transfer procedure, it was assumed that the graphene remained single layer, but may now contain defects and is partially functionalized with sp^3 or sp^2 oxygen functional groups from the solution transfer procedure.

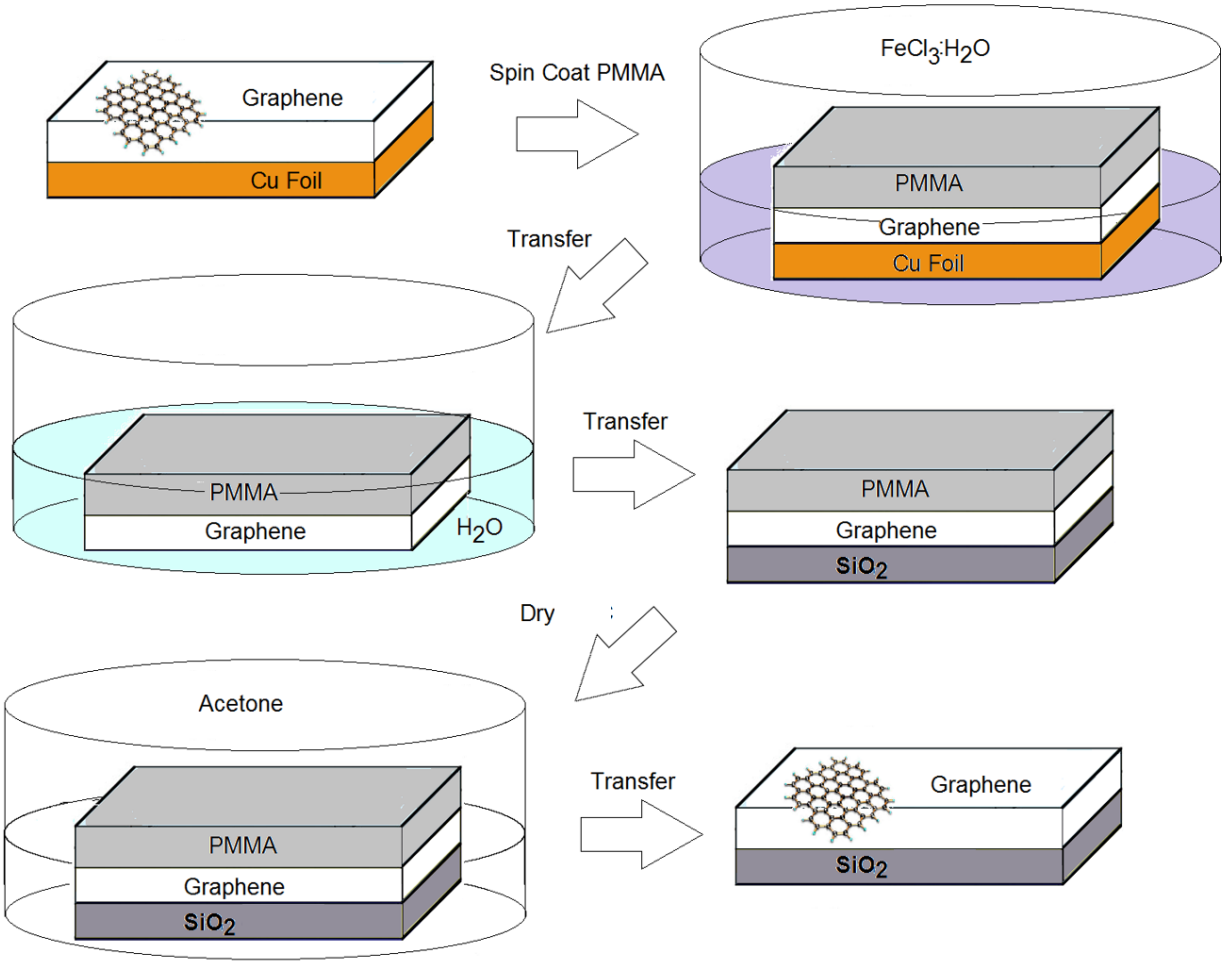

Figure 2.12. Schematic of solution transfer process using PMMA and copper etchant.

Deposition of cobalt on the surface was carried out in the PVD system for each graphene sample. In this study a shallow, wide, tungsten (W) boat in combination with resistive heating was used to deposit cobalt. Co metal powder (99.995% metals basis, Sigma Aldrich) was used as the

source material, with the deposition rate fixed at 0.02 Å/s. The thicknesses examined in this study range from 0.06 nm to 3.0 nm of Co deposited on both graphene/Cu and graphene/SiO_2 substrates. The thicknesses reported are as recorded by the thickness monitor *in situ* and the Co is not considered to be a uniform layer, but rather a submonolayer covering a percentage of the graphene surface. This procedure was also used without modification to transfer graphene to Co/SiO_2 substrates. Notably Co deposition was difficult to achieve at higher deposition rates because under high vacuum conditions Co sublimes rather than melting into a liquid. Additionally at high temperature Co begins to bond with W, forming a brittle Co-W alloy that can cause the boat to form holes or even break apart.

CHAPTER 3

RESULTS AND DISCUSSION

The results and discussion section is organized into two sections focusing on Graphene/Cu and Co/Graphene/SiO_2. The measurements were conducted primarily on four sets of samples to make up these two studies: Graphene/Cu, Co/Graphene/Cu, Graphene/Co/SiO_2, Co/Graphene/SiO_2. The properties of Grapehene/Cu were investigated concurrently with Co/Graphene systems with the aim of understanding the efficacy of graphene as an oxidation barrier for the copper substrate.

3.1 Graphene on Copper

Along with the study of cobalt-graphene systems, graphene/Cu alone was studied to investigate the potential protective properties of graphene in preventing oxidation of the copper substrate. Copper is widely used in many industries including modern electronics due its well-known high thermal and electrical conductivity, as well as environmental availability. However, the formation of an oxide layer on the copper surface even at room temperature results in the creation of trap states and significant degradation of its electrical and thermal properties [79,80]. Therefore a coating that limits or prevents Cu oxidation without disrupting its properties is highly desirable. Graphene could be suitable as an ideal barrier; it is atomically thin, can be easily grown on Cu, and is an excellent thermal and electrical conductor.

There are two possible paths for the penetration of oxygen to the metal surface covered with graphene. The first is intercalation when gas molecules leak between the graphene and metal to interact with the substrate metal. This model explains why the oxidation requires heating during

the intercalation process, but does not account for the dependence of metal corrosion on the quality of the graphene (which should not affect the process of intercalation), or why the corrosion starts from the sample edges instead of its center [81,82]. The other model describes penetration of oxygen through the surface of graphene [81], but according to theory and experiment, graphene impermeable to gases unless defects are present to serve as permeation pathways [83-85]. Recent studies have shown the possibility of formation of vacancies in one, two and three-layer graphene during the process of oxidation, which may result in pathways for oxidation of the Cu [86,87].

To investigate the oxidation of Cu substrates over time, samples of Gr/Cu prepared by CVD were aged in either a low humidity (LH) (dessicator) environment, or in ambient atmosphere at room temperature (ATM) for 1 month to 1.5 years. The graphene in these samples was considered to be a single layer without significant wrinkling or areas of multiple layers. Some native oxygen functional groups may be present on the graphene due to exposure to ambient atmosphere. These samples were investigated using XPS and XAS at the C *K* and Cu $L_{2,3}$ edges with measurements results compared to DFT calculations performed using SIESTA. From the results a model is proposed that takes into account both oxidation of the graphene and penetration of carbon atoms into the Cu during synthesis of the graphene.

3.1.1 XPS spectra of Graphene/Cu

The spectroscopic characterization of graphene/Cu begins with an XPS survey spectra of the elements in the samples. The core level peaks associated with carbon (C *K*) and copper (Cu L_1, Cu $L_{2,3}$, Cu M_1, Cu $M_{2,3}$ and Cu *LMM*) are clearly seen in each survey spectrum. A small amount of oxygen (O *K*) is detected, but does not vary significantly between samples. All samples contain

some native oxides, but it is not immediately clear from the survey whether the graphene or the Cu is oxidized. Oxygen present in graphene/Cu may be simply due to adsorbed water on the graphene surface or oxygen functional groups on the graphene. To investigate graphene-oxygen bonding further, the inset of Figure 3.1 displays high resolution measurements of the C *K*-edge showing a prominent C=C bonding peak that is similar in shape and intensity between the samples.

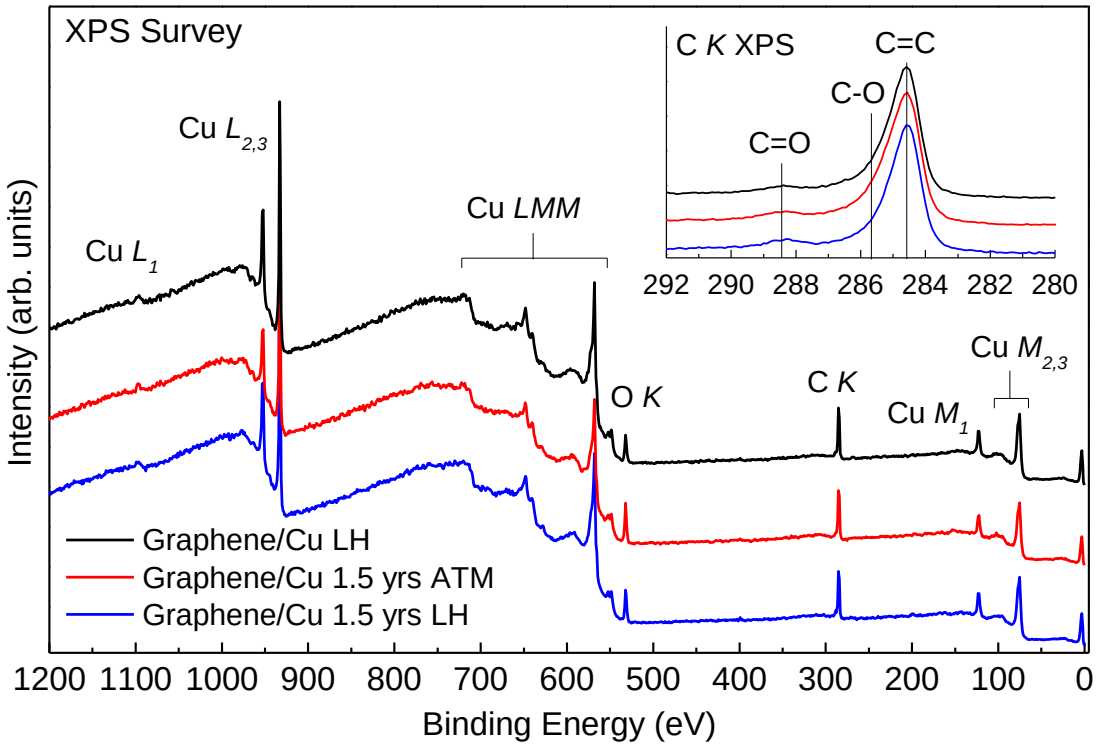

Figure 3.1. XPS survey spectra of Graphene/Cu after oxygen exposure in low humidity and ambient atmosphere environments. The C 1*s* core level XPS spectra are shown in the inset. Graphene is abbreviated to Gr in figure legends.

From the C *K*-edge, evidence of oxygen functional groups appears as a low intensity feature at 288.4 eV corresponding to C=O bonding, and a slight shoulder on the high energy side of the main C=C peak representing C-O bonds. These initial results suggest the graphene overlayer resists

oxidation and subsequently may limit oxygen diffusion into the metal substrate. Even after 1.5 years of exposure the oxidation is comparable to recently prepared samples stored in low humidity. This suggests that the oxidation present in the samples appears immediately after their fabrication, and may be native to the graphene or Cu substrate.

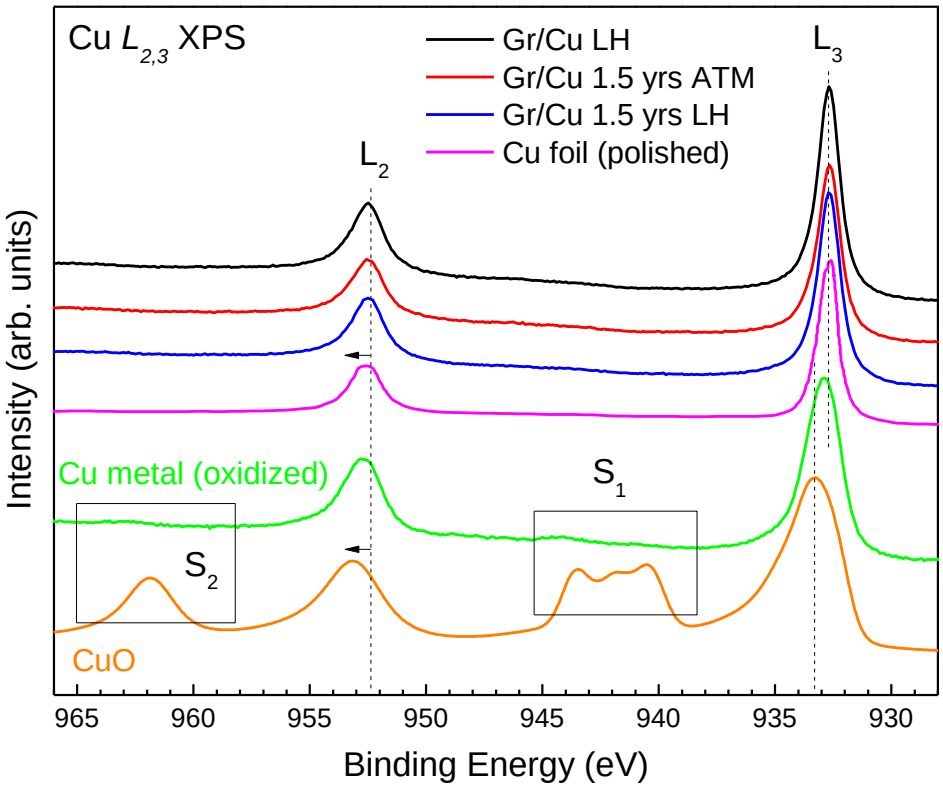

Figure 3.2. Cu $L_{2,3}$ XPS of Graphene/Cu samples compared to copper references.

First to investigate the oxidation of Cu, Figure 3.2 shows the Cu $L_{2,3}$ edge of graphene/Cu compared to copper references. Both graphene/Cu and Cu-foil (polished) have similar spectral shape and energy positions for L_2 and L_3 peaks [88], while the reference spectrum of Cu-metal (oxidized) exhibits a shift to higher energy towards binding energies of CuO [89]. Higher energy fine structures S_1 and S_2, which are in the energy location for charge-transfer satellites typical of

CuO, are small or not visible in Cu foil. This demonstrates that both graphene/Cu and Cu-foil (oxidized or polished) have no Cu^{2+} oxidation state. However, only Cu^{2+} oxidation states may be ruled out here because the Cu $L_{2,3}$ core-level XPS spectrum of Cu metal (polished) is identical to that of Cu_2O [89]. Therefore, the presence of a monovalent (Cu^{+}) oxidation state in graphene/Cu and formation of Cu_2O cannot be excluded without looking further at the valence band spectra.

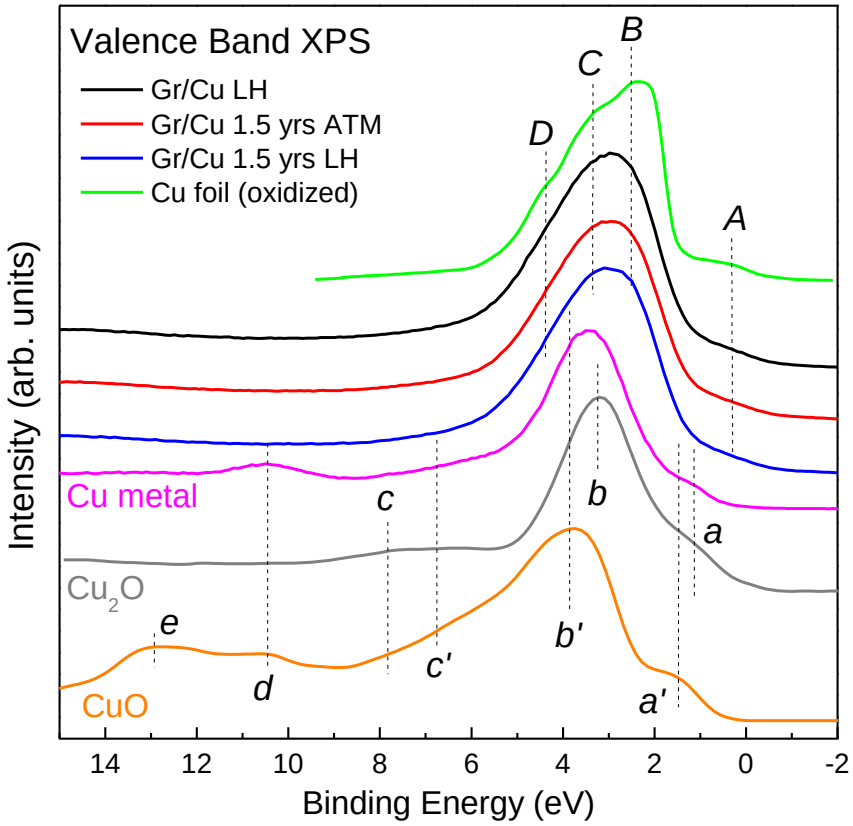

Figure 3.3. XPS valence band spectra of graphene/Cu and reference samples Cu-foil after exposure to ambient air (oxidized), Cu metal (polished), CuO and Cu_2O.

As seen in Figure 3.3, XPS VB spectra show *A*, *B*, *C* and *D* fine structure features typical for Cu metal (polished) which are completely reproduced in spectra of graphene/Cu [90]. Peaks *a* and *b* of Cu-foil (oxidized) appear closer to that of Cu_2O than CuO; that is, no low-energy shift of

spectral features is observed. Additional fine structure features *c*, *d* and *e* also appear, typical for the valence band of CuO [89]. Aside from these peaks, several other higher energy features are visible in Cu_2O and CuO, labeled *c*, *d* and *e* that are not seen in the valence band spectra of any of the graphene/Cu samples. This further indicates that the copper substrate is not oxidized significantly to form either CuO or Cu_2O. From the XPS analysis, it appears the surface of the Cu substrate has not been significantly oxidized. To verify this result and also probe deeper into the Cu substrate, XAS measurements were performed at the C *K* and Cu $L_{2,3}$ edges, which are discussed in the next sections.

3.1.2 C *K* and Cu $L_{2,3}$ XAS

To further examine the electronic structure of graphene/Cu, the unoccupied DOS states of carbon and copper were also probed. At the carbon edge (Figure 3.4) graphene/Cu shows a splitting of the main π* peak of ~ 0.47 eV relative to graphene/SiO_2, with no change in the σ* peak position. This π* splitting suggests a significant change in the graphene/Cu electronic structure which may be attributed to charge transfer, covalent bonding, and/or vacancy formation. Aside from the splitting of the main π* peak, peaks between the π* and σ* features are evident in all graphene/Cu samples, and is highest in the graphene/SiO_2 transferred samples. These peaks represent formation of oxygen functional groups such as C-O-C, C-OH, COOH, and C=O. They may be native to graphene, or present from residual solvent or PMMA from the transfer process in the case of graphene/SiO_2. These spectral features are further discussed in detail in Chapter 3.1.2. Evidence of oxidation is well documented in graphene, and the splitting of the π* peak as

well as peaks in the range of 287-289 eV indicate that the graphene has been partially converted to graphene oxide.

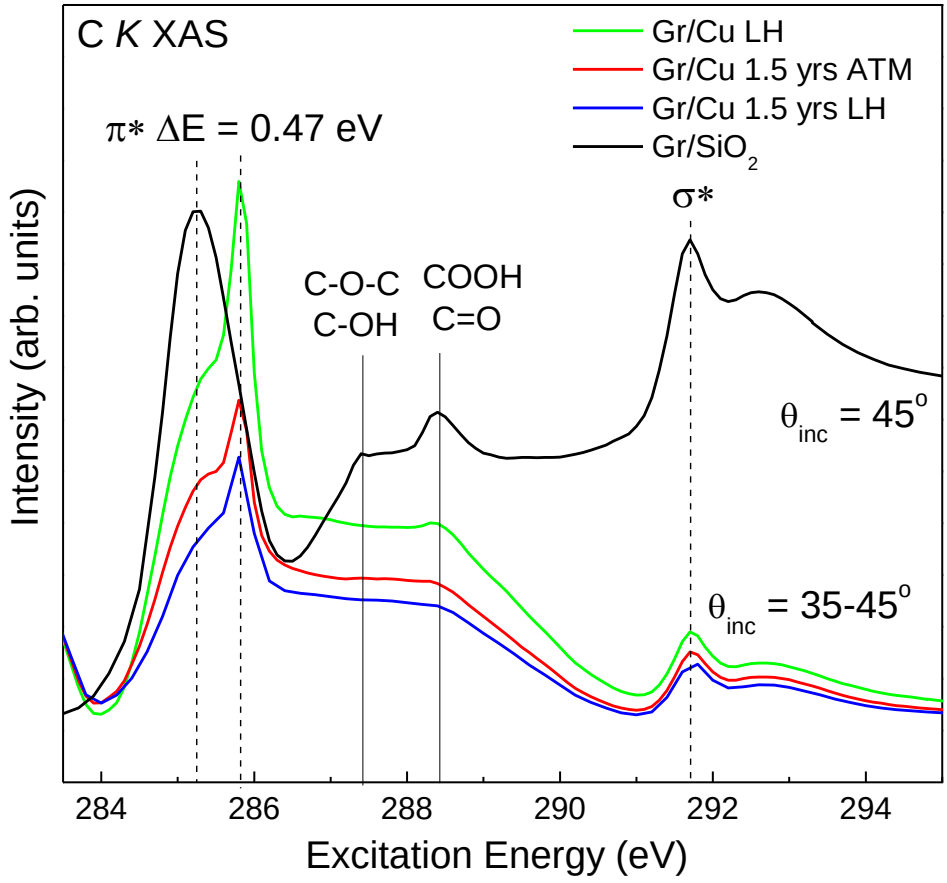

Figure 3.4. C K XAS of Graphene/Cu compared to Graphene/SiO_2. Significant differences in the peaks are evident between the two samples with a splitting of the Graphene/Cu main π* peak.

Notably the background and relative peak intensities between the samples on Cu vs. SiO_2 is significantly different. This results from a background signal for Cu substrates that is not present for SiO_2. Cu has many loosely bound valence electrons that are easily excited at low X-ray energies, resulting in a large signal background. The spectra acquire the skewed shape due to the

sudden onset of absorption at the carbon edge causing a drop in the background signal. Importantly, the energy positions of the peaks are not affected by this background artifact.

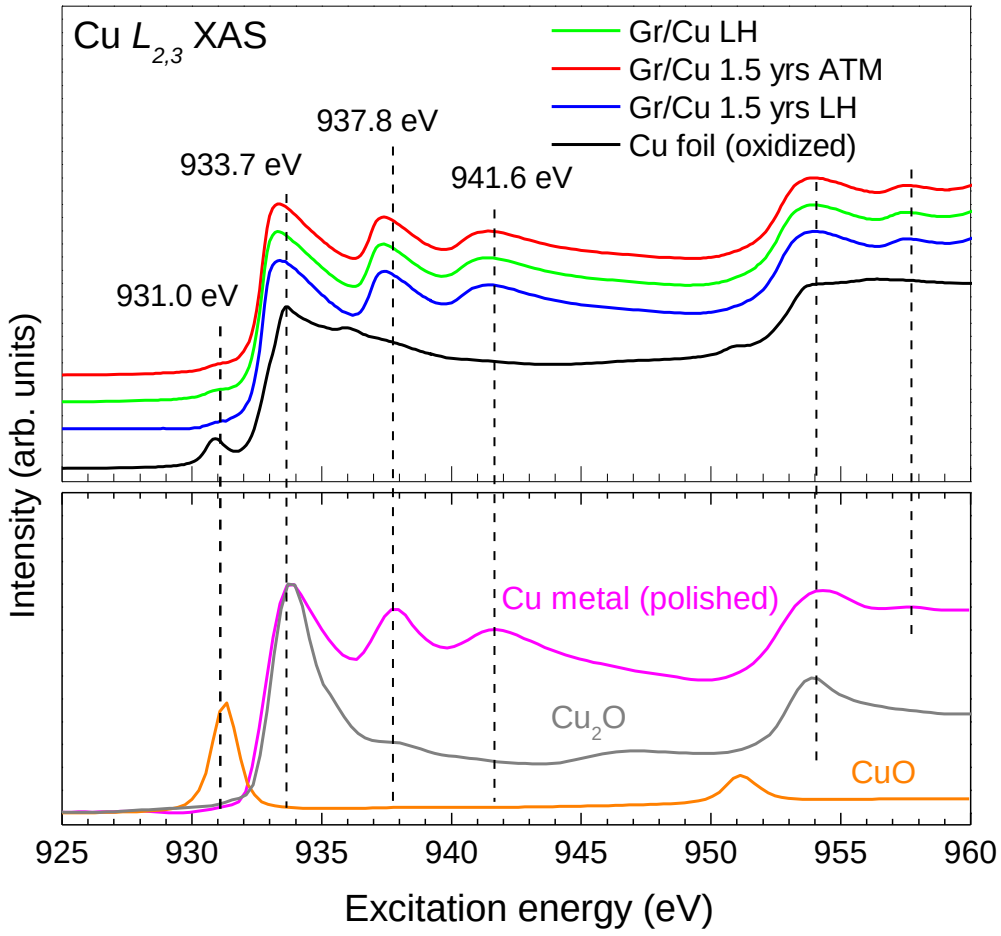

Figure 3.5. Cu $L_{2,3}$ XAS measurements compared to calculated spectra.

The splitting of the main π* peak suggests significant changes to the graphene band structure likely due to oxidation, which is further investigated using density functional theory calculations with the SIESTA calculation code. Before discussing those details, the final spectroscopy measurements were XAS of the Cu $L_{2,3}$ edge, shown in Figure 3.5**.** From comparison to reference samples the Cu $L_{2,3}$ XAS spectra of graphene/Cu is very similar to that of Cu-metal in energy

position of the peaks as well as fine structure, and quite different from Cu_2O and CuO [91]. Spectral features at 937.8 eV and 941.6 eV for polished Cu metal are reproduced in graphene/Cu samples, while those features are suppressed in Cu oxides. The spectra of Cu foil (oxidized) is found to be in good agreement with Cu_2O containing races of CuO as indicated by the peak at 931.0 eV, in agreement with XPS results. From these measurements it is clear that the Cu substrates are not significantly oxidized, even after 1.5 years of exposure. The graphene itself has been oxidized into graphene oxide containing oxygen functional groups, but the contamination does not affect the underlying Cu substrate. This shows that graphene in as-grown condition is a robust barrier for oxidation under normal atmospheric conditions, even when the graphene itself becomes oxidized. The remaining detail is the origin of the peak splitting observed in C *K* XAS, which was further analyzed using SIESTA calculations.

3.1.3 SIESTA Simulations of C *K* XAS

The DFT pseudo-potential code SIESTA was used to simulate the carbon DOS for four different Graphene/Cu systems containing different arrangements of carbon and copper. With these simulations, the origin of the π^* peak splitting in C *K* XAS can be determined. The arrangements simulated were a pristine free standing graphene sheet, graphene with defects on copper, graphene on copper with carbon interstitials, and graphene with epoxide impurities and carbon interstitials [Figure 3.6(a-d), respectively]. Calculations were performed using the local density approximation (LDA) exchange-correlation functional with a full optimization of the atomic positions as well as optimization of the force and total energy with an accuracy of 0.04 eV/Å and 1 meV, respectively. Double-ζ plus polarization basis sets were used to represent the localized

orbitals for carbon and oxygen sites. All calculations were carried out with an energy mesh cut-off of 360 Ry and a k-point mesh of 4×4×2 in the Monkhorst-Park scheme [92]. The calculated density of C 2*p* unoccupied states for free standing graphene is shown in Figure 3.6(a). It is in a reasonable agreement with experimental splitting between π* and σ* peaks (7 eV) in the C *K* XAS spectrum of graphene/SiO_2.

However, the 0.47 eV splitting in the main π* peak is not seen in typical graphene/Cu samples, and may be caused by vacancy formation or bonding between the graphene and Cu substrate [93-95]. In order to determine the origin of the splitting, both bi-vacancies and oxide contamination of the graphene are considered. A bi-vacancy is a fairly stable configuration with a vacancy size that allows oxygen atoms to penetrate through the graphene to the copper beneath. The presence of this type of defect also results in the formation of covalent bonds between the carbon atoms at the edges of the vacancies and the copper substrate. These covalent bonds lead to appearance of an additional σ' peak and high energy shift in the π*-peak of 1.3 eV as shown in Figure 3.6(b), which is not observed in C *K* XAS. However, Figure 3.6(d) does reproduce the π*-peak splitting (~0.7 eV) in the case where oxygen atoms form epoxide groups (C-O-C), combined with carbon impurities in the Cu matrix below. This theoretically predicted DOS agrees with the XAS spectra showing a π*-peak splitting as well as other peaks indicating oxidation.

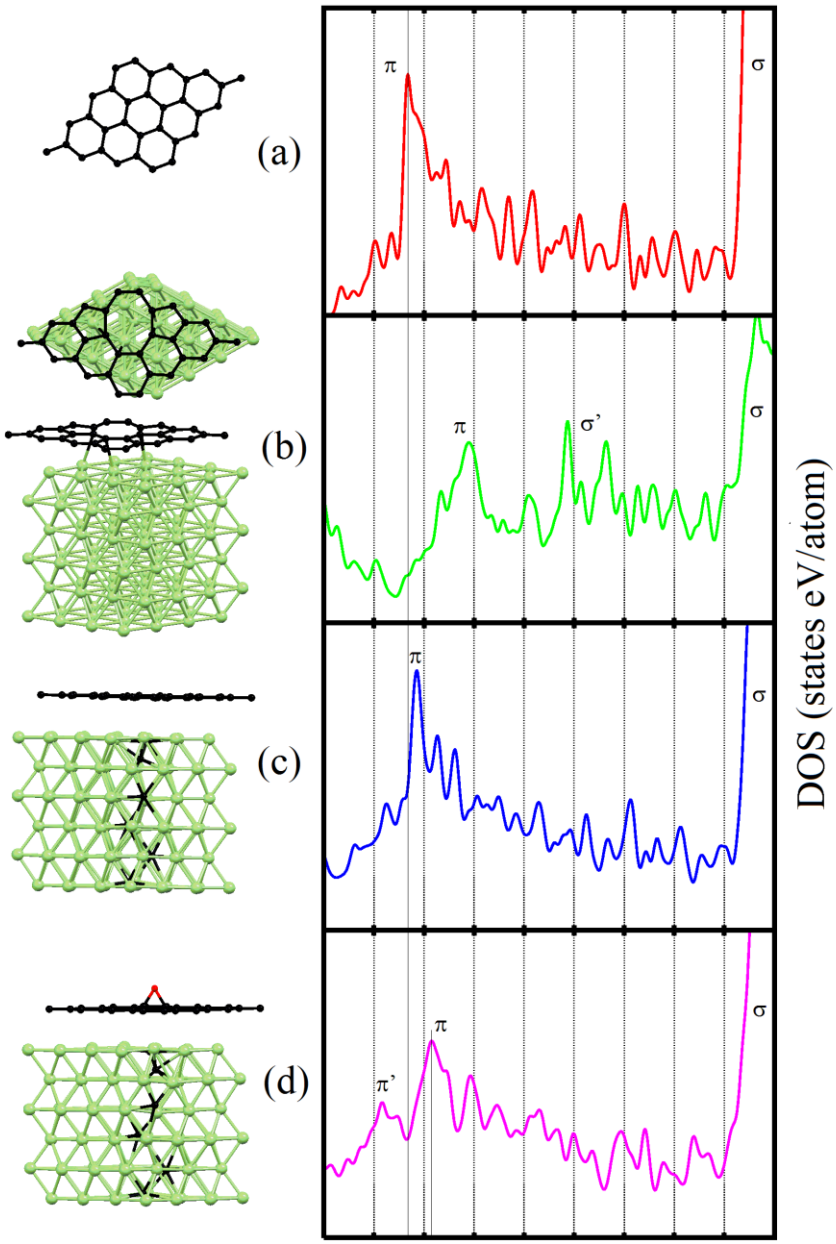

Figure 3.6. SIESTA simulations of the carbon DOS for four different Graphene/Cu systems. Panel (d) containing epoxide functional groups and carbon interstitials reproduces the peak splitting observed in C K XAS.

Based on comparison of experimental C *K* XAS spectra with unoccupied C 2*p* DOS calculated by DFT, we can exclude the formation of carbon vacancies over time which could cause oxidation of the Cu. It is more likely that the splitting of π*-peak results from sparse epoxide formation on the graphene surface combined with interstitial C impurity atoms. This is reasonable when considering that the graphene was grown on the Cu which could produce interstitials, and that the Cu foil was very thin (70 μm). The low thickness of the foil resulted in practical considerations where it was nearly impossible not to bend or twist the samples as they were mounted for measurements. In this case, unavoidable bending of the samples could produce defects in the graphene that promote epoxide formation. In an attempt to limit bending, some Graphene/Cu was mounted on rigid SiO_2 substrates using carbon tape, but the results were not significantly different.

These results show that graphene can be a robust barrier to oxidation of an underlying Cu substrate due to atmospheric exposure over long time scales. The graphene itself may also be converted to graphene oxide without affecting its veracity as an oxidation barrier.

3.2 Co/Graphene/Cu

3.2.1 XPS Survey and Valence band spectra of Graphene/Cu

Concurrent with the study of Graphene/Cu, work was also begun concerning cobalt deposition on graphene samples. Full survey scans of all element edges were completed for Graphene/Cu samples both with and without Co. A representative set of these measurements is shown in Figure 3.7, identifying the expected elements in the sample by the energy location of their edge. As Co is added, peaks become evident (circled) as well as an increase in the O *K*-edge intensity. Similar to

the Graphene/Cu survey scans, a closer look is required at selected edges to identify the functional groups forming.

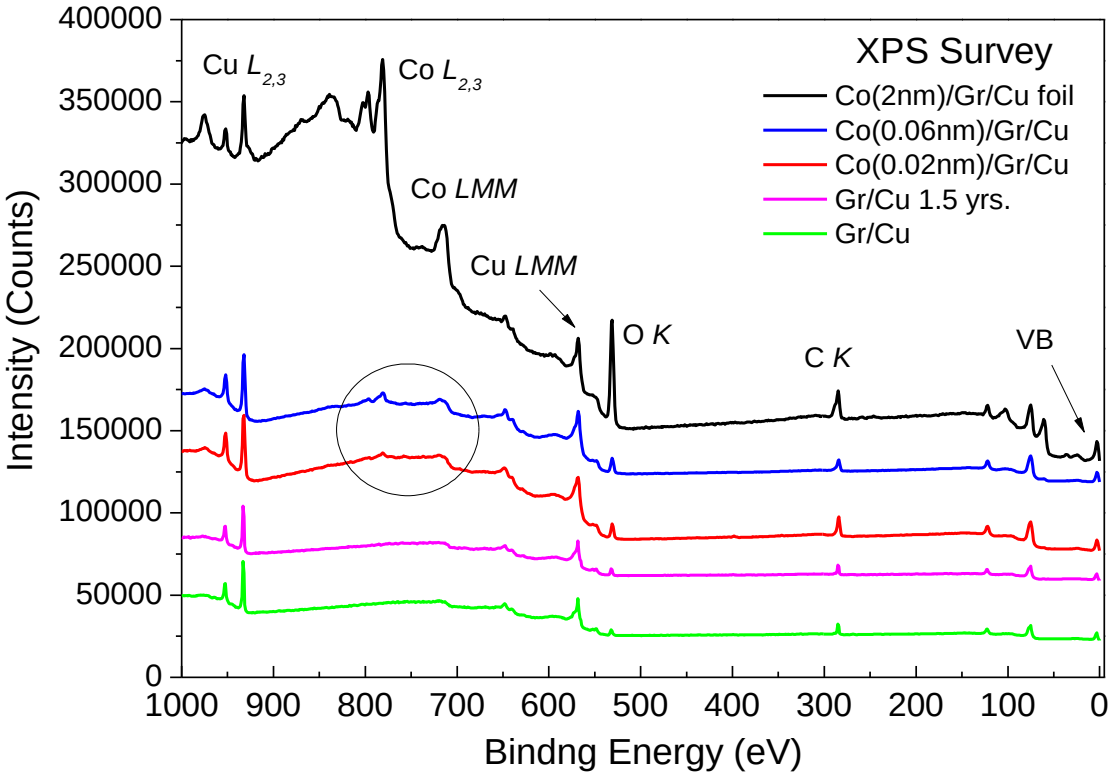

Figure 3.7. XPS survey scans of graphene/Cu and Co/graphene/Cu samples. Very little change in the spectra is evident for graphene aged as long as 1.5 yrs.

Peak fitting using Voigt functions at the C and O *K*-edges was performed to identify functional groups that form with Co deposition (Figure 3.8). Peak fitting was performed by considering the possible functional groups and their energy locations as reported in the literature for graphene oxide systems [96]. C=O and C-O bonds are formed and increase with Co thickness, as well as carbonate (CO_3^{-2}). Some oxide groups (C=O, C-O) are present in low concentration even on as-prepared graphene/Cu, which may be due to native oxidation or adsorbed water. It should be noted

here that in the O *K* XPS, there may be a contribution from cobalt oxides in peaks in the range of 529-533 eV, but they could not be resolved using peak fitting [97].

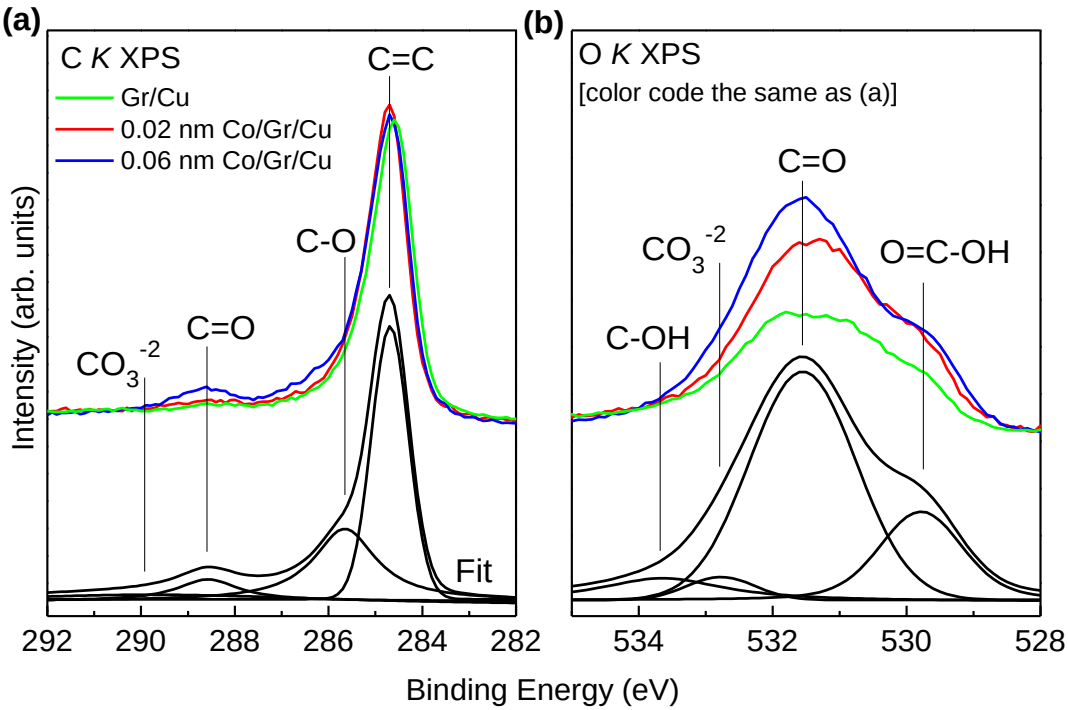

Figure 3.8. XPS scans of (a) carbon edge and (b) oxygen edge. Oxygen functional groups form in proportion to the deposited Cop thickness.

The concentration of oxides continues to increase with the thickness of Co deposited, and can therefore can be manipulated by finely controlling the deposition rate and final thickness. Various thicknesses of Co were deposited (up to 2 nm, Appendix A: Figure A.1) with a clear trend of increasing oxide concentration proportional to Co thickness. Spectra of the valence band were also recorded for Graphene/Cu and Co/Graphene/Cu samples (Figure 3.9). Comparing VB measurements to reference spectra of Co shows CoO and Co clusters when 2 nm of Co is deposited. At lower thicknesses (below 0.06 nm), pre-edge features at 0-2 eV are not present, but the main peak is clearly split into two (2.6 and 3.5 eV) when any Co is present compared to the smooth

single peak of Graphene/Cu. As cobalt is deposited, Co and CoO contribute additional electronic states to the valence band that cause the peak splitting (peak at 3.5 eV in CoO).

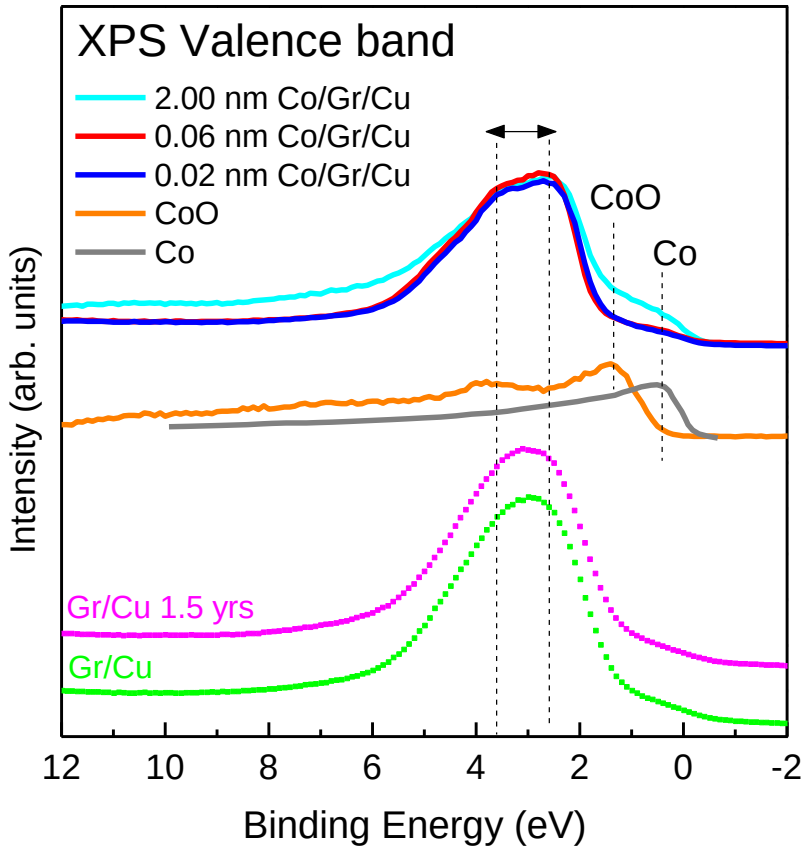

Figure 3.9. Valence Band spectra of Graphene/Cu and Co/Graphene/Cu samples. After 2 nm of Co deposition, CoO and some Co metal are evident.

3.2.2 Raman Spectroscopy of Graphene/Cu

To characterize the condition of graphene/Cu, Raman measurements were also performed as detailed in Figure 3.10. From visual comparison to Figure 2.8, there is clearly a large background signal present. This is caused by low energy fluorescence from the Cu substrate excited by the laser light. Unfortunately fluorescence excitations are much more probable than Raman scattering

events, so the background signal makes analysis difficult by nearly overwhelming the *G* and *G'* bands. For this reason, characterization using Raman spectroscopy was focused on Graphene/SiO_2 samples that do not contain such a large substrate-induced fluorescence background.

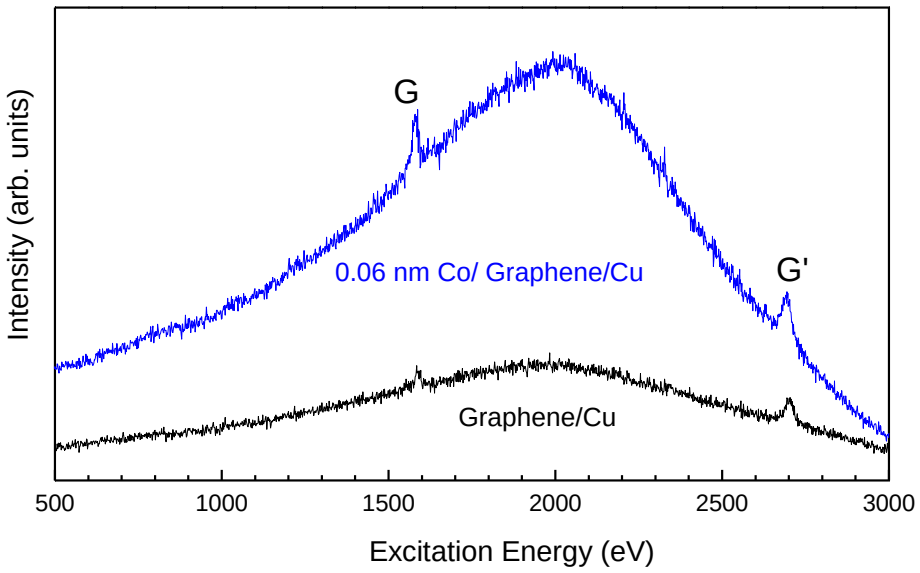

Figure 3.10. Raman spectra of Graphene/Cu and Co/Graphene/Cu.

After completion of XPS and Raman measurements of Graphene/Cu samples, two facts became clear. First, the development of CoO on the surface is directly related to the motivation of producing RKKY exchange coupling in graphene. CoO is antiferromagnetic, and therefore if clusters are centered and *A* and *B* sublattices, it fulfills the requirements suggested in Ref. 42 to achieve band opening. Second, the effect of the Cu substrate on the graphene DOS cannot be discounted. In addition to the troublesome Raman background signal, any shifting of the graphene Fermi level due to unknown charge doping from the substrate could be prevented by decoupling the graphene and moving it to a non-interacting surface. With these points in mind, further experiments were performed after transfer to SiO_2 substrates.

3.3 Co/Graphene/Co/SiO_2

3.3.1 Motivation

With the motivation of RKKY coupling in mind, the next experimental architecture investigated was a stack of Co/graphene/Co where the bottom Co layer was varied between 1 and 10 nm. These thicknesses were chosen to manipulate the surface magnetization direction of the Co. At 10 the Co is effectively bulk with a parallel surface magnetization. Below approximately 3 nm the layer is thin enough for the direction to be perpendicular to the surface, represented by the 1 nm thickness. At the outset of this study, it was unclear which magnetization direction would be more favorable. This architecture allows for two exchange processes to occur; first between the cobalt under layer and decorating Co clusters to induce a fixed magnetization direction in the clusters.

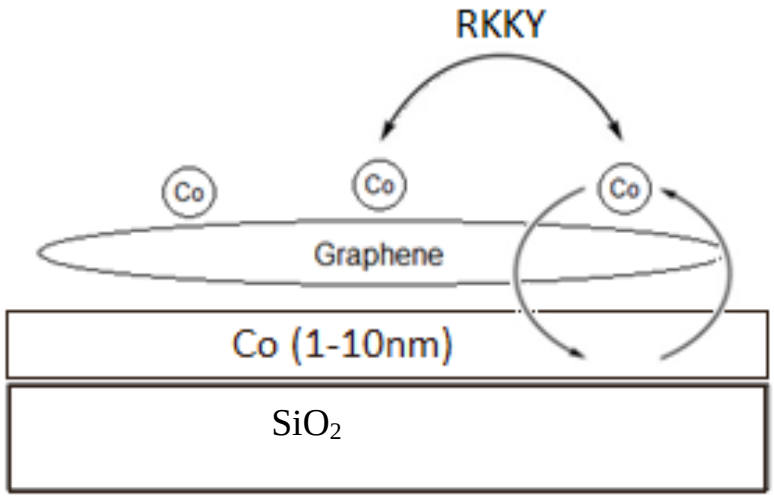

Figure 3.11. Schematic representation of Co-Graphene trilayer stack. Double or super exchange coupling as well as RKKY coupling combine to spin polarize graphene electronic states.

Second, RKKY coupling between the clusters may in turn spin polarize the graphene conduction electrons. This may have the two fold effect of allowing this architecture to potentially open a semiconducting band gap in graphene as well as serve in spintronic devices. With this motivation in mind, samples were fabricated as described in the Experimental Chapter with varied bottom layer thickness (1-10 nm) and between 0.06-0.12 nm to top Co thickness.

3.3.2 C *K* XAS and XES

XAS measurements of a set of cobalt-graphene samples is detailed in Figure 3.12 below. The intensity variation between some of the measurements is due to a slightly different angle of incidence of linearly polarized X-rays. Since Graphene is nearly planar to the substrate surface, the X-ray polarization results in preferential excitation to π^* or σ^* states at grazing (90^o) and normal (0^o) incidence, respectively (See inset). Aside from the main graphene π^* and σ^* peaks at 285 and 292 eV, respectively, new peaks are visible between the two. Peaks at 287.4 eV (*A*) and 288.3 eV (*B*) may be due to the presence of hydroxyl (C-OH) or epoxide (C-O-C), and carbonyl (C=O) or carboxyl (COOH) functional groups, some of which may be remnant from the transfer process [96,97]. It is possible that peak *A* does not arise from bonding to functional groups alone, but also from carbon sites that have been perturbed by nearby functional groups [98]. This detail is important as bonding of epoxide groups (which are in the energy position of peak *A*) could act to break up the graphene over time. This is supported by the observation that peak *A* does not vary in intensity significantly after the addition of Co. Peak *B* similarly does not show significant intensity variation between the samples. Peak *C* at 290.2 eV is attributed to a carbonate (CO_3^{-2}) structure which is verified by comparison to $CoCO_3$ (Alfa Aesar 99.95 %) reference powder. There

is significant change in intensity of the carbonate peak, particularly when Co is deposited on the graphene when a Co substrate is present.

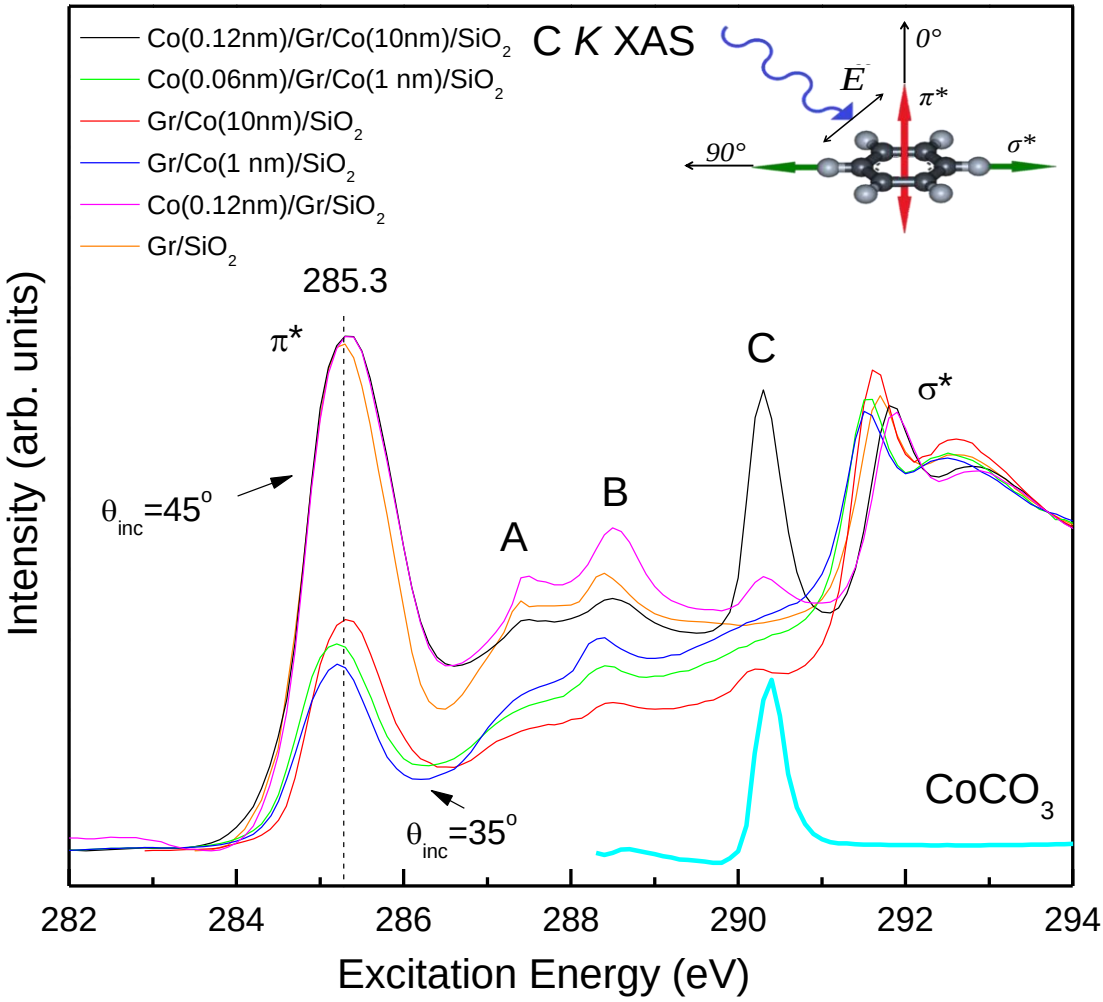

Figure 3.12. XAS of Co-Graphene samples. Peaks *A*, *B*, *C* are evident representing oxygen bonded to the graphene when Co is added to the system.

This is reasonable since Co may bond easily at defect sites as it is slowly deposited on the surface to produce carbonates. The largest intensity of this peak appears for a Co(10 nm) substrate with Co(0.12nm) deposited on the surface. From these measurements the carbonate concentration is directly related to the amount of Co; carbonates do not form until a threshold thickness on

deposited Co is reached at approximately 0.10-0.12 nm. The position of the main π* peak of Graphene/SiO_2 is marked with the dotted line. There appears to be some shifts of the main π* peak relative to Graphene/SiO_2 which may indicate a band gap opening, and are examined more closely in Figure 3.13(a).

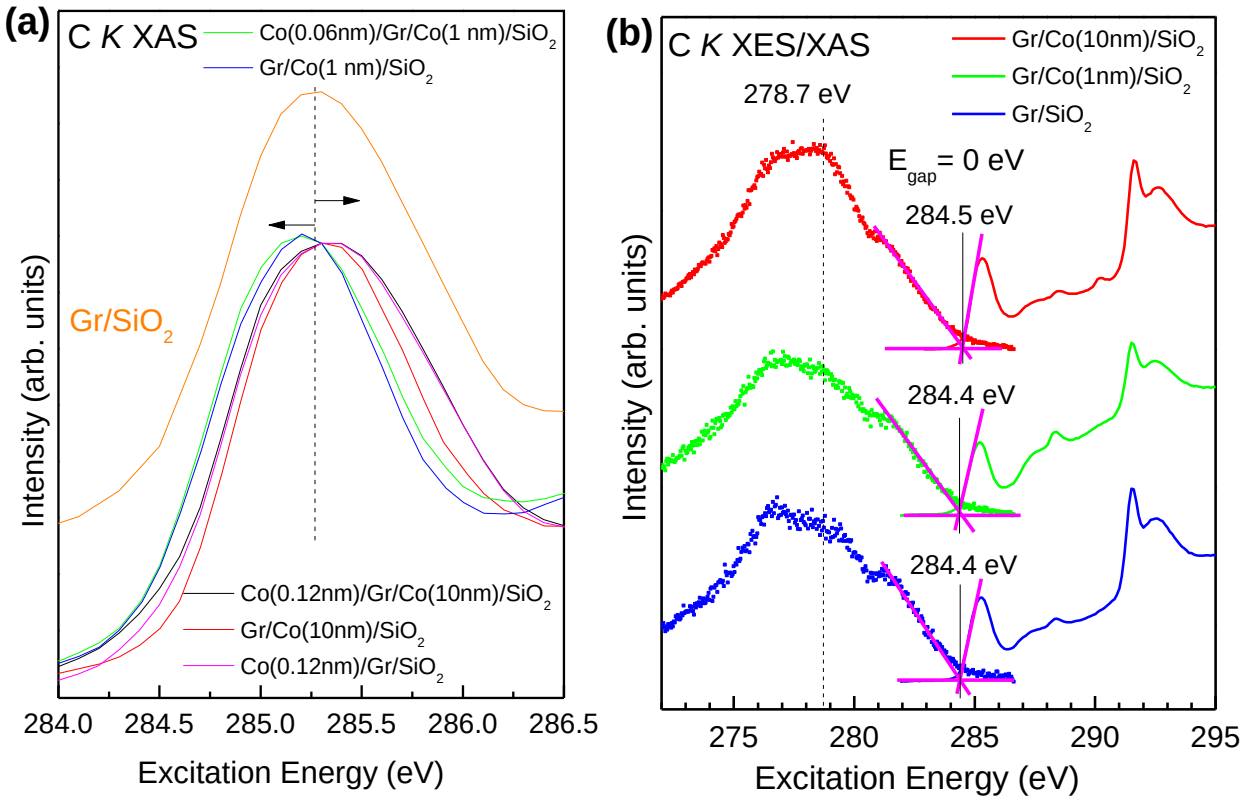

Figure 3.13. XAS and band gap analysis for Co substrates. (a) The main π* peak of Co/Gr samples. Some band bending and a shift of unoccupied states to higher energy of about 0.05 eV is observed for three of the samples containing relatively high amounts of Co. (b) Band gap determination for a Co substrate compared to Gr/SiO_2.

Notably the relative shift of π* and σ*peaks in the same spectrum does not appear to be constant. For example in the case Co(0.06nm)/Gr/Co(10nm), the π* peak is shifted -0.15 eV relative to Graphene/SiO_2, while the σ*peak shift is -0.32 eV. This difference may indicate different hybridization between the Co 3*d* states with the out-of plane *p*-orbitals compared to the in-plane *s*-orbitals.

XES measurements were also performed (Figure 3.13 (b)), primarily to probe the edge of occupied states to determine if a band gap is present. A shift in the unoccupied states alone may arise from a shift of the Fermi level due to charge carrier doping, so a full picture of the graphene 2*p* states is required. In a non-resonant XES experiment of carbon, the resulting spectra often does not contain many sharp spectral features because carbon 2*p* occupied sates are very degenerate in energy. Without a resonant excitation to promote a specific transition over others, the resulting spectra are very broad. Nevertheless some spectral change is evident by the intensity increase of peak at 278.7 eV representing an increase in the DOS due to Co-C bonding.

The existence of a band gap in graphene/Co/SiO_2 samples was determined using line fitting to the edge of 2*p* unoccupied and occupied states, and extrapolating to the baseline to determine the conduction-band-minimum (ECBM) and valence-band-maximum (EVBM), respectively (Figure 3.13(b)) [99]. Line fitting was found to be preferred for band gap determinations in graphene as opposed to using 2nd derivatives to locate fluctuations in the spectral line. This is because the XES spectra are dependent on collecting sufficient counts to have a well-defined edge above the noise threshold. For graphene, gathering sufficient counts to meet this condition confidently was very difficult, making interpretation of the band gap using the 2nd derivative inappropriate (see Appendix B). The fitting with XES measurements for graphene transferred to a Co substrate shows for both the 1 nm and 10 nm thickness a closed band gap is evident. This indicates that the shift

observed in XAS is due to charge doping of the graphene from the Co substrate, and does not alone open a band gap. Similar results were observed (Appendix A: Figure A.3) when Co was added to the surface to create the sandwich structure shown in Figure 3.11 indicating that the charge doping effect from Co is too great for any band gap opening to arise from magnetic exchange coupling when a Co substrate is used. At this point the focus of the study shifted to Co/Graphene/SiO_2 which from Figure 3.13 shows an energy shift to higher energy in the unoccupied states.

3.4 Co/Graphene/SiO_2 Electronic Structure

Before completing the discussion of the band gap in Co/Graphene probed with X-ray spectroscopy, the surface characterization using Raman and AFM will be discussed. In the course of the actual study, Raman and AFM were performed before the X-ray band gap characterization. Several thicknesses of Co were deposited on graphene ranging from 0.02 – 3 nm, but the discussion will focus on the most interesting set ranging from 0.06-0.25 nm where favorable modification of the band structure was observed.

3.4.1 Raman Spectroscopy

Raman measurements were performed to primarily determine the condition of the graphene after transfer to SiO_2 substrates and Co deposition. Both of these processes may damage the graphene through wrinkling or etching of the surface. After the transfer, large areas of the graphene remain intact with clearly defined *G* and *G'* (*2D*) bands. Below 0.25 nm thickness of Co, the spectra appear very similar to undeposited graphene/SiO_2 while a red shift is observed in both *G* and *G'* bands at 0.25 nm of Co. This small red shift of 3.8 - 6 cm^{-1} in the *G'* and *G*-bands

respectively can be attributed to charge transfer from the Co to the graphene, or a strain reduction [100-102]. Strain could be induced in the graphene due to transfer to the SiO_2, which is then reduced by Co deposition. Strain reduction may occur at higher Co thickness where the metal begins to etch and break up the graphene into smaller pieces, reducing the overall strain. At 0.12 nm of Co thickness, broadening of the *G*-band is visible that develops into a shoulder peak at 1531 cm^{-1} for 0.25 nm Co. The similar *G*-band broadening has been reported for Cr-deposited on graphene, and in semiconducting single-walled carbon nanotubes (S-SWNT) [103]. In S-SWNTs this band has a Lorentzian lineshape and arises from vibrations in carbon atoms along the circumferential direction of the tube. Since only a suppressed *D*-band is visible, a high level of graphene curvature similar to a CNT is unlikely. In this case this feature arises from a removal of degeneracy in the *G*-band stretching mode due to Co deposition. This feature is resonantly enhanced in intensity due to additional electrons transferred from the Co, causing an increase in electron-phonon interaction. The ratio of integrated peak intensity, *A(G')/A(G)*, is calculated to be ~ 4 or greater for all cases (Table 2), showing the graphene is indeed a single layer and has not become folded or heavily wrinkled from the transfer process. In addition, very low *A(D)/A(G)* ratio (below 0.1) indicates nearly defect-free graphene. At thicknesses above 0.25 nm, the number of defects on the surface increases and the Raman lineshape begins to resemble the blue curve in Figure 2.8 for 1 nm of Co deposited.

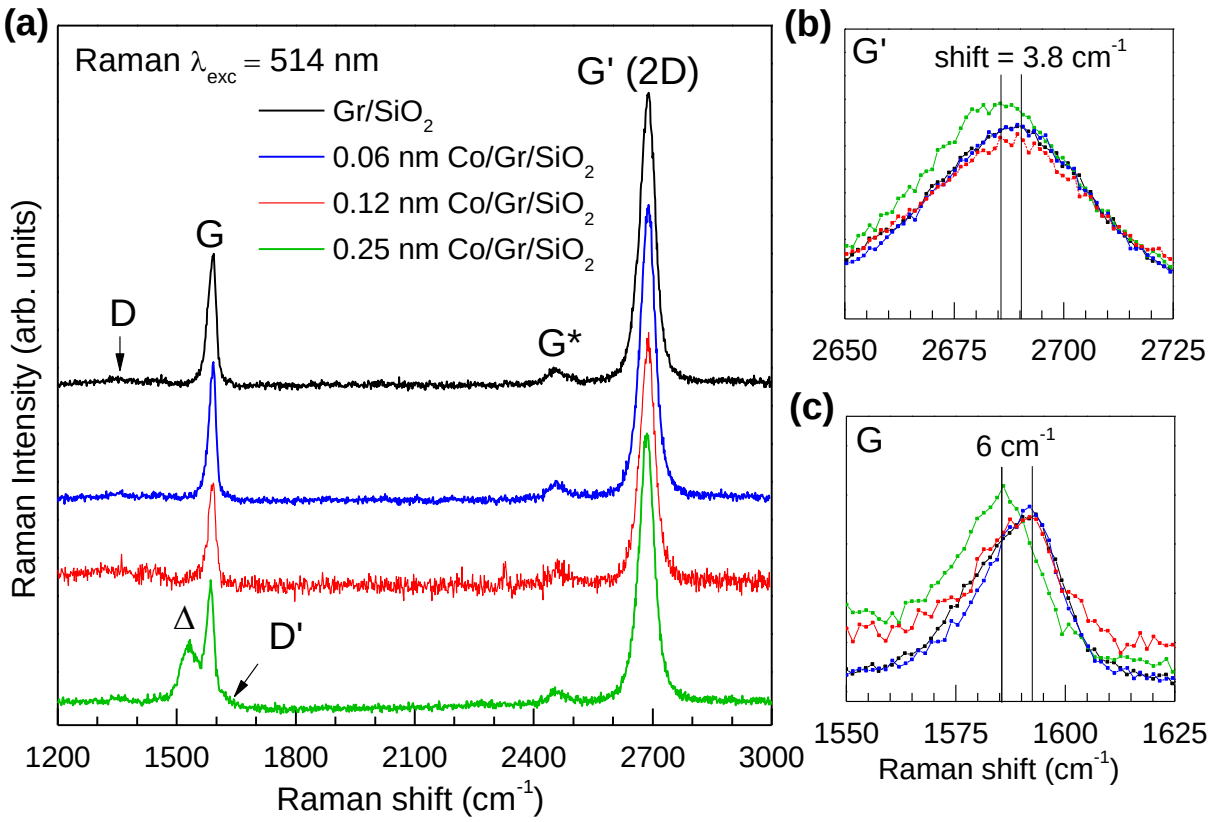

Figure 3.14. (a) Raman Spectroscopy of Co/Graphene/SiO_2 samples showing the region of interest with *G* and *G'* peaks. After 0.25 nm of Co deposited, and shift to lower wavenumber in both G (b) and G' (c) peaks is observed due to charge transfer from Co to graphene.

	Peak locations (cm^{-1})						**Integrated Peak Area ratios**		
Sample	*D*	Δ	*G*	*D'*	*G**	*G'*	**A(*D*)/ A(*G'*)**	**A(*D*)/ A(*G*)**	**A(*G'*)/ A(*G*)**
Gr/SiO_2	1353	*NA*	1593	*NA*	2455	2689	**0.00325**	**0.0138**	**4.26**
Co 0.06 nm	1353	*NA*	1593	*NA*	2458	2689	**0.00108**	**0.0479**	**4.44**
Co 0.12 nm	1353	*NA*	1589	*NA*	2459	2688	**0.0628**	**0.2504**	**3.98**
Co 0.25 nm	1353	1531	1586	1634	2458	2686	**0.0109**	**0.0724**	**6.71**

Table 3.1. Raman band locations and integrated peak area ratios.

The good condition of the graphene for low metal thickness is notable because Co and other transition metals can produce vacancy-related defects in graphene. The use of metal atoms to etch or cleave graphene in a controlled way is a well-known procedure using many metals including Ni, Cr, Pd, Al, or Ti in conjunction with oxidation or hydrogenation at elevated temperatures [104]. Although we did not anneal the samples, Boukhvalov *et al*. have predicted that metal adatoms (Fe, Co, Ni, or Al) lower the vacancy formation energy in free-standing graphene without assistance from heat [105]. In particular, Co is shown to have the lowest energy for vacancy and bi-vacancy formation compared to other metals when deposited on graphene. However, the vacancy formation in that study was simulated for unsupported pristine graphene, which is not our case. To understand the metal behavior, consider several experimental studies using atomic resolution topography images showing that regardless of the fabrication method used, the graphene surface contains randomly distributed adsorbed hydrocarbon groups [105,106]. Studies on such systems examining metal cluster growth with high resolution transmission electron microscope (HR-TEM) report metal adatoms deposited on the surface prefer to aggregate at defect or hydrocarbon sites, rather than the pristine honeycomb graphene surface [105]. Therefore covalent bonding between graphene and metal adatoms may be limited at low thickness, reducing vacancy formation. This is in agreement with the Raman measurements showing a very low *D*-band for 0.06-0.25 nm of Co.

3.4.2 Atomic Force Microscopy

To gain further insight into the Co distribution on the sample surface, AFM measurements were conducted of several Co/Graphene samples. Figure 3.15 shows a representative topography

measurement of Gr/SiO_2 with a measured height profiles. The graphene appears to be quite rough but note that the contrast is adjusted such that the highest and lowest points are brightest and darkest respectively, even if they only differ by 1 nm. This is reflected by the height profiles where even across the defects the root mean square roughness (RMSR) value is < 2 nm. In the area scanned, some larger contaminates such as residual PMMA are evident from the solution transfer process. Studies have shown that some residue is unavoidable when PMMA is used as a sacrificial scaffold material [107].

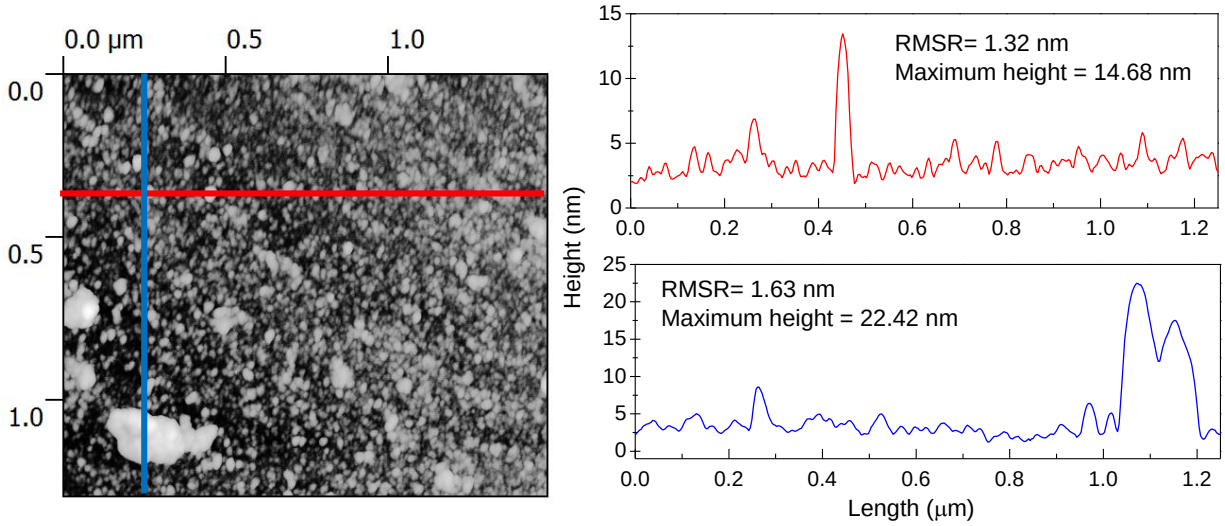

Figure 3.15. 1.2 x 1.2 µm AFM scan of a Graphene/SiO_2 surface. Height profiles are shown for *x* and *y* directions with RMSR values < 2 nm.

Cobalt was deposited using PVD and similarly imaged, shown in Figure 3.16. In the figures the red lines mark the 2D slice that was used for the roughness profiles in Figure 3.17. The Co exhibits Volmer-Weber growth on the graphene surface where islands are formed at nucleation sites preferentially without homogeneous growth across the surface. The two other growth modes are Frank–van der Merwe where layers form uniformly, one at a time, and Stranski–Krastanov where

both islands and layers are formed depending on a critical layer thickness determined by the chemical and physical properties of the material.

At 0.06 nm Co (as measured by crystal thickness monitors), the clusters are small in diameter and aggregate in local areas of 2-3 μm^2. Some areas (4-5 μm^2) were observed that appeared free of Co, showing the coverage is non-homogeneous when this thin. At 0.12 nm thickness, the clusters become substantially larger in diameter but are spaced further apart, and still do not homogeneously cover the graphene surface. This growth pattern suggest nucleation at defect or impurity sites, which would limit the damage to the graphene. This may explain why the graphene appears not to be heavily damaged according to Raman. At 0.25 nm, the Co covers the surface more uniformly, presenting as many smaller clusters spaced closely together and beginning to achieve homogeneous coverage. As Co is deposited, charge transfer makes the graphene's surface more energetically favorable for uniform wetting, resulting in the more homogeneous coverage.

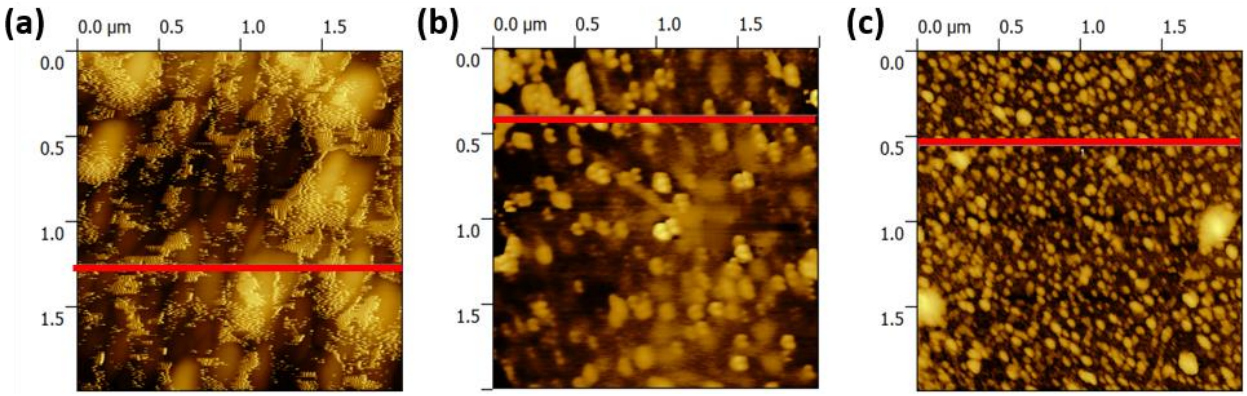

Figure 3.16. 2 x 2 µm AFM images. (a) Co(0.06 nm)/Gr/SiO_2, (b) Co(0.12 nm)/Gr/SiO_2, and (c) Co(0.25 nm)/Gr/SiO_2. Red lines correspond to Figure 3.17 height profiles.

The homogeneity is reflected in the root-mean-square roughness showing the lowest value across all samples for 0.25 nm. Note that some local wrinkling of the graphene in evident in the

roughness profile shown in Figure 3.17 where red lines are used to mark the boundary between the graphene and Co clusters.

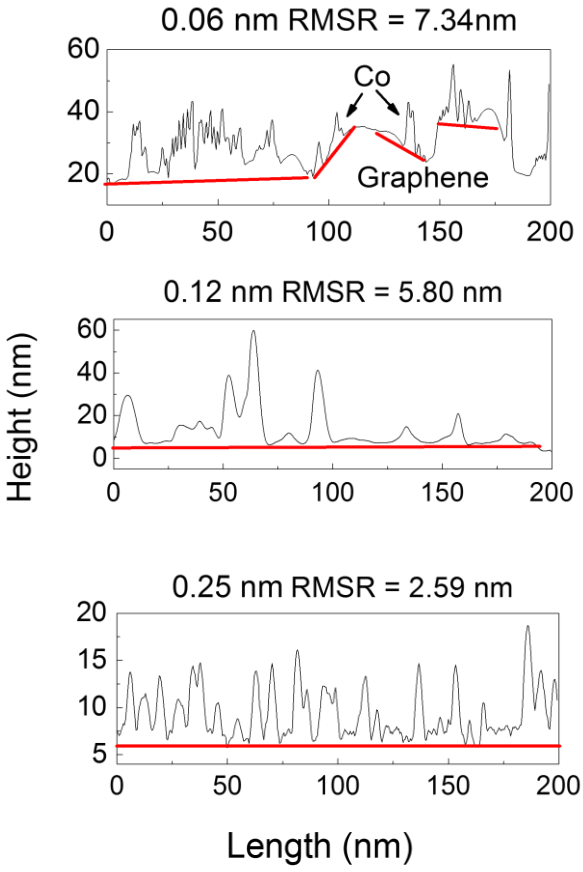

Figure 3.17. AFM Height profiles and RMSR for three different Co thicknesses deposited on Graphene corresponding to Figure 3.16 (a,b,c) as (top, middle, bottom), respectively.

Following AFM and Raman characterization, it seemed that thicknesses below 0.25 nm would be most promising for band engineering of graphene. Co thickness below this level is sufficient to cover the surface but is not a complete monolayer. X-ray characterization of the C *K* and Co $L_{2,3}$ edges was used next to determine if a band gap is formed, and if so by what mechanism.

3.4.3 C *K* XAS and XES

X-ray absorption of graphene with four representative Co thicknesses deposited on its surface is shown in Figure 3.18. The same peaks are observed as discussed for the case of Co substrate, with some important differences. In the case of a Co substrate, peak *B* (C=O and COOH functional groups) was relatively constant and did not vary with substrate thickness, but by contrast there is a clear trend for Co deposited on the surface when compared to Graphene/SiO_2. After 0.25 nm of Co, peak *B* overcomes the main π* peak in intensity.

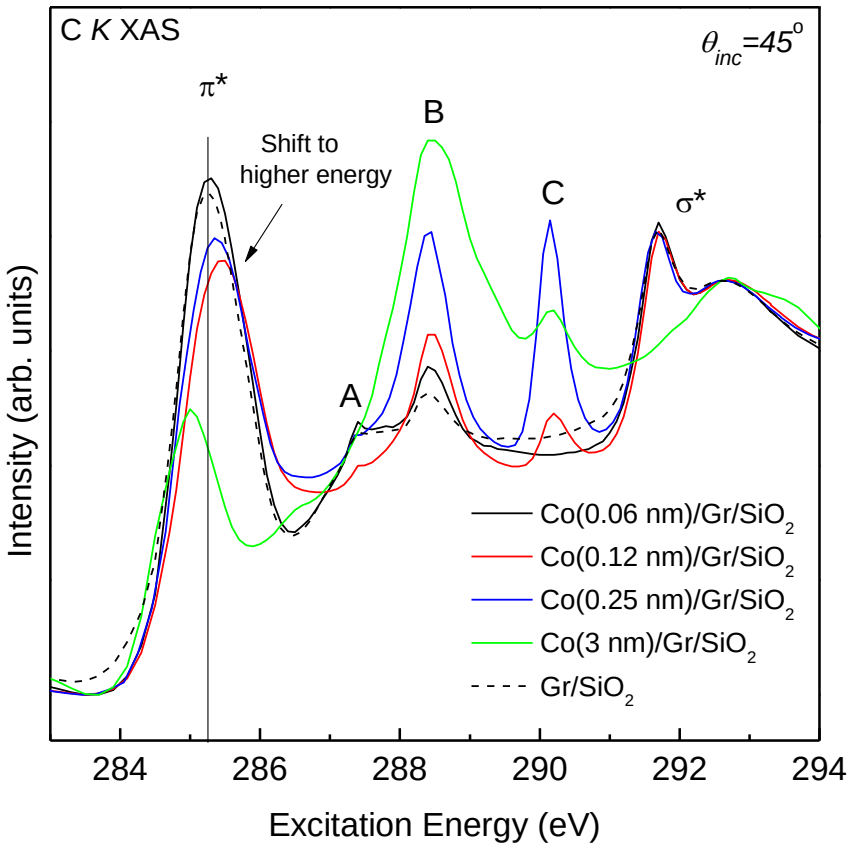

Figure 3.18. XAS of Co/Graphene/SiO_2. Peaks *B* and *C* evolve and increase in intensity as Co is deposited.

A drastic case of Co (3nm) is shown where the graphene electronic structure has significantly changed, indicating damage – the sharp excitonic feature in the lineshape of the σ* peak is no longer visible, and the main π* peak is shifted to lower energy. Peak *C* arises from $CoCO_3$ formation, with a concentration that increases dramatically between 0.12 and 0.25 nm of Co. Aside from the development of oxide functional groups, a band bending and shift to higher energy is evident in the main π* peak for 0.12-0.25 nm of Co.

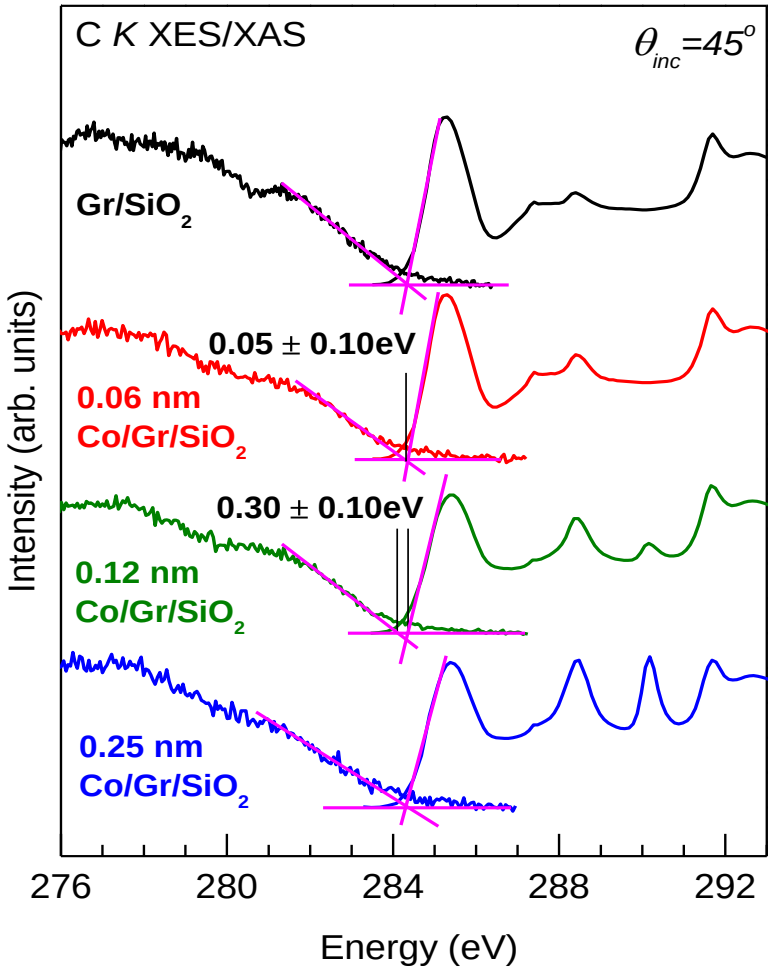

Figure 3.19. Band gap determination for Co/Graphene/SiO_2 samples. Using linear line fitting, a band gap up to 0.30 ± 0.10 eV is evident in graphene 2*p* states with 0.12 nm of Co.

To determine the band gap XES measurements were performed and plotted with XAS for linear line fitting. The energy splitting between unoccupied and occupied states was determined for Co/Graphene/SiO_2 samples as shown in Figure 3.19, with a band gap of 0.05-0.30 ± 0.10 eV evident for 0.06-0.12 nm of Co. The uncertainty in the measurement arises mainly from the energy uncertainty due to the calibration procedure. An error in energy of 0.05 eV from both XES and XAS measurements is reasonable to account for the energy width of spectral features in the samples used for calibration. It should be noted here that although there is a relatively large uncertainty in the band gap value, the shift of the edge of occupied and unoccupied states between measurements with different Co coverage is clearly evident. Apart from a shift of the edge of occupied states, there is very little variation in XES measurements across the sample set. Based on these measurements, conditions to support a band gap can be defined where the intensity of peak *B* representing C=O and C-O bonding in the graphene is large compared to peak *C*, representing carbonate ($CoCO_3$).

After the discovery of a measureable band gap in Co/Graphene, the question of the mechanism remained. A full picture of the graphene 2*p* states has been provided by C *K* XAS/XES, showing the band opening. To determine the mechanism the Co $L_{2,3}$ edge should also be probed. XAS measurements of this edge are detailed in the next section. Due to the dilute nature of Co some of the samples, XES measurements were not possible in all cases (Appendix A: Figure A.2).

3.4.4 Co $L_{2,3}$ XAS and MLFT Simulations

XAS measurements at the Co $L_{2,3}$ edge were used to probe the characteristics of Co deposited on the graphene surface. The Co was classified using comparison to reference samples and multi

ligand field theory simulations. Measurements of Co/graphene samples are detailed in Figure 3.20 below (L_3 edge only). Two peak positions are labeled, A^* (776.2 eV) representing the onset of Co unoccupied states, and B^* (779.4 eV), a characteristic peak of Co^{+3} in Co_3O_4. One must take care when interpreting the energy position of the edge; due to spin-orbit interaction the core hole in the final state has a significant effect on the spectrum. At first glance, Co/graphene/SiO_2 samples show sharper multiplet features associated with metal-oxides when compared to a 10 nm metallic reference Co film. Metallic films without oxygen have broader XAS features due to the lack of oxygen bonding to break the state degeneracy.

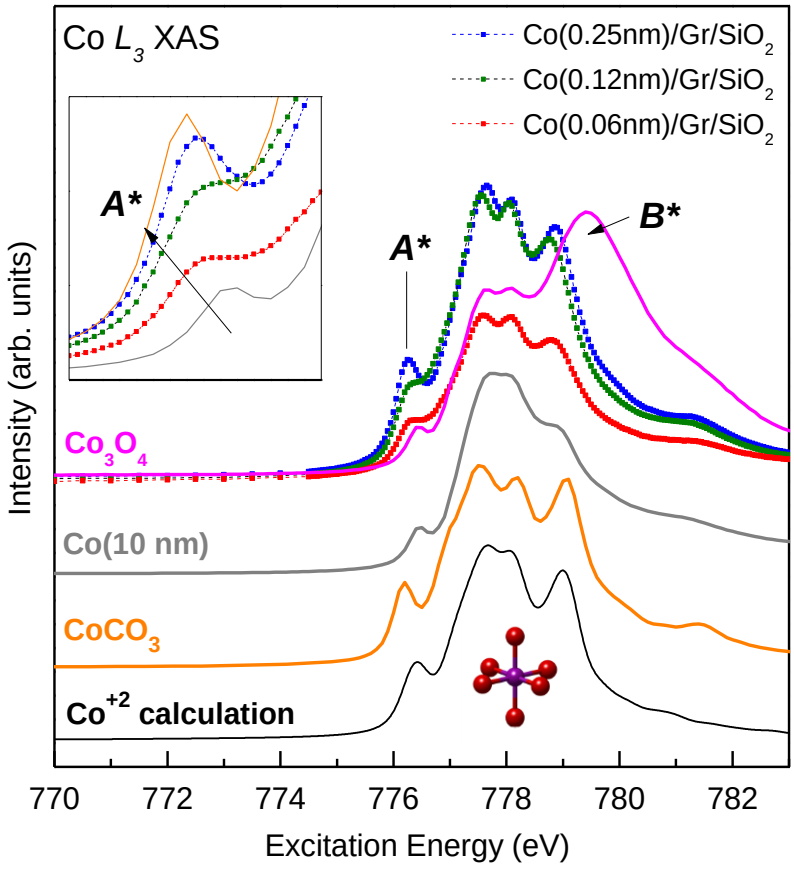

Figure 3.20. Co L_3 XAS of Co/Graphene/SiO_2 compared Co_3O_4 reference and a simulated spectrum for CoO in octahedral symmetry.

The lack of peak *B** in Co/Graphene also qualitatively shows that little to no Co^{3+} is present. Shown enlarged in the inset of Figure 3.20, peak *A** shifts to lower energy by 0.15 eV. From comparison to a $CoCO_3$ reference, the shift arises as more $CoCO_3$ is generated as opposed to only CoO. Peak *A** is a convolution of signals from both $CoCO_3$ and CoO with $CoCO_3$ lower in energy. This can be seen by the lineshape of $CoCO_3$ that well matches Co(0.25 nm)/Graphene to produce the shift in *A**.

As discussed in Chapter 2, MLFT simulations were used to interpret Co $L_{2,3}$ XAS spectra of Co/Graphene/SiO_2 samples. The simulation was fit to the spectrum for Co (0.25 nm), resulting in Co^{2+} with octahedral symmetry. The slater integral scaling was 86 %, with the other calculation parameters reported in Table 3. The positive 10*Dq* value, which represents the energy difference between the t_{2g} and e_g *d*-orbitals, indicates an octahedral geometry (*Oh* point group), consistent with CoO. However, to obtain good agreement with the experimental spectrum, a small Dσ was included. This suggests that the structure is not strictly octahedral, but rather a distorted octahedral. This can be interpreted as compression or stretching along one of the crystal axis, possibly due to interaction with the graphene/SiO_2 substrate. The calculations indicate that Co in octahedral symmetry (CoO) is the dominate phase, but other Co^{2+} phases in other symmetries such as cobalt hydroxide ($Co[OH]_2$ *P*3*m*1 space group) could also be present.

10*Dq*	*Dσ*	*Dτ*	*Δ*	*U - Q*	V_{b1g}	V_{a1g}	V_{b2g}	V_{eg}
0.4	-0.1	0.0	3.5	0.5	2.0	2.0	0.85	1.0

Table 3.2. MLFT CoO calculation parameters (eV)

From the Co measurements it is clear that a band gap opening is accompanied by the formation of not only oxygen functional groups but also CoO and $CoCO_3$. However from the measurements presented, a band gap is observed when the concentration of carbonates is low compared to CoO and other oxygen functional groups. This is possibly because formation of a carbonate requires a site at a vacancy, defect or edge, meaning that carbonates initially formed are anchored at defect sites natively present on undeposited graphene. This is supported by the Raman measurements which do not show evidence of graphene etching after metal deposition until thickness above 0.25 nm is reached. From Figure 3.19, the only significant changes to the C *K* XAS spectral shape between 0.12 nm and 0.25 nm are intensity increases in peaks *B* and *C*. This suggests that $CoCO_3$ contributes to closing a band gap that is induced by other factors such as oxidation of the graphene. To further investigate this system, electronic structure calculations were performed to investigate oxide formation versus metallic Co cluster formation on graphene. Metallic Co clusters were initially simulated concurrently with the performance of experimental measurements. After Co $L_{2,3}$ XAS was observed, calculations focused on the effect of CoO because a band gap was observed in the Co/Graphene sample where CoO is the primary cobalt compound.

3.5 Theoretical Simulations using Density Functional Theory

Calculations of the graphene band structure were undertaken using WIEN2k for several sample environments including cobalt metal clusters (Figure 3.21) and CoO (Figure 3.22) on graphene. The results were spin polarized in both cases and take spin-orbit coupling into account with the specific details of each calculation discussed below.

3.5.1 Cobalt Metal Clusters on Graphene

Metallic clusters were the first structure simulation that was attempted. DFT simulations of three different Co/graphene structures were performed using WIEN2k with the calculation parameters as follows. Single layer graphene sheets were used that were isolated from each other by 10 Å vacuum. This isolation is necessary because WIEN2K performs the calculation on an infinite lattice of repeating graphene unit cells. In order for the cells above and below to be non-interacting, a vacuum layer of 10-20 Å is required. Cobalt was added to the system by placing 1, 4, or 7 Co atoms on a 4 x 4 supercell of graphene, to achieve C:Co ratios of 32, 8, and 4.57, respectively. The positions of all Co and C atoms were allowed to relax until all forces were below 1 mRy/a.u., showing that Co does not significantly perturb the graphene lattice even for 7 atom clusters. For all three structures, the LDA exchange-correlation functional was used. The C states were simulated using a linear augmented plane wave (LAPW) basis set, whereas the Co states used an augmented plane wave plus local orbital (APW+lo) basis set, so as to better simulate the Co 3*d* states [68]. A gamma-point centered mesh of 10 x 10 x 1 points was sampled in k-space where the number of k-points calculated depended upon the symmetry of the cell. The plane wave expansion was taken up to a RK_max of 7.0, with charge, force, and energy convergence criteria set to 0.001 e, 0.5 mRy/a.u., and 0.0001 Ry, respectively. Muffin tin radii for C and Co sites were 1.32 Bohr and 1.40 Bohr, respectively. The muffin tin radii are not strictly required to be of a certain size; the radii defines where the atomic-like basis set is switched for the planewave basis set. Setting a reasonable value may increase the speed of the calculation, but so long as it is large enough to contain the wavefunction it will not affect the calculated DOS.

In all cases of metallic Co that were simulated, a band gap is not evident in either spin channel. This is because Co metal adds additional conduction electrons to the graphene conduction electron sea. This causes overlapping of the graphene valence and conduction bands, with the effect becoming more pronounced for larger clusters. From these results it is clear that metallic Co increases the density of states at the edge of the valence band. Therefore, metallic Co clusters alone cannot open a band gap in graphene.

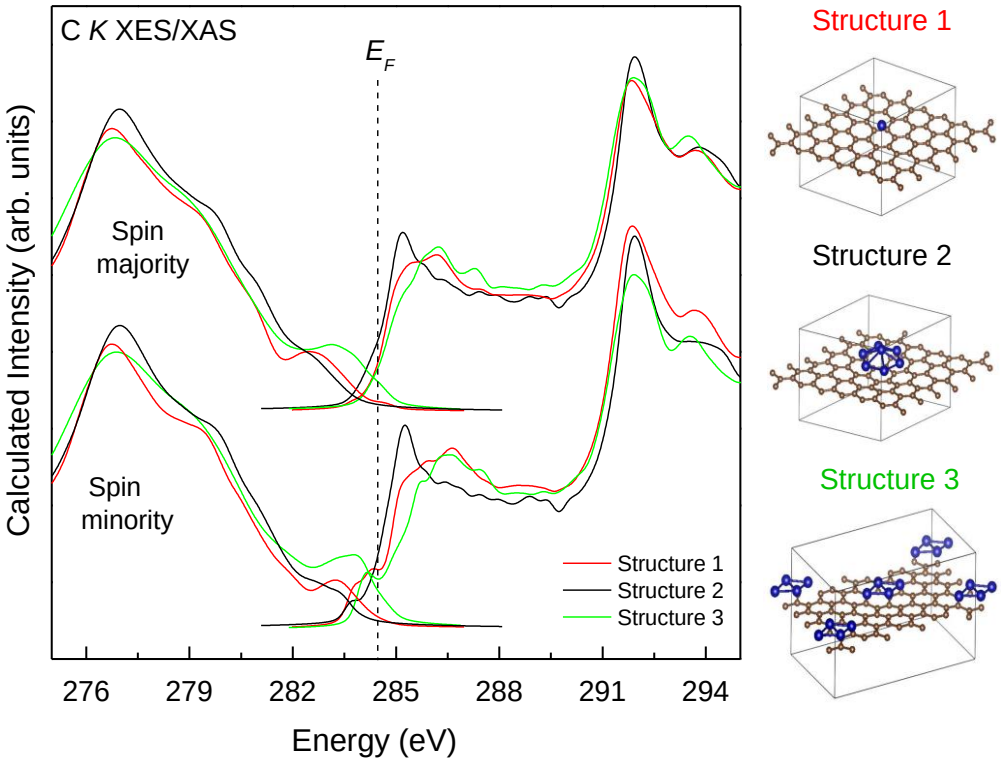

Figure 3.21. Simulated density of 2*p* states for graphene decorated with Co in three different structures. The marked energy location of the Fermi level shows a closed band gap for all cases.

3.5.2 Cobalt Oxide (CoO) on Graphene

Given that XAS has determined that CoO does in fact form on the surface of graphene, simulations were also performed for this system. DFT simulations for this system were also performed using WIEN2k by a similar process, with the calculation parameters as follows. A 5x5 supercell of graphene (50 carbon atoms) was constructed, with 20 angstroms of vacuum added as isolation between neighboring cells (Figure 3.22).

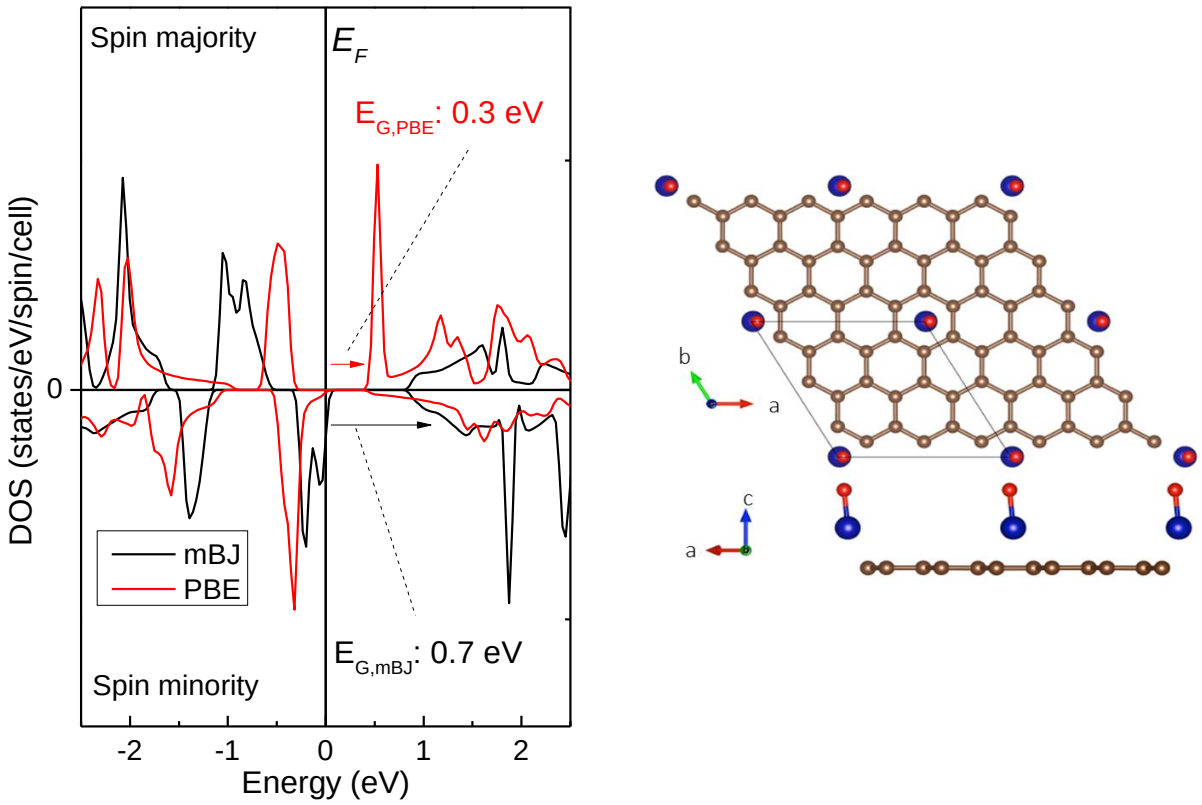

Figure 3.22. Simulated density of 2p states for graphene decorated with CoO monomers (Left). Schematic representation of the CoO/Graphene system (right).

A single Co was positioned and relaxed until all forces were below 1 mRy/a.u., with the relaxation process repeated when an O was added above the Co. A gamma-point centered mesh of 20 points was sampled in k-space, with a plane wave expansion for up to RK_max of 5.0, and an convergence of 0.1 mRy was achieved, with all forces being less than 1 Ry/a.u. Muffin tin sphere sizes were C:1.28 Bohr, Co:1.49 Bohr and O: 1.28 Bohr. The PBE functional [87] as well as the modified Becke-Johnson potential [88] were used. Dispersion forces were corrected in the force relaxation through the use of the DFT-D3 code [68].

Notably after force relaxation the underlying graphene sheet does not buckle or otherwise become deformed as in the case of Co metallic clusters. CoO molecules were found to preferentially occupy the hollow sites above the hexagonally symmetric vacancies in graphene rings, as supported by previous studies [89,90]. Figure 3.22 shows the results of a total DOS simulation for a CoO decorated graphene sheet. Upon introduction of CoO and force relaxation using the Perdew–Burke–Ernzerhof (PBE) functional, a semiconducting gap develops in spin channels for both the total and carbon 2*p* partial DOS. Similar calculations using GGA plus van der Waals correction (with the DFT-D3 code) with adsorbed CoO exhibit a band gap opening in the total DOS (including the carbon 2*p* projection) when a Co surface loading above 11% is used (for example in the case of one CoO isolated on a 3x3 graphene unit cell). At lower CoO surface loading, the graphene layer remains with a closed band gap. Since GGA in the PBE formulation is widely known to underestimate band gaps in materials, the Tran-Blaha modified Becke-Johnson (mBJ) potential was also applied as a correction. This results in the band gap of 0.3 eV increasing to 0.7 eV due to CoO surface loading alone [91]. The gap is opened by hybridization of Co 3*d*4*s* with graphene 2*p* states. Electrons in hybridized orbitals are then partially localized by the Co-O bond. This localization effectively makes these electrons unavailable for conduction, resulting in

partially filled states near the valence band edge and a band gap opening. Although this system was not developed experimentally, it shows that only CoO may be required to open a band gap in graphene. This effect may contribute to the band opening observed in Co/Graphene/SiO_2.

3.6 Band Gap opening Mechanism

With the results presented, we can speculate that the mechanism of band opening is related to Co-mediated oxidation of the graphene and formation of cobalt oxides and graphene oxide. For single layer graphene, charge transfer alone from metallic impurities does not open a semiconducting gap, but rather shifts the Fermi level according to the doping type as in the case of Graphene transferred to a Co substrate. In the Co/graphene system, a two-step process takes place beginning with charge transfer to the graphene, followed by oxidation of both the Co and the graphene. When Co is in close proximity (3 Å) to graphene, minor charge doping of the graphene can occur without bonding between Co and C [92]. This results in a higher electron charge on the graphene locally, and greater affinity for covalent bonding with oxygen. As observed in the XAS, oxygen functional groups form more readily in the presence of Co, but are also mediated by it to proportional concentration by formation of CoO. A band gap may be opened due to sp^3 and sp^2 bond formation when a high enough oxygen concentration is reached in the form carbonyl, epoxide, carboxyl, or hydroxyl groups. Effectively the local area of graphene around the Co clusters is converted to graphene oxide. Although oxygen functional groups are natively present in the graphene after transfer, they are not in sufficient concentration to induce a band gap alone. This method of band opening in graphene is well known in graphene oxide, but in this case it is controlled using metal deposition. There is also an effect from CoO formation alone shown

by calculation that cannot be discounted and may also contribute to the band opening. However, due to the oxidation of the graphene used as part of the sample preparation procedure, it was not possible to experimentally isolate the effect of CoO alone. $CoCO_3$ may also contribute to sequestration of oxygen, but as discussed above at nominal Co thickness to produce a band gap, carbonates are not present in sufficient concentration to greatly affect the band gap formation.

CHAPTER 4

CONCLUSIONS

In summary, I have discussed the electronic characteristics of Graphene-Copper and Cobalt-Graphene systems in the context of oxidation protection and band gap opening, respectively. To investigate the protective properties of graphene, graphene/Cu samples were prepared and exposed to ambient atmosphere for times ranging from 1 month to 1.5 years. Electronic structure characterizations of these samples reveal that although graphene becomes contaminated with oxygen functional groups, it does provide a long term barrier to oxidation for an underlying copper substrate in ambient atmosphere at room temperature.

For Graphene-cobalt systems, cobalt was deposited by PVD as both a substrate for the graphene and as top decorating layer. The surface of these samples was characterized for both the distribution of cobalt clusters on the surface and the condition of the graphene. Raman measurements show the graphene does not fragment or become heavily damaged below 0.25 nm of Co deposited on its surface. This is because Co prefers to nucleate at impurity sites in graphene to form clusters on the surface that do not break nearby C-C bonds in the graphene. AFM images of the surface support this finding showing cluster growth up to about 0.25 nm of Co when the coverage begins to become more homogeneous. X-ray spectroscopy techniques were used to probe the graphene 2*p* density of states, revealing a band gap of up to 0.30 ± 0.10 eV due to Co deposited on the surface. The mechanism has been proposed to be oxygen functional group formation mediated by the Co and cobalt oxides to produce local areas of graphene oxide. Electronic structure calculations also reveal a contribution to the band gap opening from CoO

alone where graphene 2*p* electrons in hybridized orbitals are partially localized by the Co-O bond, leading to a band gap opening.

Co/graphene may be attractive for use in patterned electronic devices by using masking to deposit on a selected area of a graphene substrate. Cobalt-mediated oxidation is therefore scalable to the maximum size of graphene sheets that can be obtained by conventional growth techniques. Most importantly, the band gap produced is of sufficient size to be of use in semiconducting applications, and is stable at room temperature under exposure to ambient conditions. Indeed, the band gap requires exposure to oxygen to form. This method is unique in that a band gap is formed only in the local area where Co is deposited without greatly deforming or damaging the graphene. Damage and fragmentation of graphene are a weakness of other fabrication methods that rely on solution-based methods with thermal heating to functionalize graphene in a controllable way. Disadvantages of this technique centers around the requirement for single layer CVD graphene that must be transferred to other substrates. The transfer process using a sacrificial layer unavoidably introduces contaminants to the graphene surface that may vary in concentration between fabrication runs. The process of opening a band gap using metal mediated oxidation depends highly on the condition of the graphene sample in terms of native oxidation and number of defects both before and after the solution transfer. Since the growth mode of Co has been determined to be nucleation at impurity sites, the homogeneity and size of Co clusters depends not only on the Co thickness but also the number and type of defects present. Therefore, successful implementation of this method requires careful preparation of the initial graphene sample and testing of its condition at each step in the fabrication process.

Graphene is and will continue to be an exciting material for use in electronic devices. Its unique electronic structural properties make it applicable in many novel applications including protection

of metals from electrochemical exposure or as a semiconductor in electronic and spintronic devices. The potential ways to modify it are also deep and varied, and opening a band gap is certainly possible by several methods. Metal mediated oxidation presents another feasible path to modify graphene for its potential use as a semiconductor in electronic devices.

CHAPTER 5

FUTURE WORK

5.1 X-ray Magnetic Circular Dichroism of Co/Graphene/SiO_2

X-ray spectroscopy studies to probe the magnetic characteristics of Co/Graphene were also performed in the form of X-ray magnetic circular dichroism (XMCD) measurements. XMCD uses circularly polarized X-rays to preferentially excite electrons in one spin channel. It can therefore be used to probe for ferromagnetism since such materials are not spin neutral. XMCD can be used to probe spin polarization in graphene/metal systems. Dedkov *et al.* showed evidence of dichroism in C 1*s* XMCD spectra of a graphene/Ni(111) sample in π^* states originating from hybridized C p_z–Ni 3*d* and C p_z–Ni p_x,p_y,3*d* states [93]. Literature studies employing *ab initio* calculations of Fe, Co, and Mn-Graphene systems show polarization of the graphene DOS and other interesting behavior for cases of increased charge carrier concentration or gating [94,40]. This suggests spin polarization of graphene p_z states which could be used for device applications, with the Co/graphene system in this study a potential candidate.

Figures 5.1 and 5.2 show XMCD measurements (TFY and TEY respectively) performed using a magnetic sample plate with B = 0.7 T and circularly left and right polarized light. TFY measurements were performed with the field parallel to the surface plane and TEY with the field perpendicular to the surface.

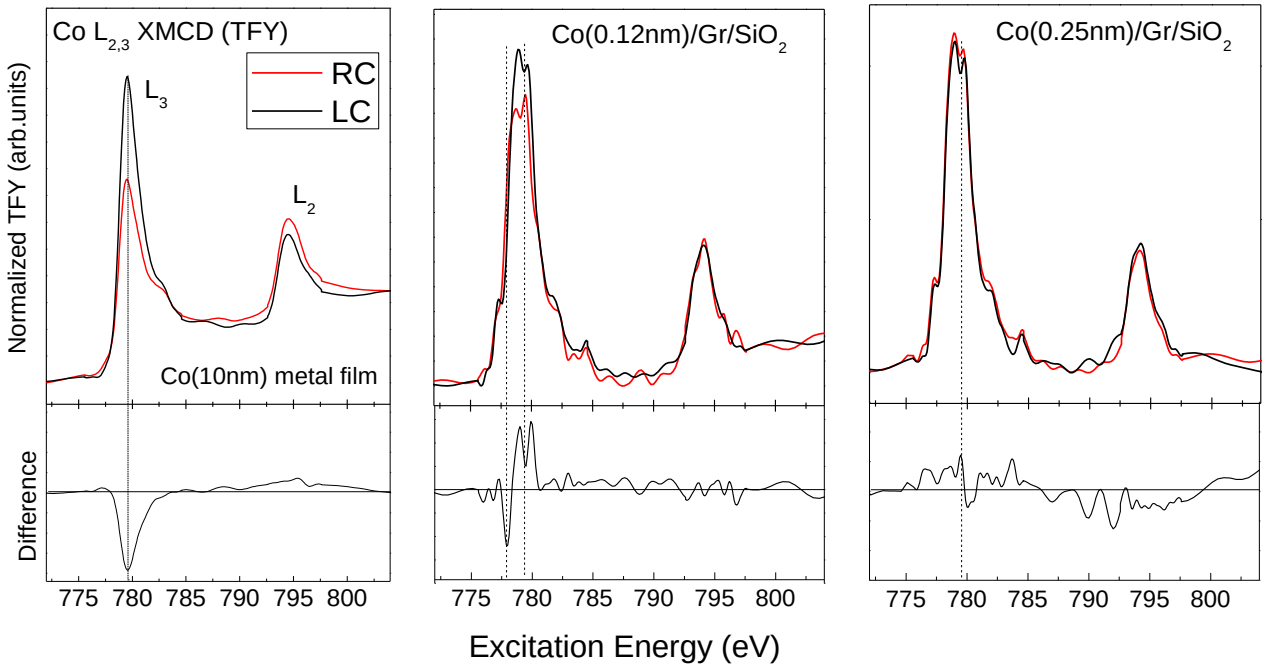

Figure 5.1. XMCD results for Co/Graphane/SiO_2 using TFY and a field parallel to the substrate. 5 point FFT smoothing was used on Co/Graphene/SiO_2 spectra.

A clear MCD signal is evident for the Co(10nm) thin film, showing clear ferromagnetism from the difference spectrum [37]. The interpretation of the other spectra is somewhat ambiguous due to the quality of the spectrum. In practice, a parallel field can only be created with a recessed holder where the samples sits inside a box of magnets with one opening. Due to this much of the fluorescence that would normally fall on the detector is blocked, resulting is noisy data. Even with a 5 second dwell time per data point (normally 1 s is sufficient), a 5 point FFT smoothing was also necessary to display the difference spectrum of TFY measurements. Notably TEY measurements were found to be impossible to obtain because of the large magnetic field and location of the sample. It was found that electrons ejected from the surface are accelerated into the sides of the

magnet box by the magnetic field (thus neutralizing the sample) faster than the TEY signal could be measured. To avoid this difficulty, a perpendicular field arrangement was also used, allowing TEY to be more easily collected. An MCD signal is evident for both 0.06 and 0.12 nm of Co, but the difference is very low intensity. This is reasonable when previous results are considered showing CoO is the primary phase at this thickness, which is antiferromagnetic. The small difference does however indicate there is some ferromagnetic Co in small clusters. At 0.25 nm, the MCD signal is present but less coherent, similar to the TFY results.

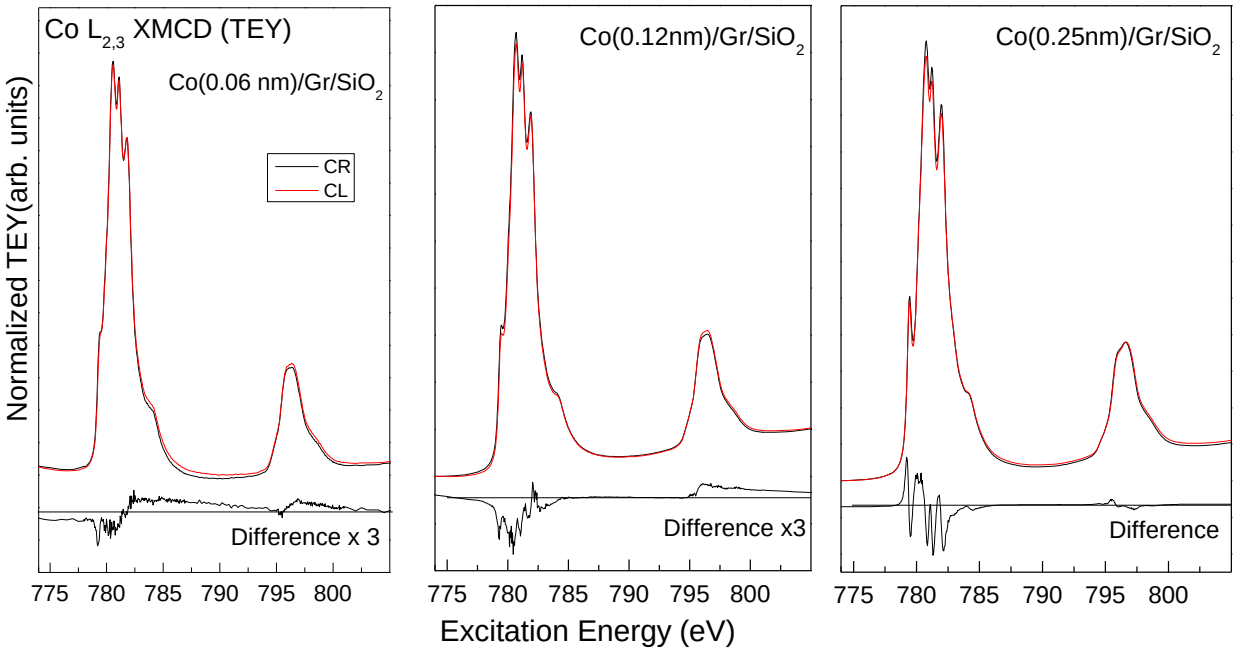

Figure 5.2. XMCD results for Co/Graphane/SiO_2 using TEY and a field parallel to the substrate. 5 point FFT smoothing was used on Co/Graphene/SiO_2 spectra.

An MCD signal is evident for 0.06 and 0.12 nm, but is very small in intensity. Future measurements on this system should employ X-ray linear magnetic dichroism (XMLD) to probe for antiferromagnetic CoO. This line of work may be promising for device applications because

ferromagnetic or antiferromagnetic clusters could be utilized as a spin polarized layer in spintronic devices.

5.1 Other Transition Metals on Graphene

In addition to cobalt, some preliminary work has been planned concerning other transition metals deposited on graphene, mainly Mn, Fe, and Ni deposited on Graphene/Cu. These materials were predicted to have similar exchange coupling effects to Co and are also candidates for band gap opening. Graphene/Ni(111) is one of the most heavily studied graphene-metal systems. When graphene is grown on Ni, hybridization between Ni 3*d* states and graphene can result in a band gap of 10-20 meV [44]. Studies of metallic clusters are not as prevalent, but some have examined Fe, Co, and Ni clusters deposited on graphene surfaces with many experimental techniques, but have not revealed a band gap [45,46]. Future work in this area is planned with deposition of metal clusters and analysis by a similar method presented in this study.

5.3 Graphene on Arbitrary Substrates

In the course of this study it became clear that using Graphene/Cu has significant drawbacks in terms of a requirement of transfer to other substrates. Only certain substrates such as Nickel, Copper or Ruthenium are used because graphene growth is a catalytic process. Similar drawbacks for substrates other than Cu exist in that the graphene may need to be transferred to another material. Ru is also quite expensive when one is considering materials, and is not appropriate for large area or sacrificial substrates. Growing on these substrates by CVD can give high quality, large area graphene, but with the added complexity of transferring it for a specific application.

One possible route is to devise a method of growing CVD graphene without the requirement for a Cu substrate seed to promote the growth. Studies have shown other substrates are suitable, such as hexagonal boron nitride (h-BN) [95,96]. h-BN has an advantage over other metallic substrates in that it is non-reactive and according to theory should not perturb the graphene band structure [97]. But even this is not ideal as h-BN may also not be the desired substrate – what is needed is a method that can deposit graphene onto any arbitrary substrate. Methods have been proposed [98], but an experimental example of graphene grown on an arbitrary substrate remains elusive. Alternatively, a more robust transfer method could be used that does not leave contaminants on the graphene as the PMMA method is known to do. Some modifications to the procedure can be found in the literature, but they still rely on PMMA or another similar material as a sacrificial layer [99].

For graphene to be successfully integrated into next-generation electronic devices, a versatile and robust growth method needs to be developed. This will allow graphene to be deposited at any stage in fabrication of a device, and also increase the graphene quality by avoiding damage due to a chemical transfer process.

5.4 Electronic structure calculations of Co-Graphene systems

In addition to the systems investigated here computationally, further work should be done on graphene-cobalt systems with different configurations of Co on the surface. From the results presented here the cobalt clusters on the graphene surface are cobalt oxides, but the exact structure is unclear. A system that would better approximate that under study would be Co clusters ranging in size from 10-50 atoms with a generally amorphous structure containing

octahedral phases. Cobalt carbonates and $Co[OH]_2$ groups should also be included in the system besides CoO to fully account for all of the phases of cobalt present. Furthermore a distribution of oxygen functional groups should also be added in the vicinity of the Co clusters to ideally account for all the changes to the graphene. Band structure calculations using WIEN2K or SIESTA of such a system would provide a more accurate representation of the samples that have been studied experimentally.

LIST OF REFERENCES

[1] K. Novoselov, A. Geim, S. Morozov, D. Jiang, Y. Zhang, S. Dubonos, I. Grigorieva, A. Firsov. Electric Field Effect in Atomically Thin Carbon Films. *Science*. 306**:**666-669, 2004.

[2] H. P. Boehm, A. Clauss, G. O. Fischer, U. Hofmann, Z. Dünnste Kohlenstoff-Folien. *Naturforsch. B.* 17**:**150-153, 1962.

[3] E.P. Randviir, D. A.C. Brownson, C. E. Banks. A decade of graphene research: production, applications and outlook. *Mater. Today*. 17:426-432, 2014.

[4] A.K. Geim. Graphene prehistory. *Phys. Scr*. T146:014003, 2012.

[5] W. S. Hummers Jr., R. E. Offeman. Preparation of Graphitic Oxide. *J. Am. Chem. Soc*. 80: 1339–1339, 1958.

[6] A.J. Van Bommel, J. E. Crombeen, A. Van Tooren. LEED and Auger electron observations of the SiC(0001) surface. *Surf. Sci*. 48:463–472, 1975.

[7] J. Park, W. H. Lee, S. Huh, S. H. Sim, S. B. Kim, K. Cho, B. H. Hong, K. S. Kim. Work-Function Engineering of Graphene Electrodes by Self-Assembled Monolayers for High-Performance Organic Field-Effect Transistors. *J. Phys. Chem. Lett.* 2:841–845, 2011.

[8] G. Eda, A. Nathan, P. Wöbkenberg, F. Colleaux, K. Ghaffarzadeh, T. D. Anthopoulos, M. Chhowalla. Graphene oxide gate dielectric for graphene-based monolithic field effect transistors. *App. Phys. Lett.* 102:133108, 2013.

[9] C. X. Guo, H. B. Yang, Z. M. Sheng, Z. S. Lu, Q. L. Song, C. M. Li. Layered Graphene/Quantum Dots for Photovoltaic Devices. *Angew. Chem. Int. Ed*. 49:3014 – 3017, 2010.

[10] J.-M. Yun, J.-S. Yeo, J. Kim, H.-G. Jeong, D.-Y. Kim, Y.-J. Noh, S.-S. Kim, B.-C. Ku, S.-I. Na. Solution-Processable Reduced Graphene Oxide as a Novel Alternative to PEDOT:PSS Hole Transport Layers for Highly Efficient and Stable Polymer Solar Cells. *Adv. Mater*. 23:4923–4928, 2011.

[11] J. T. Robinson, F. K. Perkins, E. S. Snow, Z. Wei, P. E. Sheehan. Reduced Graphene Oxide Molecular Sensors. *Nano Lett.* 8:3137-3140, 2008.

[12] D. Prasai, J. C. Tuberquia, R. R. Harl, G. K. Jennings, K. I. Bolotin. Graphene: Corrosion-Inhibiting Coating. *ACS Nano*. 6:1102–1108, 2012.

[13] J. Bai, R. Cheng, F. Xiu, L. Liao, M. Wang, A. Shailos, K. L. Wang, Y. Huang, X. Duan. Very large magnetoresistance in graphene nanoribbons. *Nat. Nanotechnol*. 5:655-659 2010.

[14] Thomson Reuters Blog (accessed January 2105) http://blog.thomsonreuters.com/index.php/graphene-patents-graphic-of-the-day/

[15] K. S. Novoselov, V. I. Fal'ko, L. Colombo, P. R. Gellert, M. G. Schwab, K. Kim. A roadmap for graphene. *Nature.* 490:192-200, 2012.

[16] C. Lee, X. Wei, J. W. Kysar, J. Hone. Measurement of the Elastic Properties and Intrinsic Strength of Monolayer Graphene. *Science*. 321:385-388, 2008.

[17] K. S. Novoselov, A. K. Geim, S. V. Morozov, D. Jiang, M. I. Katsnelson, I. V. Grigorieva, S. V. Dubonos, A. A. Firsov. Two-dimensional gas of massless Dirac fermions in graphene. *Nature.* 438:197–200, 2005.

[18] Y.Zhang, Y.-W Tan, H. L. Stormer, P. Kim. Experimental observation of the quantum Hall effect and Berry's phase in graphene. *Nature.* 438:201–204, 2005.

[19] Y. Zhang, J. P. Small, M. E. S. Amori, P. Kim. Electric field modulation of galvanomagnetic properties of mesoscopic graphite. *Phys. Rev. Lett*. 94:176803, 2005.

[20] K.I. Bolotina, K.J. Sikes, Z. Jianga, M. Klima, G. Fudenberg, J. Honec, P. Kima, H.L. Stormer. Ultrahigh electron mobility in suspended graphene. *Solid State Commun*. 146:351–355, 2008.

[21] A. H. Castro Neto, F. Guinea, N. M. R. Peres, K. S. Novoselov, A. K. Geim. The electronic properties of graphene. *Rev. Mod. Phys*. 81:109-162, 2009.

[22] P. R. Wallace. The Band Theory of Graphite. *Phys. Rev.* 71:622-634, 1947.

[23] V. Ariel. Effectve Mass and Energy-Mass Relationship. *arXiv*:1205.3995v1 [physics.gen-ph], 2012.

[24] Y. Zhang, T.-T. Tang, C. Girit, Z. Hao, M.C. Martin, A. Zettl, M. F. Crommie, Y. R. Shen, F. Wang. Direct observation of a widely tunable bandgap in bilayer graphene. *Nat. Lett*. 459:820-823, 2009.

[25] C. H. Lui, Z. Li, K. F. Mak, E. Cappelluti, T. F. Heinz. Observation of an electrically tunable band gap in trilayer graphene. *Nat. Phys*. 7:944–947, 2011.

[26] A. J. Samuels, J. D. Carey. Molecular Doping and Band-Gap Opening of Bilayer Graphene. *ACS Nano.* 7:2790–2799, 2013.

[27] A. Nourbakhsh, T. K. Agarwal, Al. Klekachev, I. Asselberghs, M. Cantoro, C. Huyghebaert, M. Heyns, M. Verhelst, A. Thean, S. De Gendt. *Nanotechnol*. 25:345203, 2014.

[28] S.-H Cheng, K. Zou, F. Okino, H. R. Gutierrez, A. Gupta, N. Shen, P. C. Eklund, J. O. Sofo, , J. Zhu. *Phys. Rev. B.* 81:205435, 2010.

[29] R.R. Nair, W. Ren, R. Jalil, I. Riaz, V. G. Kravets, L. Britnell, P. Blake, F. Schedin, A. S. Mayorov, S. Yuan, M. I. Katsnelson, H.-M. Cheng, W. Strupinski, L. G. Bulusheva, A. V. Okotrub, I. V. Grigorieva, A. N. Grigorenko, K. S. Novoselov, A. K. Geim. Fluorographene: A two-dimensional counterpart of teflon. *Small*. 6:2877, 2010.

[30] L. Wang, X. Xie, W. Zhang, J. Zhang, M. Zhu, Y. Guo, P. Chen, M. Liu, G. Yu. Tuning the light response of organic field-effect transistors using fluorographene nanosheets as an interface modification layer. *J. Mater. Chem. C.* 2:6484, 2014,

[31] K.-I Ho, J.-H. Liao, C.-H. Huang, C.-L. Hsu, W. Zhang, A.-Y. Lu, L.-J. Li, C.-S. Lai, C.-Y. Su. One-Step Formation of a Single Atomic-Layer Transistor by the Selective Fluorination of a Graphene Film. *Small*. 10:989–997, 2014.

[32] M. Acik, Y. J. Chabal. A Review on Thermal Exfoliation of Graphene Oxide. *J. Mater. Sci. Res.* 2:101-112, 2013.

[33] T. K. Truong, T.N.T. Nguyen, T. Q. Trung, I. Y. Sohn, D.-J. Kim, J.-H. Jung, N.-E. Lee. Reduced graphene oxide field-effect transistor with indium tin oxide extended gate for proton sensing. *Current Appl. Phys*. 14:738e743, 2014.

[34] Y.-C. Chen, D. G. de Oteyza, Z. Pedramrazi, C. Chen, F. R. Fischer, M. F. Crommie, *ACS Nano*. 7:6123–6128, 2013.

[35] X. Li, X. Wang, L. Zhang, S. Lee, H. Dai. Chemically Derived, Ultrasmooth Graphene Nanoribbon Semiconductors. *Science*. 319: 1229-1232, 2008.

[36] K. K. Kim, A. Reina, Y. Shi, H. Park, L.-J. Li, Y. H. Lee, J. Kong. Enhancing the conductivity of transparent graphene films via doping. *Nanotechnol.* 2010, 21, 28520.

[37] E. Kan, Z. Li, J. Yang. *Graphene Nanoribbons: Geometric, Electronic, and Magnetic Properties, Physics and Applications of Graphene – Theory*; Dr. Sergey Mikhailov (Ed.), InTech, 2011. ISBN: 978-953-307-152-7, Available from: http://www.intechopen.com/books/physics-and-applications-of-graphenetheory/graphene-nanoribbons-geometric-electronic-and-magnetic-properties.

[38] M. Acik, Y. J. Chabal. Nature of Graphene Edges: A Review. *Jap. J. of Appl. Phys.* 50:070101, 2011.

[39] J. Stöhr, H. C. Seigmann. *Magnetism*; Springer Verlag, 2006. ISBN: 978-3-540-30282-7.

[40] S. R. Power, M. S. Ferreira. Indirect Exchange and Ruderman-Kittel-Kasuya-Yosida (RKKY) Interactions in Magnetically-Doped Graphene. *arXiv*:1301.1779v2 [cond-mat.mes-hall], 2013.

[41] P. D. Gorman, J. M. Duffy, M. S. Ferreira, and S. R. Power. RKKY interaction between adsorbed magnetic impurities in graphene: Symmetry and strain effects. *Phys. Rev. B.* 88:085405, 2013.

[42] T. G. Rappoport, M. Godoy, B. Uchoa, R. R. dos Santos, A. H. Castro Neto. Magnetic exchange mechanism for electronic gap opening in graphene. *Europhys. Lett*. 96:27010, 2011.

[43] R. Garg, N. K. Dutta, N. R. Choudhury. Work Function Engineering of Graphene. *Nanomaterials*. 4:267-300, 2014.

[44] H.-J. Shin, W. M. Choi, D. Choi, G. H. Han, S.-M. Yoon, H.-K. Park, S.-W. Kim, Y. W. Jin, S. Y. Lee, J. M. Kim, J.-Y. Choi, Y. H. Lee. Control of Electronic Structure of Graphene by Various Dopants and Their Effects on a Nanogenerator. *J. Am. Chem. Soc.* 132:15603–15609, 2014.

[45] K. Gotoh, T. Kinumoto, E. Fujii, A. Yamamoto, H. Hashimoto, T. Ohkubo, A. Itadani, Y. Kuroda, H. Ishida. Exfoliated graphene sheets decorated with metal / metal oxide nanoparticles: simple preparation from cation exchanged graphite oxide. *Carbon.* 49:1118 –1125, 2011

[46] S. M. Song, J. K. Park, O. J. Sul, B. J. Cho. Determination of Work Function of Graphene under a Metal Electrode and Its Role in Contact Resistance. *Nano Lett*. 12:3887−3892, 2012.

[47] A. Dahal, M. Batzill. Graphene–nickel interfaces: a review. *Nanoscale*. 6:2548, 2014.

[48] T. Eelbo, M. Wasniowska, P. Thakur, M. Gyamfi, B. Sachs, T. O. Wehling, S. Forti, U. Starke, C. Tieg, A. I. Lichtenstein, R. Wiesendanger. Adatoms and Clusters of 3d Transition Metals on Graphene:Electronic and Magnetic Configurations. *Phys. Rev. Lett.* 110:136804, 2013

[49] V.W. Brar, R. Decker, H.-M. Solowan, Y. Wang, L. Maserati, K. T. Chan, H. Lee, C. O. Girit, A. Zettl, S. G. Louie, M. L. Cohen, M. F. Crommie. Gate-controlled ionization and screening of cobalt adatoms on a graphene surface. *Nat. Phys.* 7:43-47, 2011.

[50] Farrel W. Lytle. The EXAFS family tree: a personal history of the development of extended X-ray absorption fine structure. *J. Synchrotron Rad.* 6:123-134, 1999.

[51] R. Stumm von Bordwehr. A history of x-ray absorption fine structure. *Ann. Phys. (Paris),* 14:377-465, 1989.

[52] UC Davis Chem Wiki. (accessed February 1, 2015). http://chemwiki.ucdavis.edu/.

[53] J. J. Jia, T. A. Callcott, J. Yurkas, A. W. Ellis, F. J. Himpsel, M. G. Samant, J. Stöhr, D. L. Ederer, J. A. Carlisle, E. A. Hudson, L. J. Terminello, D. K. Shuh, R. C. C. Perera. First experimental results from IBM/TENN/TULANE/LLNL/LBL undulator beamline at the Advanced Light Source. *Rev. Sci. Instrum*. 66:1394-1397, 1995.

[54] REIXS: XES endstation. (accessed January 26, 2015). http://exshare.lightsource.ca/REIXS/Pages/XES.aspx

[55] A. J. Achkar, T. Z. Regier, H. Wadati, Y.-J. Kim, H. Zhang, D. G. Hawthorn. Bulk sensitive x-ray absorption spectroscopy free of self-absorption effects. *Phys. Rev. B.* 83:081106(R) 2011.

[56] M. O. Krause. Atomic Radiative and Radiationless Yields for K and L Shells. *J. Phys. Chem. Ref. Data.* 8:307, 1979.

[57] A. C. Thompson, D. T. Attwood, E. M. Gullikson, M. R. Howells, J. B. Kortright, A. L. Robinson, J. H. Underwood, K.-J. Kim, J. Kirz, I. Lindau, P. Pianetta, H. Winick, G. P. Williams, J. H. Scofield. *X-Ray Data Booklet*. Lawrence Berkeley National Labratory, 2009.

[58] J. J. Sakurai, J. Napolitano. *Modern Quantum Mechanics*; Ch. 5, pages 365-368. Addison-Wesley, San Francisco, CA, 2nd edition, 1994. ISBN-13: 978-0805382914.

[59] H. Ebert, J. Stöhr, S. S. P. Parkin, M. Samant, and A. Nilsson. L-edge x-ray absorption in fcc and bcc Cu metal: Comparison of experimental and first-principles theoretical results. *Phys. Rev. B.* 53:16067-16073, 1996.

[60] J. Stöhr. *NEXAFS Spectroscopy*; Springer-Verlag, 1992. ISBN 978-3-662-02853-7.

[61] P. van der Heide. *X-Ray Photoelectron Spectroscopy: An Introduction to Principles and Practices;* John Wiley & Sons, Inc., Hoboken, New Jersey, 2012. ISBN 9781118162897.

[62] F. de Groot. Multiplet Effects in X-ray Spectroscopy. *Coord. Chem. Rev*. 249:31–63, 2005.

[63] F. de Groot, A. Kotani. *Core Level Spectroscopy of Solids; Advances in Condensed Matter Science Series*; CRC Press: Boca Raton, FL, 2008. ISBN-13: 978-0849390715.

[64] S. C. Das, R. J. Green, J. Podder, T. Z. Regier, G. S. Chang, A. Moewes. Band gap tuning in ZnO through Ni doping via spray pyrolysis. *J. Phys. Chem. C*. 117:12745−12753, 2013.

[65] F.M.F. de Groot, R. K. Hocking, C. Piamonteze, B. Hedman, K.O. Hodgson, E.I. Solomon. New Developments in Charge Transfer Multiplet Calculations: Projection Operators, Mixed-Spin States and π-Bonding. Contributed to 13th International Conference On X-Ray Absorption Fine Structure (XAFS13), July 9-14, 2006, Stanford, California.

[66] P. Hohenberg, W. Kohn. Inhomogeneous Electron Gas. *Phys. Rev.* 136:864, 1964.

[67] W. Kohn, L. J. Sham. Self-Consistent Equations Including Exchange and Correlation Effects. *Phys. Rev*. 140:1133, 1965.

[68] R. Catlow, E. Kotomin. *Computational Materials Science*; IOS Press, Amsterdam, Netherlands, 2003. ISBN 1-58603-335-2.

[69] J. Kohanoff. *Electronic Structure Calculations for Solids and Molecules Theory and Computational Methods*; Cambridge University Press, Cambridge, United Kingdom, 2006. ISBN 9780521815918.

[70] P. Blaha, K. Schwarz, G. Madsen, D. Kvasnicka, J. Luitz, *WIEN2K, An Augmented Plane Wave + Local Orbitals Program for Calculating Crystal Properties*; Universität Wien: Vienna, Austria, 2001. ISBN 3-9501031-1-2.

[71]. D. W. Boukhvalov D. R. Dreyer, C. W. Bielawski, Y-W Son. A Computational Investigation of the Catalytic Properties of Graphene Oxide: Exploring Mechanisms by using DFT Methods. *ChemCatChem*. 4:1844, 2012.

[72]. A. Ye. Yermakov, D. W. Boukhvalov, M. A. Uimin, E. S. Lokteva, A. V. Erokhin, N. N. Schegoleva. Hydrogen dissociation catalyzed by carbon coated nickel nanoparticles: experiment and theory. *ChemPhysChem*. 14:381-385, 2013.

[73] A. C. Ferrari, D. M. Basko. Raman spectroscopy as a versatile tool for studying the properties of graphene. *Nat. Nano.* 8:235-246, 2013.

[74] Raman Spectroscopy (accessed February 5, 2015) http://en.wikipedia.org/wiki/Raman_spectroscopy

[75] L. M. Malard, M. A. Pimenta, G. Dresselhaus, M. S. Dresselhaus. Raman spectroscopy in graphene. *Phys. Rep*. 473:51–87, 2009.

[76] M. W. Iqbal, A. K. Singh, M. Z. Iqbal, J. J. Eo. Raman fingerprint of doping due to metal adsorbates on graphene. *Phys.: Condens. Matter.* 24:335301, 2012.

[77] Atomic Force Microscopy (accessed February 5, 2015) http://en.wikipedia.org/wiki/Atomic_force_microscopy

[78] F. Günes¸ H.-J. Shin, C. Biswas, G. H. Han, E. S. Kim, S. J. Chae, J-Y. Choi, Y.H. Lee. A general method for transferring graphene onto soft surfaces. *ACS Nano.* 4:4595-4600, 2010.

[79] S. Suzuki, Y. Ishikawa, M. Isshiki, Y. Waseda. Native oxide layers formed on the surface of ultra-high-purity iron and copper investigated by angle-resolved XPS. *Mater. Trans.* 38:1004-1009, 1997

[80] J. Iijima, J.-W. Lim, S.-H. Hong, S. Suzuki, K. Mimura, M. Isshiki. Native oxidation of ultra high purity Cu bulk and thin films. *Appl Surf Sci.* 253:2825-2829, 2006.

[81] M. Schriver, W. Regan, W. J. Gannett, A. M. Zaniewski, M. F. Crommie, A. Zettl, Graphene as a Long-Term Metal Oxidation Barrier: Worse Than Nothing. *ACS Nano* 7:5763-5769, 2013.

[82] P. Sutter, J. T. Sadowski, E. A. Sutter. Chemistry under Cover: Tuning metal-Graphene interaction by Reactive Intercalation. *J. Am. Chem. Soc.* 132:8175-8179, 2010.

[83] O. Leenaerts, B. Partoens, F. M. Peeters. Graphene: a perfect nanobaloon. *Appl Phys Lett.* 93:193107, 2008.

[84] J. S. Bunch, S. S. Verbridge, J. S. Alden, A. M. van der Zande, J. N. Parpia. H.gG. Craighead, P. L. McEuen. Impermeable atomic membranes from graphene sheets. *Nano Lett.* 8:2458-2462, 2008.

[85] D. W. Boukhvalov, C. Virojanadara. Penetration of alkali atoms throughout graphene membrane: theoretical modeling. *Nanoscale.* 4:1749-1753, 2012

[86] I.-S.Byun, W. Kim, D. W. Boukhvalov, I. Hwang, J. W. Son, G. Oh, J. S. Choi, D. Yoon, H. Cheong, J. Baik, H.-J. Shin, H. W. Shiu, C.-H. Chen, Y.-W. Son, B. H. Park. Electrical control of nanoscale functionalization in graphene by the scanning probe technique. *NPG Asia Materials*. 6:1-6, 2014.

[87] Y. Zhang, L. Gomez, F. N. Ishikawa, A. Madaria, K. Ryu, C. Wang, A. Badmaev, C. Zhou. Comparison of graphene growth on single-crystalline and polycrystalline Ni by chemical vapor deposition. *J Phys Chem Lett.* 1:3101–3107, 2010.

[88] L. Zhang, E. Pollak. W.-C. Wang, P. Jiang, P.-A. Glans, Y. Zhang, J. Cabana, R. Kostecki, C. Chang, M. Salmeron, J. Zhu, J. Guo. Electronic structure study of ordering and interfacial interaction in graphene/Cu composites. *Carbon*. 50:5316-5322, 2012.

[89] J. F. Moulder, W. F. Stickle, P. E. Sobol, K. D. Bomben. *Handbook of X-ray Photoelectron Spectroscopy*. Perkin-Elmer Corp.: Physics Electronics Div. 1992, pages 86-87.

[90] P. Jiang, D. Prendergast, F. Borondics, S. Porsgaard, L. Giovanett, E. Pach, J. Newberg, H. Bluhm, F. Besenbacher, M. Salmeron. Experimental and theoretical investigation of the electronic structure of Cu_2O and CuO thin films on Cu(110) using x-ray photoelectron and absorption spectroscopy. *J. Chem. Phys*. 138:024704-024709, 2013.

[91] D. Tahir, S. Tougaard. Electronic and optical properties of Cu, CuO and Cu_2O studied by electron spectroscopy. *J Phys: Condens Matter*. 24:175002-175010, 2012.

[92] F. Günes, G. H. Han, K. K. Kim, E. S. Kim, S. J. Chae, M. H. Park, H.-K. Jeong, S.-C. Lim, Y. H. Lee. Large-area graphene-based flexible transparent conducting films. *NANO*. 4:83-90, 2009.

[93] A. Dimiev, D. V. Kosynkin, A. Sinitskii, A. Slesarev, Z. Sun, J. M. Tour. Layer-by-Layer Removal of Graphene for Device Patterning. *Science.* 331:1168-1172, 2011.

[94] R Hawaldar, P. Merino, M. R. Correia, I. Budikin, J. Grácio, J. Méndez J. Large-area high-throughput synthesis of monolayer graphene sheet by Hot Filament Thermal Chemical Vapor Deposition. *Sci Rep*. 2:1-9, 2012.

[95] F. Yang, Y. Liu, W. Wu, W. Chen, L Gao, J. A. Sun. A facile method to observe graphene growth on copper foil. *Nanotechnol*. 23:475705, 2012.

[96] A. Hunt, D. A. Dikin, E. Z. Kurmaev, T. D. Boyko, P Bazylewski, G. S. Chang, A. Moewes. Epoxide Speciation and Functional Group Distribution in Graphene Oxide Paper-Like Materials *Adv. Func. Mater.* 22:3950–3957, 2012.

[97]. D. Barreca, A. Gasparotto, O. I. Lebedev, C. Maccato, A. Pozza, E. Tondello, S.Turnerc G.Van Tendelooc. Controlled vapor-phase synthesis of cobalt oxide nanomaterials with tuned composition and spatial organization. *CrystEngComm,* 12:2185–2197, 2010.

[98] A. Hunt, E. Z. Kurmaev, A. Moewes. A Re-evaluation of How Functional Groups Modify the Electronic Structure of Graphene Oxide. *Adv. Mater.* 26:4870–4874, 2014.

[99] C.-H, Chuang, Y.-F. Wang, Y.-C. Shao, Y.-C. Yeh, D.-Y. Wang, C.-W. Chen, J. W. Chiou, S. C. Ray, W. F. Pong, L. Zhang, J. F. Zhu, J. H. Guo. The effect of thermal reduction on the photoluminescence and electronic structures of graphene oxides. *Sci. Reps.* 4525:1-7, 2014.

[100] A. M. Rao, P. C. Eklund, S. Bandow, A Thess, R. E. Smalley. Evidence for charge transfer in dopedcarbon nanotube bundles from Raman scattering. *Nature*. 388:257–259, 1997.

[101] K. T. Nguyen, A. Gaur, M. Shim. Fano Lineshape and Phonon Softening in Single Isolated Metallic Carbon Nanotubes. *Phys. Rev. Lett.* 98:145504, 2007.

[102] R. A. Jishi, M. S. Dresselhaus. Mode softening and mode stiffening in C_{60} doped with alkali metals. *Phys. Rev. B*. 45:6914–6918, 1992.

[103] Q. M. Ramasse, R. Zan, U. Bangert, D. W. Boukhvalov, Y.-W Son, K. S. Novoselov. *ACS Nano*. 6:4063–4071, 2012.

[104] Boukhvalov, D. W.; Katsnelson, M. I. Destruction of graphene by metal adatoms. *Appl. Phys. Lett.* 95:023109, 2009.

[105] U. Bangert, M. H. Gass, A. L. Bleloch, R. R. Nair, J. Eccles. Nanotopography of graphene. *J. Phys. Status Solidi A*. 206:2115–2119, 2009.

[106] M. H. Gass, U. Bangert, A. L. Bleloch, P. Wang, R. R. Nair, A. K. Geim, Free-standing graphene at atomic resolution. *Nat. Nanotechnol*. 3:676-681, 2008.

[107] Y.-Ch. Lin, C.-C. Lu, C.-H.Yeh, C. Jin, K. Suenaga, P.-W. Chiu. Graphene Annealing: How Clean Can It Be? *Nano Lett.* 12:414−419, 2012.

[108] J. P. Perdew, K. Burke, M. Ernzerhof. Generalized Gradient Approximation Made Simple *Phys. Rev. Lett*. 77:3865−3868, 1996.

[109] F. Tran, P. Blaha. Accurate Band Gaps of Semiconductors and Insulators with a Semilocal Exchange-Correlation Potential. *Phys. Rev. Lett.* 102:226401, 2009

[110] S. Grimme, J. Antony, S. Ehrlich, H. J. Krieg. A consistent and accurate ab initio parametrization of density functional dispersion correction (DFT-D) for the 94 elements H-Pu. *Chem. Phys*. 132:154104, 2010.

[111] Y. Mao, J. Yuan, J. Zhong. Density functional calculation of transition metal adatom adsorption on graphene. *J. Phys. Condens. Matter*. 20:115209, 2008.

[112] C. Cao, M. Wu, J. Jiang, H.-P. Cheng. Transition metal adatom and dimer adsorbed on graphene: Induced magnetization and electronic structures. *Phys. Rev. B*. 81:205424, 2010.

[113] A. N. Rudenko, F. J. Keil, M. I. Katsnelson, A. I. Lichtenstein. Adsorption of cobalt on graphene: Electron correlation effects from a quantum chemical perspective. *Phys. Rev. B*. 86:075422, 2012.

[114] Yu. S. Dedkov, M. Sicot, M. Fonin. X-ray absorption and magnetic circular dichroism of graphene/Ni(111). *J. Appl. Phys.* 107:09E121, 2010.

[115] M. Wang, S. K. Jang, W.-J. Jang, M. Kim, S.-Y. Park, S.-W.Kim, S.-J. Kahng, J.-Y. Choi, R. S. Ruoff, Y. J. Song, S. Lee. A Platform for Large-Scale Graphene Electronics – CVD Growth of Single-Layer Graphene on CVD-Grown Hexagonal Boron Nitride. *Adv. Mater.* 25:2746–2752, 2013.

[116] W. Gannett, W. Regan, K. Watanabe, T. Taniguchi, M. F. Crommie, A. Zettl. Boron nitride substrates for high mobility chemical vapor deposited graphene. *Appl. Phys. Lett.* 98:242105, 2011.

[117] Y. Fan, M. Zhao, Z. Wang, X. Zhang, H. Zhang. Tunable electronic structures of graphene/boron nitride heterobilayers. *Appl. Phys. Lett.* 98:083103, 2011

[118] J. Sun, M. T. Cole, N. Lindvall, K. B. K. Teo, A. Yurgens. Noncatalytic chemical vapor deposition of graphene on high-temperature substrates for transparent electrodes. *Appl. Phys. Lett.* 100:022102, 2012.

[119] J. W. Suk, A. Kitt, C. W. Magnuson, Y. Hao, S. Ahmed, J. An, A. K. Swan, B. B. Goldberg, R. S. Ruoff. Transfer of CVD-Grown Monolayer Graphene onto Arbitrary Substrates. *ACS Nano*. 5:6916–6924, 2011.

[120] E. Z. Kurmaev, A. L. Ankudinov, J. J. Rehr, L. D. Finkelstein, P. F. Karimov, A. Moewes. The L_2:L_3 intensity ratio in soft X-ray emission spectra of 3*d*-metals *J. Electron Spectrosc. Relat. Phenom*. 148:1-4, 2005.

[121] E. Z. Kurmaev, R. G. Wilks, A. Moewes, L. D. Finkelstein, S.N. Shamin, J. Kuneš. Oxygen X-ray Emission and Absorption Spectra as a Probe of the Electronic Structure of Strongly Correlated Oxides. *Phys. Rev. B*. 77:165127, 2008.

[122] P. F. Bazylewski, K. H. Kim, J. L. Forrest, H. Tada, D. H. Choi, G. S. Chang. Side-chain effects on electronic structure and molecular stacking arrangement of PCBM spin-coated films. *Chem. Phys. Lett*. 508:90–94, 2011.

APPENDIX A

SUPPORTING X-RAY DATA

Supporting data in this section includes XPS, XES, and XAS data that confirms the main results gathered in this study, but is not integral to the conclusions. Beginning with XPS, peak fitting was also performed for Co/graphene samples with thicker Co films, up to 2 nm. The fitting for a 2nm film (Figure A.) reveals similar functional groups as are present as for lower thinner Co films. Notably carbonates are present in much greater concentration with thicker Co films, comparable to other functional groups. At this thickness of Co the graphene has also become damaged and is likely many small plates covered by a nearly complete layer of Co.

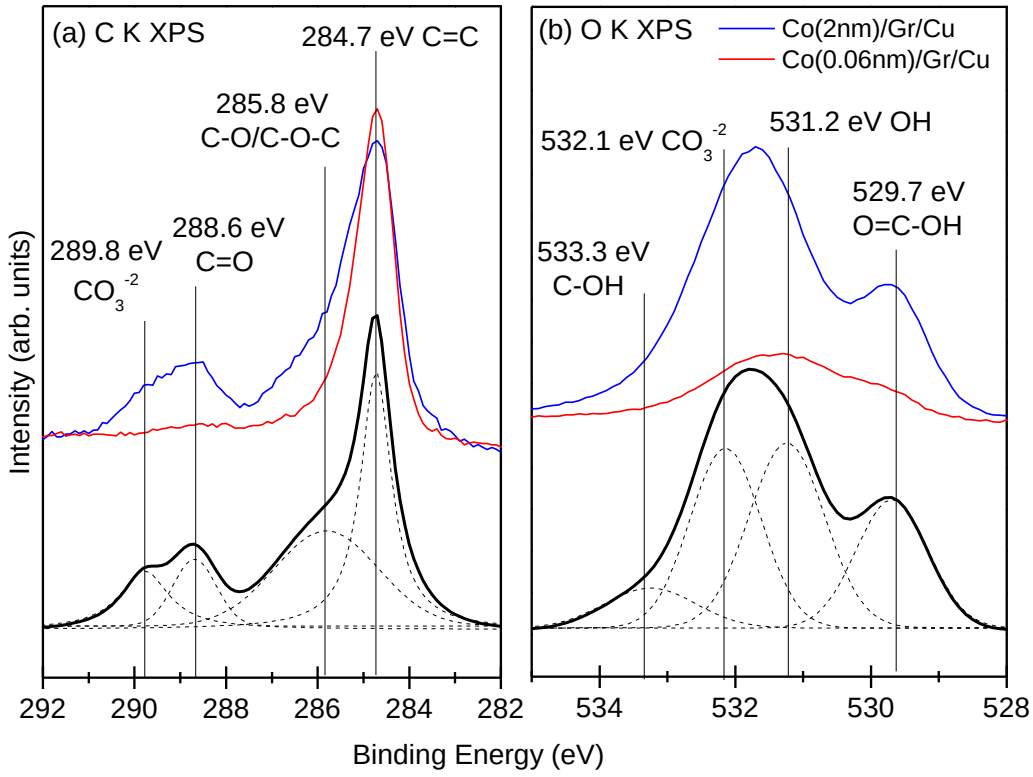

Figure A.1. XPS data for Co(2nm) deposited on Graphene/Cu. The same functional groups are evident with some shifts in peak position to lower energy.

The Co oxidation state can be confirmed by non-resonant Co $L_{2,3}$ XES measurements. Cobalt emission measurements have only been completed for Co(0.12 nm)/Graphene/Cu and some reference samples, as shown in Figure A.2. As can be seen, the relative $I(L_2)/I(L_3)$ intensity ratio for Co(0.12nm)/Graphene/Cu is almost the same as that of CoO powder, and much higher than that of a Co-metal film. The $I(L_2)/I(L_3)$ intensity ratio is related to the number of free *d*-electrons around the element being probed, and is therefore an accurate measure of the oxidation state with appropriate reference [120]. Other variations in the *d*-electron count would produce a significant change in the $I(L_2)/I(L_3)$ intensity ratio, and therefore Co $L_{2,3}$ XES measurements confirm the existence of Co^{2+} in Co(0.12nm)/Graphene/Cu due to CoO. Co $L_{2,3}$ XES measurements were not performed for all samples due to difficulties in acquiring the measurements. Of the beamlines visited to conduct this study only Beamline 8.0.1 at the ALS has sufficient flux to measure the dilute amount of Co in these samples, and there was not time to complete measurements for all samples.

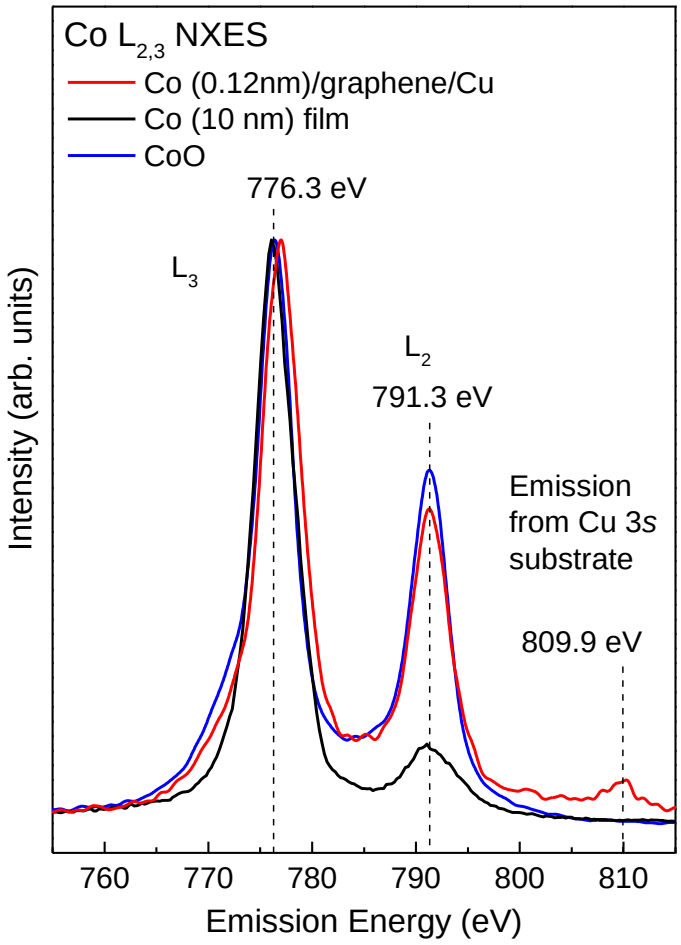

Figure A.2. Co $L_{2,3}$ XES measurements of a Co/Graphene/Cu sample. These results confirm the Co^{+2} oxidation state and CoO formation.

As was discussed for graphene with Co substrate or top coverage, a band gap analysis was also performed for the sandwich three layer architecture with Co on both sides (Figure A.3). Unfortunately after analysis this architecture does not yield a band gap in graphene 2*p* states as was predicted. If linear line fitting is used and the cross over point is marked, we see a shift to higher energy of the crossing point as Co is added in the substrate or on the surface.

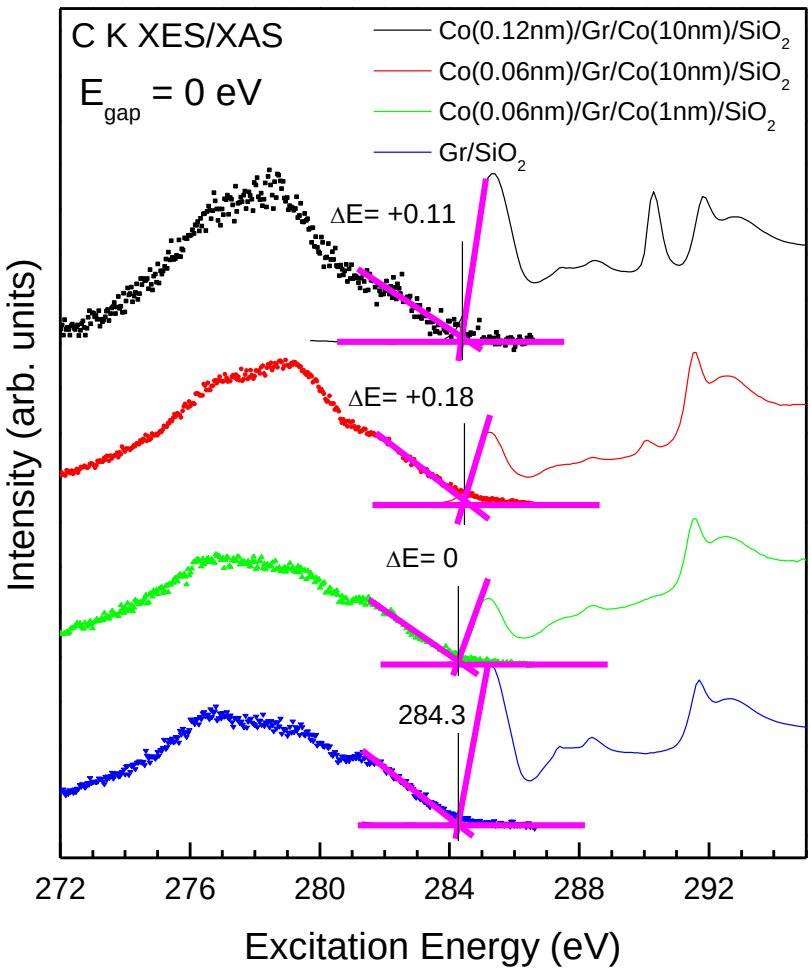

Figure A.3. C *K* XAS and XES of Co/Gr/Co samples to probe for a band gap that may be induced by magnetic exchange processes. No band gap is evident using linear line fitting for any of the cases tested.

A further observation can be made about the XES near the valence band edge. Referring to Figure A.4, there is a noticeable increase in the DOS around 283.7 eV. Careful linear line fitting reveals a shoulder peak due to hybridization of Co 3*d* and C 2*p* states that is not present for Graphene/SiO_2. This shows that Co above a low threshold concentration in the substrate or on the surface provides new hybridized states near the valence band edge that acts to increase the overlap of valence and conduction bands rather than open a band gap.

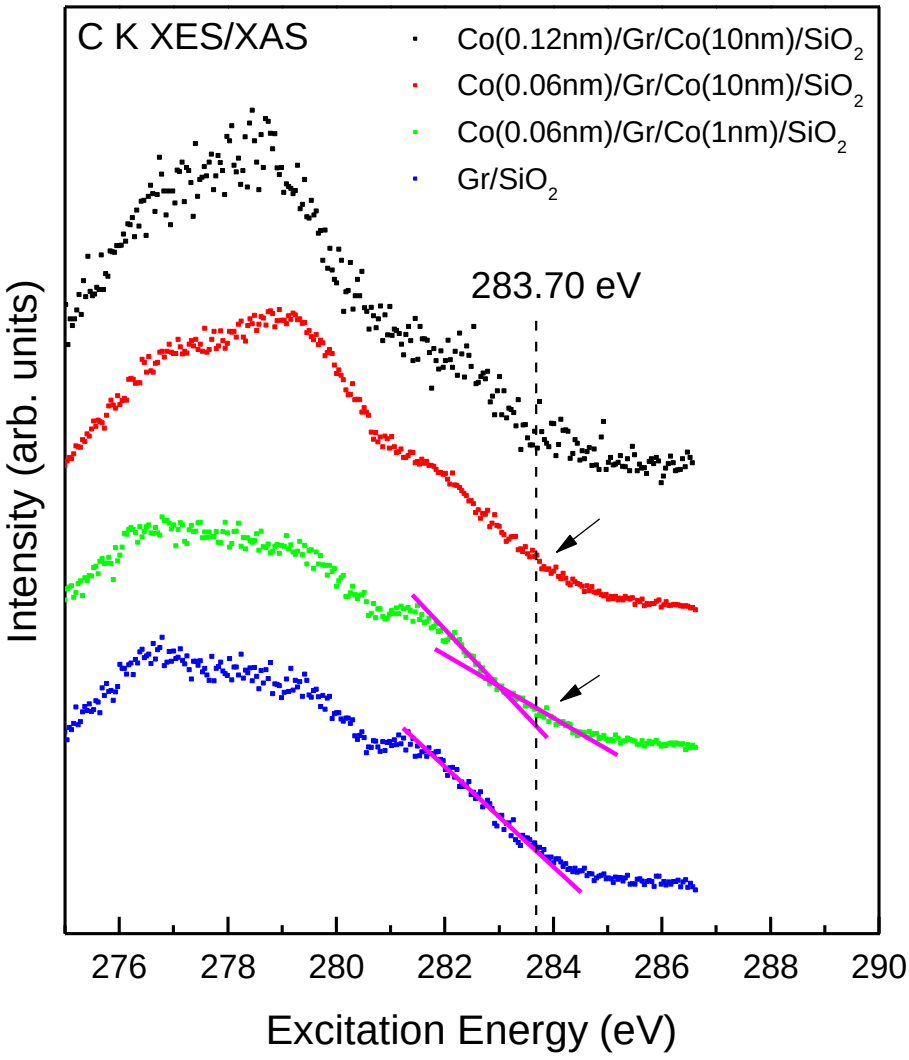

Figure A.4. C *K* XES of Co/Gr/Co showing a second peak appearing near the valence band edge due to hybridization of Co 3*d* and C 2*p* states.

APPENDIX B

BAND GAP DETERMINATION USING 2ND DERIVATIVES

Determination of band gaps in this study was accomplished using linear line fitting as opposed to 2nd derivatives mainly due to the low counts that could be obtained from XES of graphene. In some cases the counts collected that represent actual spectral features can be close to the intensity of the noise. Since the 2nd derivative method relies on identifying a peak (or trough) in a plotted line, it must be clear which peak one should pick without subjectivity. In the case of a solid state or non-molecular system with degenerate and continuous density of states, the edge of the valence or conduction band is defined by a point of sharp incline of the spectral line, represented by a peak in the 2nd derivative. In an organic material possessing molecules the density of states is comprised of energy localized molecular orbitals, represented by peaks in the X-ray spectra, and therefore troughs in the 2nd derivative. This method has been used by several studies to determine the band gap of many materials finding good agreement with other experimental methods [101,102]. With that in mind, one need only take the first peak or trough going outward in the 2nd derivative of XES and XAS spectra. This presents another problem where a measurement with low counts may not resolve enough detail in spectra, resulting in incorrect or unphysical values for band gap. This is observed in Figure B.1 where a band gap of about 1.0 eV is observed for all cases of Co deposited on the surface when applying this method. The interpretation problem in limited to the XES; the 2nd derivative does correctly indicate the shift observed in the main π*peak of the XAS.

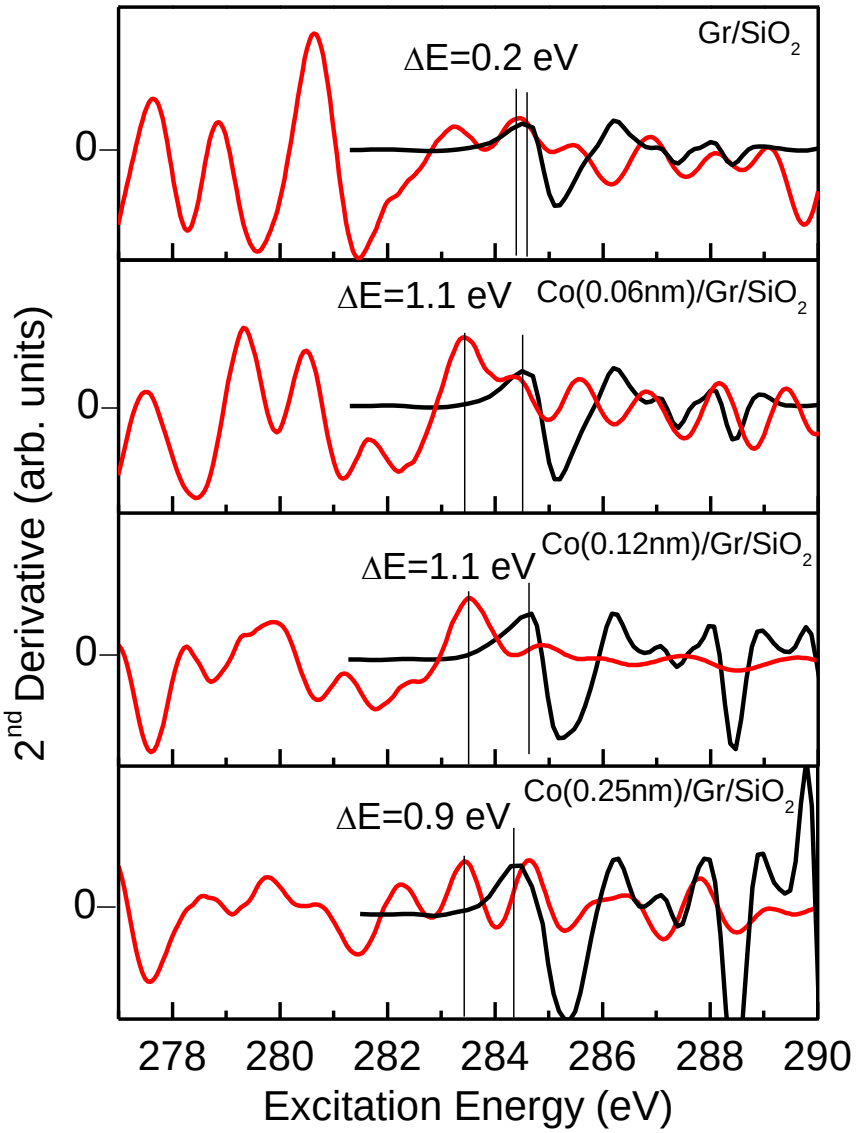

Figure B.1. 2nd Derivatives of Co/Graphene/SiO_2 samples.